8-18-2022

BIOENGINEERED SCAFFOLDS TO INDUCE ALIGNMENT AND PROMOTE AXON REGENERATION FOLLOWING SPINAL CORD INJURY

Kiet Anh Tran
Rowan University

BIOENGINEERED SCAFFOLDS TO INDUCE ALIGNMENT AND PROMOTE AXON REGENERATION FOLLOWING SPINAL CORD INJURY

by

Kiet Anh Tran

A Dissertation

Submitted to the
Department of Biomedical Engineering
College of Engineering
In partial fulfillment of the requirement
For the degree of
Doctor of Philosophy
at
Rowan University
July 25, 2022

Dissertation Chair: Peter A. Galie, Ph.D., Professor, Department of Biomedical Engineering, Rowan University

Committee Members:
Erik C. Brewer, Ph.D., Professor, Department of Biomedical Engineering, Rowan University
Paul A. Janmey, Ph.D., Professor, Department of Physiology, University of Pennsylvania
Alan Turtz, M.D., Department of Neurosurgery, Cooper University Hospital
Sebastian L. Vega, Ph.D., Department of Biomedical Engineering, Rowan University

Dedication

To my fiancé and family, without whom none of my success would be possible.

Acknowledgments

First, I thank my advisor Dr. Peter Galie for his mentorship, guidance, and support throughout this work. Thank you for your invaluable lifelong lessons that extended beyond performing authentic biomedical research in the lab. I am beyond honored to have worked with you and forever grateful for the freedom I was given to explore my scientific curiosity.

Second, I thank the committee members for their mentorship and continuing support: Dr. Erik Brewer, Dr. Paul Janmey, Dr. Alan Turtz and Dr. Sebastian Vega. You have been instrumental in the professional development of my career as a student and scientist.

Moreover, this work would not have been possible without the highly motivated Galie lab members: Paul Partyka, Nesrine Bouhrira, Brandon DeOre, and Louis Paone. Thank you for aligning your experiment schedule with mine during those late-night and weekend hours. I thank Dr. Ying Jin and Julien Bouyer, who have made significant contributions towards the in vivo implantations of our injectable and 3D-printed constructs. I thank Fitzroy Byfield for his willingness to help with our tissue mechanics studies.

Finally, my biggest thanks go out to my family – Mom, Dad, and Khoa – for their unwavering support. My parents, of course, played a pivotal role in my success, and I am forever grateful for their belief in me. I would like to extend my gratitude towards my brother, Khoa and best friend, Frankie Coffman for their endless support during my time as a PhD student. And lastly, my fiancé, Vivian, thank you for your relentless encouragement throughout this journey.

Abstract

Kiet Anh Tran
BIOENGINEERED SCAFFOLDS TO INDUCE ALIGNMENT AND PROMOTE AXON REGENERATION FOLLOWING SPINAL CORD INJURY
2018-2022
Peter A. Galie, PhD
Doctor of Philosophy

Scaffolds delivered to injured spinal cords to stimulate axon connectivity often act as a bridge to stimulate regeneration at the injured area, but current approaches lack the permissiveness, topology and mechanics to mimic host tissue properties. This dissertation focuses on bioengineering scaffolds through the means of altering topology in injectables and tuning mechanics in 3D-printed constructs as potential therapies for spinal cord injury repair. A self-assembling peptide scaffold, RADA-16I, is used due to its established permissiveness to axon growth and ability to support vascularization. Immunohistochemistry assays verify that vascularized peptide scaffolds promote axon infiltration, attenuate inflammation and reduce astrogliosis. Furthermore, magnetically-responsive (MR) RADA-16I injections are patterned along the rostral-caudal direction in both *in-vitro* and *in-vivo* conditions. ELISA and histochemical assays validate the efficacy of MR hydrogels to promote and align axon infiltration at the site of injury. In addition to injectable scaffolds, this thesis uses digital light processing (DLP) to mimic the mechanical heterogeneity of the spinal cord caused by white and gray matter, and demonstrate that doing so improves axon infiltration into the scaffold compared to controls exhibiting homogeneous mechanical properties. Taken together, this work contributes to advancing the field of tissue engineering and regenerative medicine by demonstrating the potential of bioengineered scaffolds to repair the damaged spinal cord.

Table of Contents

Table of Contents (Continued)

Table of Contents (Continued)

Table of Contents (Continued)

Table of Contents (Continued)

List of Figures

Figure Page

List of Figures (Continued)

Figure Page

List of Figures (Continued)

Figure Page

Chapter I

Introduction

Spinal cord injury (SCI) is a neurological disorder that stems from mechanical forces that cause synaptic failure between axons that eventually lead to neurodegeneration and ultimately result in permanent disabilities [1]–[3]. The primary injury results in the death of neurons and cause the blood vessels to lose their blood-spinal cord barrier [4]. Subsequently, inflammation caused by disruption of the barrier leads to the formation of glial scars that prevent axons from regenerating into the injured area [2]. SCI affects approximately 17,730 new patients per annum, causing over 291,000 hospitalizations annually in the United States alone [5]–[9]. Despite the previous therapeutic attempts to bridge the site of injury, glial scars present a physical barrier to obstruct axon regrowth and the influx of microglia and reactive astrocytes provide a biochemical barrier that becomes a hostile environment to prevent neuroregeneration [10]. This hostile environment is one of the major factors preventing neuronal regeneration and subsequently an effective repair strategy for these pathologies. To encourage axon regrowth, therapeutic strategies have attempted to attenuate glial scar formation through the inhibition of glial fibrillary acidic protein (GFAP) which have been shown to exacerbate the injury, suggesting that scarring exerts neurotropic properties even though it inhibits neuronal regeneration [11], [12]. The prevalence and permanence of SCI create a substantial public health issue, necessitating a strategy to restore function by instigating axon regrowth and connectivity.

Current approaches to treat SCI rely heavily on pharmacological and activity-based rehabilitation strategies that include neurotrophic factors to promote neuronal growth and

survival at the site of injury [13]–[15]. However, these approaches have proven to be minimally effective due to the inability to restore axon connection and facilitate the direction of regrowth in the presence of glial scars. In addition to preventing axon regrowth, scars in the central nervous system are initially more compliant than the surrounding tissue due to an altered extracellular matrix (ECM) composition [16]. The change in tissue mechanics presents a blockage to inhibit axon regeneration that disrupt cell-matrix interactions and mechanosensing between axons and the surrounding microenvironment. Yet, none of these therapeutic strategies have shown to restore axon connectivity in human patients.

Bioengineered scaffolds designed to treat spinal cord injury fall under two broad categories: (i) injectable strategies and (ii) solid scaffolds. Transplantation of injectable biomaterials is less invasive than pre-fabricated scaffolds because they can be delivered through small-gauged needles; however, this delivery method precludes patterning topologies that guide cell growth and motility. Although studies have altered fiber orientation with magnetic fields in vitro [17]–[21], this approach has not been applied in vivo. Yet, magnetic fields can penetrate beyond the range of light-based methods, especially in tissues obstructed by bone including the spinal cord. Therefore, part of this dissertation uses spinal cord injury as a model to determine whether a magnetic field can align a self-assembling peptide hydrogel in the rostral-caudal direction following injection. Overall, these results in this dissertation indicate that magnetism is a viable means to align biomaterials post-injection.

Another approach to bridge the cavity of the spinal cord is to implant prefabricated conduits that facilitate the growth of axonal processes across the site of damage provide

the potential for a direct multifunctional treatment. A limitation of previous scaffolds is the inability to fabricate scaffolds with complex topologies that have tunable mechanical properties. Conduits featuring voids aligned in the rostral-caudal direction have been used in models of spinal cord injury, but consist of materials with fixed mechanical properties [22]. 3D-printing provides a means to precisely control the geometry and topology of scaffolds, and has been used previously to repair spinal cord injury in small animal models [23]. However, the scaffolds in that particular study exhibited an elastic modulus exceeding 200 kPa, which far surpasses the mechanical properties of the surrounding tissue and precludes the ability to seed cells within the bulk of the scaffold. Our laboratory has helped to pioneer a 3D-printing approach to print complex topologies within tunable 3D scaffolds that overcomes the limitations of previous strategies [24]. This process can be used to control and guide the growth of axons in scaffolds with tunable mechanical and biochemical properties to facilitate both infiltration and outgrowth from the site of injury. Specifying a microenvironment that overcomes the barrier created by the inflammation and scarring caused by the injury provides an alternative strategy to instigate axon infiltration.

Chapter II

Background

2.1. Vascularized Injectables as Potential Therapies for Spinal Cord Injury Repair

Bioengineered scaffolds hold tremendous potential for stimulating axon growth in the aftermath of a spinal cord injury (SCI). The purpose of a scaffold is to bridge the damaged spinal cord so that patients can experience functional recovery, and clinical trials using scaffold transplantation have already begun [25]. Previously described strategies include providing physical guidance cues for axon growth/regeneration [26], [27], releasing neuroprotective or neuroregenerative growth factors [28], or delivering precursor or support cells to the injury site [29]–[31]. However, as with many other endeavors involving scaffold and cell transplantation, delivery of nutrients and oxygen to the injury site remains a challenge. Axons regenerating into the scaffold require oxygen transport to continue their growth, as do precursor cells seeded into the injury site. Moreover, a recent study demonstrated that a pre-vascularized scaffold encouraged the growth and guided the regeneration of host axons into a collagen-hyaluronan composite matrix following transplantation [32]. These results validate that scaffold vascularization provides a promising strategy to advance bioengineered scaffolds for SCI repair.

In the aftermath of SCI (7–10 days post-injury), a strong angiogenic response mediated by VEGF and HIF1-α restores oxygen and nutrient transport to the site of injury [33]–[35]. However, these nascent vessels initially lack a blood-spinal cord barrier (BSCB) [36], and are thus unable to prevent the inflammation and reactive gliosis that exacerbate the damage. Inflammation and scar formation represent the secondary aspect of SCI that contributes to the inhibition of axon growth and functional recovery. Rat models of SCI

indicate that in the months following this initial angiogenic response, the density of the vasculature significantly decreases as the tissue remodels [36]. Transplantation of vasculature exhibiting a functional BSCB within a bioengineered scaffold can potentially stabilize the vasculature within the cord and attenuate the inflammatory effects that inhibit neuroregeneration.

RADA-16I, a peptide that forms a self-assembling hydrogel in response to pH, is the main component of the scaffolds used in specific aim 1 and 2. The composition of RADA16-I (Ac-RADARADARADARADA-CONH2) exhibits an appropriate structural environment that supports the growth of axons following SCI [37] and minimizes glial scar and inflammation in surrounding tissue [38]. Furthermore, studies have shown that the scaffold exhibits biocompatibility with host tissue and causes minimal tissue inflammation and immune response [39]–[42]. RADA-16I also provides a three-dimensional environment that allows cells to grow, proliferate and migrate [41], [43]–[45]. Previous studies have shown that not only can RADA-16I effectively treat intracerebral hemorrhage [46], but this synthetic material is also capable of providing a favorable environment for capillary morphogenesis [47], though microvessels with BSCB-integrity have yet to be fabricated within RADA-16I prior to the studies within this dissertation. Overall, its established ability to support vascularization and axon growth validates the use of RADA-16I in the work in this dissertation.

2.2. Methods to Facilitate Rostral-Caudal Alignment in Injectables Post-Delivery

One benefit of regenerative scaffolds is the ability to provide a compatible matrix with guidance cues to cells within and surrounding the scaffold. A common example of this approach is provided by scaffolds and conduits delivered to the site of spinal cord

injury; alignment in the rostral-caudal direction improves host axon infiltration and can also mitigate secondary aspects of the injury including inflammation and glial scarring [48]–[50]. Such guidance cues can be provided by cylindrical holes aligned in the axial direction of the conduit [51]–[53]. Recent advances in 3D printing have been used to apply this technique to geometries that match specific tracts within the spinal cord [54]. However, scaffold alignment can also be implemented on the level of individual fibers, using techniques that include electrospinning [55], [56] and the application of either interstitial flow [32] or mechanical stretch [57], [58]. Previous work from our laboratories demonstrated that transplanting scaffolds with aligned microvessels exerted a similar benefit on guiding axon infiltration in a spinal cord injury model [32]. However, previously described approaches are only compatible with pre-fabricated scaffolds: they are not applicable to injectable hydrogels.

The primary advantage of injectable strategies for the treatment of spinal cord injury and other pathologies is their minimal invasiveness compared to pre-fabricated scaffolds. Injectable hydrogels can be delivered through small gauge needles, and mitigate the damage to surrounding healthy tissue incurred by the transplantation of a solid-phase scaffold. The majority of cell therapies in current clinical trials for the treatment of spinal cord injury are delivered via injection [59], providing a framework for similar transplantation with hydrogels. Furthermore, advances in self-assembling peptide hydrogels have demonstrated the therapeutic potential of injectable scaffolds for a variety of regenerative applications [37]–[39], [41]. Specifically, RADA-16I has been shown to improve axon infiltration following central nervous system injury. Recently, our laboratories demonstrated the benefit of injecting RADA-16I hydrogels seeded with

microvascular cells for increasing axon infiltration and reducing inflammation and scarring [60]. However, the limitation of RADA-16I and other self-assembling hydrogels is the inability to control the orientation and topology of the fibrous matrix.

The regenerative potential of injectable hydrogels can be augmented by strategies to tune physical guidance cues following delivery. Previous studies have described methods to alter hydrogel structure following transplantation: photocrosslinkable hydrogels such as PEGDA can be altered with the administration of ultraviolet light following delivery [24], [61]. However, light-based approaches are limited by the depth the scaffold is transplanted and whether the injury site is obscured by bone. Thus, a light-based method to alter an injectable hydrogel is not an option for spinal cord regeneration [62]. In contrast to UV and visible light, magnetic fields penetrate further into the body and thus provide an option to tune hydrogel topology. Several *in vitro* studies have demonstrated that seeding magnetic particles (MPs) into hydrogels and applying a magnetic field prior to polymerization results in alignment of fibrous matrices [17]–[21]. However, these techniques have yet to be implemented as a strategy *in vivo*, despite the potential to overcome the limitations of existing methods to alter hydrogels post-transplantation.

A goal in this dissertation is to assess magnetic alignment as a strategy to align RADA-16I self-assembling hydrogels injected into a rat model for spinal cord injury. Specifically, a contusion injury model is used to increase the clinical relevance of these studies. The magnetically responsive (MR) scaffolds are combined with human mesenchymal stem cells (hMSCs), which have shown encouraging results from ongoing clinical trials [59]. In order to determine the parameters needed to align the fibrous

network, initial *in vitro* experiments are conducted using hMSC-seeded peptide hydrogels and rat-derived neural progenitor cells (NPCs) to replicate *in vivo* environments. The magnetic parameters found to align the peptide hydrogels are subsequently extended to proof-of-concept animal experiments for facilitating axon growth along the rostral-caudal direction. Overall, these experiments evaluate magnetic alignment in both *in vitro* and *in vivo* environments to determine its potential to align injectable hydrogels following delivery.

2.3. Magnetic Particles to Dynamically Alter Viscoelastic Hydrogels

Our research indicated that applying magnetic fields to MR hydrogels provided the capability to rapidly and reversibly tune their mechanical properties. Previous understanding of how cells respond to the mechanics of their extracellular matrix (ECM) has been traditionally informed by experiments using two-dimensional (2D) substrates [63], [64]. These studies have demonstrated that cells alter their morphology [65], signaling [66], and phenotype [67] based on the mechanical properties of polyacrylamide or polydimethylsiloxane substrates to which they are attached. Yet, most non-epithelial cell types are fully surrounded by their ECM, and 2D substrates are unable to capture this aspect of the in vivo microenvironment. Alternatively, cells can be seeded within three-dimensional (3D) hydrogels to mimic cell-ECM interactions. Studies using hydrogels have identified multiple facets of the cell response that differ between 2D and 3D geometries [68], [69]. However, in contrast to the linearly elastic substrates used for 2D mechanotransduction studies, the mechanics of 3D hydrogels, especially those comprised of natural proteins including collagen and fibrin, are complicated by viscoelastic and strain

stiffening properties that have been shown to alter the cell response [70]–[73]. Nonetheless, these properties are more representative of the mechanics of the ECM in vivo.

Although 3D hydrogels better mimic the geometry and mechanics of the ECM, tuning the mechanical properties of these scaffolds is more difficult than 2D substrates. Doing so dynamically is even more challenging. Currently, methods to alter the mechanics of cell-seeded 3D scaffolds rely primarily on photocrosslinkable [74], [75] and photodegradable [76], [77] chemistries. However, these approaches generally require substantial modification of hydrogel chemistry and composition and cannot be reversibly cycled through a broad range of mechanical properties. Moreover, cytotoxicity assays reveal that cell viability significantly decreases as the concentration of photocrosslinkers increases, limiting the possible range over which these substrates can be tuned. Studies have found that altering the degradability of these hydrogels affects the cell response to the mechanics of their surroundings, preventing direct interrogation of the effect of 3D substrate stiffness [74]. These limitations necessitate a reversible and repeatable method to modify hydrogel mechanics without changing the microstructure of the surrounding fibrous matrix.

Magnetorheological materials containing carbonyl iron microparticles (MPs) provide a means to overcome the limitations of previous methods to tune hydrogel mechanics. These materials respond to external magnetic fields in a rapid, reversible, and repeatable manner [78], [79]; their stiffness can substantially increase or decrease by changing the strength of the magnetic field. This effect is dependent upon MP concentration, demonstrating that greater changes can be achieved by adding more magnetic particles [80]. Previous studies have used 2D substrates embedded with MPs to

study cell mechanotransduction [78]. However, cells can also be embedded inside of magnetorheological materials like kappa-carrageenan and N, N-dimethylacrylamide (DMAAm) and laponite without a loss of viability [81], [82].

This dissertation evaluates the ability of MPs to dynamically tune the mechanical properties of hydrogels consisting of natural proteins and proteoglycans, creating a method is applicable to a broader range of scaffolds than previously described synthetic magnetorheological materials. Here, scaffold mechanics are dynamically tuned by submerging carbonyl iron MPs and applying an external magnetic field. Embedding 10 wt% MPs into a 5 mg/mL collagen scaffold with the application of 4,000-Oe magnetic field drastically increases the storage modulus from approximately 1.5 kPa to 30 kPa. More importantly, translating this approach to hydrogels containing proteins and proteoglycans gives rise to a more physiologically-relevant platform to control cell morphology, mechanosensing pathways, and calcium transients. The findings described in this work demonstrate that magnetically-responsive hydrogels provide a new means to rapidly and reversibly tune hydrogel mechanics to evaluate cellular mechanotransduction in 3D.

2.4. 3D-Printed Scaffolds for Spinal Cord Regeneration

Although injectable scaffolds are minimally invasive, 3D-printed scaffolds provide the ability to alter topology and geometry to stimulate regeneration. A potential benefit of transplanting bioengineered scaffolds is the delivery of a matrix with mechanical properties that mimic the host tissue, but the mechanics of native tissue are often heterogeneous and difficult to characterize. In particular, our understanding of the mechanical properties of the central nervous system (CNS), specifically the spinal cord, has primarily been informed by macroscale measurements [83]–[85]. These studies have shown that CNS mechanics

are heterogenous via tensile, shear, compression testing [86], [87] and magnetic resonance elastography [88], [89]. In order to supplement bulk approaches, atomic force microscopy (AFM) has proven a useful tool to measure the stiffness of the spinal cord with higher spatial resolution. However, published data are contradictory regarding the difference in mechanical properties between white and gray matter [90]–[92]. Physiologically, white and gray matter exhibit differences in cellular and matrix composition: white matter mainly consists of glial cells and myelinated axons aligned along the rostral-caudal direction, whereas gray matter is mostly comprised of neuronal cell bodies and glial cells, which likely alters the macroscale mechanical properties. Moreover, the complex and variable environment of a spinal cord injury (SCI) is known to alter cord mechanics [16]. Therefore, transplanting a scaffold that mimics the mechanical heterogeneity of white and gray matter may improve axon infiltration at the site of spinal cord injury.

Bioengineered scaffolds with a wide array of mechanical properties have previously been used in spinal cord injury. The overall goal of transplanted hydrogels or conduits is to bridge the injured area by facilitating axon connectivity and eventual functional recovery for patients. Previously used scaffolds in animal studies and human clinical trials incorporate a wide variety of biomaterials including collagen [32], polycaprolactone [93]–[96], electrospun fibers [97]–[99], fibrin [100]–[102] and can either be injected [60], [103] or delivered as solid conduits [32]. These approaches use several repair strategies including delivery of neurotrophic factors or cells [104], implementation of a conductive microenvironment using electrically active materials [105], and providing guidance cues by anisotropic topologies including cylindrical voids [94], [106], [107]. Considerations for biomaterials used in previous spinal cord scaffolds include

biocompatibility, degradability, and premissivity to infiltrating axons from the host. Yet, none of the previous approaches tune the mechanical heterogeneity within the construct as a potential repair strategy for spinal cord regeneration.

3D-printed scaffolds provide a means to fabricate heterogeneous mechanical properties that match native spinal cord tissue. Previous approaches have demonstrated that photocrosslinkable hydrogels can be used in 3D-printed systems that can mimic the anisotropy of various tissues including skeletal muscle [108], bone [109]–[111], cartilage [112]–[115], and neural tissue [116], [117]. 3D-printing has been used to fabricate spinal cord conduits that feature voids aligned in the rostral-caudal to mimic specific axon tracts [23]. However, the scaffolds in that particular study exhibited an elastic modulus exceeding 200 kPa, which far surpasses the mechanical properties of the surrounding spinal cord tissue and precludes the ability to differentiate between the stiffness of white and gray matter. Recent innovations in 3D-printing approach, specifically digital light printing (DLP) have been used to create complex topologies within tunable 3D scaffolds that overcomes the limitations of previous strategies [24], [118]. This process can be used to control and guide the growth of axons in scaffolds with heterogeneous mechanical properties to facilitate both infiltration and outgrowth from the site of injury. In this work, an array of macroscale and microscale mechanical tests are used to characterize the mechanical properties of native spinal cord tissue, and then use DLP to mimic the mechanical heterogeneity in transplantable scaffolds.

2.5. Hypothesis and Specific Aims

This dissertation describes the potential for both injectable and solid scaffolds to stimulate central nervous system (CNS) regeneration by providing biophysical guidance

cues for host axons. These two categories have tremendous potential to create biomaterials or constructs that stimulate neuronal regeneration, but there are few examples of exploiting this technology for CNS applications. Previous approaches have yet to alter topologies on the individual fiber level to facilitate cell growth in vivo and fabricate mechanical heterogeneity in 3D-printed constructs to promote neuronal regeneration. In addition to delivering these biomaterials to the site of injury, cells can be transplanted into the bulk of these constructs (both injectable and 3D-printed scaffolds) to provide neurotropic properties that will instigate neuronal regeneration. Therefore, the approaches described in this dissertation not only bolsters scaffold-based therapeutics for transplantation, but also increases the capability of cell-based therapies to provide neurotropic factors delivered to the site of injury.

The spinal cord is a unique tissue to test the functionality of implanted biomaterials in the central nervous system because of its anisotropic axon topology. Previous strategies reveal that alignment in the rostral-caudal direction provides functional benefits by encouraging infiltration and reconnecting axons following spinal cord injury (SCI). However, less is known about the potential benefits of vascularized scaffold to induce axon infiltration, altered topology along the rostral-caudal direction in injectables post-delivery, and mechanical properties on neuronal infiltration and outgrowth. To date, the initial indicator of regeneration relies on alignment in the rostral-caudal direction to improve host axon infiltration that can also mitigate secondary aspects of the injury including inflammation and glial scarring. The specific aims of this dissertation seek to design and fabricate bioengineering scaffolds that induce alignment and promote axon infiltration

following spinal cord injury. The following aims will be used to test the hypothesis and interrogate the benefits of both injected and transplanted scaffolds on neuroregeneration.

2.6. Research Aims

Aim 1: Evaluate axon infiltration and secondary injury following delivery of vascularized injectable hydrogels in contusion spinal cord injury model. The experiments conducted in this aim will examine the effectiveness of implanting injecting scaffolds with blood-spinal cord barrier (BSCB)-integrity microvessels to augment and facilitate axon infiltration. Vascularized self-assembled peptide scaffolds will be administered at the site of a rat model of a cervical contusion spinal cord injury to determine whether transplanted microvessels augment axon infiltration. The efficacy of these scaffolds will be determined primarily by immunohistochemistry to evaluate axon infiltration, inflammation and scar formation. These experiments will evaluate the effects of cell-seeded peptide injections for spinal cord repair.

Aim 2: Align injectable, self-assembled peptide hydrogels seeded with mesenchymal stem cells using magnetic fields following contusion spinal cord injury. The second aim will validate a post-injection method to magnetically align scaffold fibers to facilitate axon regeneration in the rostral-caudal direction at the site of spinal cord injury. Stem cell-seeded scaffolds containing magnetic particles will be delivered at the site of a rat model of a contusion spinal cord injury in the presence of a magnetic field to align the fibrous network. Similar to Aim 1, the primary metric to assess the injury response will involve immunohistochemistry to determine axon alignment. These studies will measure the paracrine release from the MSC to assess the molecular mechanisms underlying their response.

Aim 3: Interrogate axon infiltration into 3D-printed scaffolds with heterogeneous mechanical properties in a transection spinal cord injury model. This aim will tune scaffold mechanics to mimic native surrounding spinal cord tissue. The mechanics of uninjured spinal cord tissue will be described by both atomic force microscopy and rheology to characterize both microscale and macroscale properties of native tissue. 3D-printed GelMA scaffolds will be used to replicate the mechanical properties and geometries of the surrounding spinal cord. Additionally, the effects of cell-seeded scaffolds on functional benefits will be examined in a rat model of a transection injury. Immunohistochemistry will be the primary metric to assess axon infiltration and connection following transected spinal cord injury.

Impact: The proposed studies will combine a novel bioengineering approach with established cell-based therapies to create a new strategy for axon connectivity in the central nervous system. Although these experiments focus primarily on SCI, they have direct relevance for other pathologies involving an inability to restore axonal connectivity. For example, if successful, this approach can also be applied to traumatic brain injury (TBI) and other forms of central nervous system injury.

2.7. Innovation

This proposal highlights several innovative aspects for injectable scaffolds:

1) Although there are several studies that have interrogated the efficacy of various scaffolds on axon infiltration after central nervous system injury, these approaches have yet to induce neurovascular interactions. These studies will include microvascular endothelial cells that exhibit a blood-spinal cord barrier to stimulate axon infiltration and guide neuronal regrowth.

2) Another innovative aspect is the ability to magnetically align of injectable scaffolds post-delivery. Magnetic particles provide a means to tune topologies post-injection in peptide scaffolds by facilitating axon infiltration in a rostral-caudal direction for spinal cord injury repair. These studies will compare the effects of MSC-seeded scaffolds on the infiltration of axons and the attenuation of inflammatory response. Reports from ongoing clinical trials have demonstrated the potential efficacy of autologous MSC transplantation on functional benefits in human patients of spinal cord injury[59].

Other innovative aspects for solid transplantable hydrogels:

1) Although prior approaches have used 3D-printing to create scaffolds for the purpose of central nervous system regeneration, previous fabrication methods preclude the seeding of cells within the bulk of the hydrogels. The method described here capitalizes on a recently described approach to pattern complex topologies within cell-permeable scaffolds. Therefore, not only can conduits with predetermined geometries be delivered with cells, but host cells can also invade into the bulk of the scaffold and facilitate nutrient and oxygen transport. An approach combining 3D-printing with cell-permeable hydrogels has not previously been used for central nervous system regeneration.
2) The fabrication strategy described in this proposal also allows for tuning of the mechanical properties of the scaffold. The mechanics of the central nervous system following injury is substantially different than other organs: whereas fibrotic scarring in other regions of the body decrease the compliance of the injured tissue, the site of a CNS injury exhibits an increased compliance. Thus,

the mechanical properties of spinal cords are determined locally by examining the stiffness of gray and white matter and globally to examine whether ratios of gray-to-white matter will contribute to the bulk mechanics. These parameters will be used to alter the mechanical properties of 3D-printing scaffolds to provide a means to tune mechanics for optimal axon regrowth.

3) The proposed studies will also compare the effects of seeding MSCs with seeding endothelial cells on the infiltration and outgrowth of axons from the scaffold. The proposed studies will assess the benefit of delivering MSCs within a scaffold to improve retention and to provide guidance pathways for infiltrating axons.

Chapter III

Materials and Methods

3.1. Experimental Methods for Vascularization of Injectable Peptides

3.1.1. Rheological Testing

To characterize the mechanical properties of the RADA-16I peptide scaffold, 40 µL of 1 mg/mL peptide in 10% sucrose (the concentrations used for in vitro and transplantation studies) was loaded onto a 1°, 20-mm cone-plate rheometer (TA Instruments) fitted with a Peltier plate to maintain a temperature of 37 °C. 1% cyclic strain applied at a frequency of 1-Hz was applied to the gel for 600 s. The rheological properties of the scaffold were measured every 5 s, and storage modulus and loss angle were used to evaluate polymerization of the peptide.

3.1.2. Microfluidic Device Fabrication

RADA-16I hydrogels were polymerized inside a polydimethylsiloxane (PDMS)-based microfluidic device fabricated using soft lithography [24]. Microfluidic devices were fabricated using positive-featured PDMS stamps containing a rectangular chamber with dimensions of 4 mm × 6 mm × 1 mm (L × W × H). A layer of PDMS was used to enclose the rectangular reservoir and act as a membrane securing the peptide gel. Nine ports were punctured in this layer with a biopsy punch to provide access to culture medium pipetted on top of the device. After assembling the two layers, the devices were cooked at 150 °C and placed on a 22 mm × 22 mm glass cover slip.

3.1.3. Cell Culture

Human cerebral microvascular endothelial cells (HCMEC/D3) were cultured in gelatin-coated tissue culture plates. Modified endothelial growth medium-2 (mEGM-2)

was prepared as previously described [25]. The final concentrations of reagents in mEGM-2 were 5 µg/mL ascorbic acid (Sigma), 1 ng/mL bFGF (Peprotech), 1% chemically defined lipid concentrate (Thermo Fisher), 5% fetal bovine serum (FBS) (VWR), 10 mM HEPES buffer (VWR), 1.4 µM of hydrocortisone (VWR), and 1% penicillin-streptomycin (VWR). HCMEC/D3 were thawed 5 days prior to seeding and medium was changed every other day. For in vivo experiments, human brain vascular pericytes (HBVP) were cultured in tissue culture plates with DMEM (VWR) supplemented with 10% FBS, 1% penicillin-streptomycin, and 1X MEM Amino Acid Solution (VWR).

3.1.4. In-Vitro Cell Seeding

HCMEC/D3 from confluent plates were washed with PBS and suspended in 10% sucrose at a density of 5×10^6 cells/mL. The solution containing cells was centrifuged and the cell pellet was resuspended in a 1:1 mixture of 20% sucrose and self-assembling peptide, yielding the final concentrations of 10% and 1 mg/mL and 5.0×10^6 cells/mL. Following suspension, the peptide-cell solution was injected into the central chamber of the microfluidic device and placed in a 6-well cell culture plate. mEGM-2 containing 10% FBS was carefully added directly above the chamber, and after an hour of incubation, the media was replaced with mEGM-2 supplemented with 0.1 mg/mL vascular endothelial growth factor (VEGF) and 1 mg/mL phorbol 12-myristate 13-acetate (PMA) and incubated for five days to stimulate vascular formation similar to a previous approach [23].

3.1.5. Permeability Testing

In order to assess barrier function within the vascular structures after five days in culture, 500 µL of 4-kDa dextran was pipetted on the surface of the microfluidic device containing the cellular peptide gel to test the integrity of tight junctions of endothelial cells.

Images were taken on a Nikon A1 confocal microscope at intervals of 10 s for 15 min at z heights corresponding to vessel lumens. The images were then imported to ImageJ for analysis. The permeability coefficients were quantified using a method in a previous study [8], [26]. Briefly, assuming the dextran concentration remains constant in the surroundings and the cylindrical geometry of the vessels, permeability coefficients can be calculated from the flux of solute across an area of the capillary using Fick's First Law of Diffusion. Here, assuming a fixed concentration outside the vessels, the dextran concentration was directly correlated with fluorescent intensity yielding the following equation for permeability coefficient: $P = \frac{r}{2I_o}\frac{dI}{dt}$, where dI/dt is the change of fluorescent intensity inside the lumen, r is the radius of the vessel, and Io is the maximum intensity through the duration of the experiment.

3.1.6. Immunocytochemistry

Devices were fixed in 4% paraformaldehyde (Alfa Aesar) at room temperature for 20 min. Afterwards, cellular peptide hydrogels were permeabilized with of 0.2% Triton X-100 (Sigma) for 30 min at room temperature. Peptide hydrogels were then removed from the central chamber of the devices and blocked by 3% bovine serum albumin (BSA) for 30 min at room temperature. These permeabilized hydrogels were incubated with 1:250 anti-ZO-1 (Cell Signaling) for two nights at 4 °C. These gels were then washed thoroughly in PBS and incubated with 1:500 DAPI, 1:50 FITC-phalloidin, and 1:500 secondary antibody Cy-3 at 37 °C for 60 min. Images were acquired on a Nikon A1 laser scanning confocal microscope.

3.1.7. Preparing Cells in Injectable Peptide Scaffold

GFP-labeled HCMECs/D3 were mixed with GFP-labeled HBVP, given that these cells have been shown to support endothelial viability post-transplantation [8]. The cells were suspended in 20% sucrose at densities of either 2.4×10^6 cells/mL or 5×10^6 cells/mL with a ratio of 5:1 HCMEC/D3 to HBVP, consistent with the ratio used in previous studies [8], [27]. The cell solution was combined with self-assembling peptide to yield final concentrations of 10% sucrose and 1 mg/mL peptide. Freshly made peptide with or without cells was injected into the lesion area immediately after preparation.

3.1.8. Spinal Cord Surgery and Transplantation

Surgeries were conducted at the Drexel University Queen Lane Medical Campus. All procedures were approved by the Institutional Animal Care and Use Committee of Drexel University College of Medicine, and were carried out according to the National Institutes of Health (NIH) Guide for the Care and Use of Laboratory Animals. Female Sprague-Dawley rats (225–250 g, n = 12) were used in this specific aim. They were housed with a 12-h/12-h light/dark cycle. Food and water were available ad libitum.

Rats were anesthetized with 5% isoflurane until unconscious followed by 3% isoflurane during surgery. A laminectomy was performed at C5, and a contusion lesion was made with IH impactor (force, 150 kdyne; impactor tip diameter, 2 mm. Precision Systems and Instrumentation, LLC, Lexington, KY) at the right side of the cord. Muscles and skin were closed in layers. Buprenex (0.015–0.02 mg/kg, Reckitt Benckiser, Richmond, VA) was administered subcutaneously post-surgery. One week after contusion, rats were anesthetized with isoflurane for scaffold transplantation. The lesion area was re-opened, and 10 µL of peptide was injected into the lesion area as an acellular control (n = 4). 10 µL

of peptide with cells in two densities were injected into lesion area: 2.4 × 106 and 5.0 × 106 (n = 4 per group), with a ratio of 5:1 endothelial cells to pericytes for both densities. Therefore, a total of 12 animals were used for these studies. Muscles were sutured and skin was closed with clips. Buprenex (0.015–0.02 mg/kg) was administered subcutaneously post-surgery. All animals received subcutaneous injection of cyclosporine A (Sandimmune; Novartis Pharmaceuticals, East Hanover, NJ, USA) at a dose of 1 mg/100 g per day beginning 2–3 days before transplantation and continuing until the end of the experiments. Animals survived for 2 weeks after scaffold transplantation.

Transplantations were performed one week following contusion to model subacute spinal cord injury, both to maintain translational relevance since patients undergoing treatment would do so in weeks to years post-injury (subacute to chronic phase), and to create a stable injury environment that has been used extensively in previous models [28]–[30].

3.1.9. Tissue Preparation

Two weeks after peptide scaffold transplantation, animals were overdosed with Euthasol (J. A. Webster) and then transcardially perfused with 100 mL of ice-cold 0.9% saline and 500 ml of ice-cold 4% paraformaldehyde in phosphate buffer. The spinal cords with injury/transplant area were removed and placed in 4% paraformaldehyde overnight, followed by cryoprotection in 30% sucrose/0.1 M phosphate buffer at 4 °C for at least 3 days. Spinal cords were embedded in M1 medium (Thermo Fischer Scientific) and cut in sagittal sections of 20-µm. Six separate groups of serial sections (approximately 10–15-mm in length) were collected onto glass slides coated with gelatin. Therefore, adjacent

slices on each slide were from levels spaced approximately 120-µm apart within the cord. Slides were kept at 4 °C.

3.1.10. Immunohistochemical Preparation

Sagittal sections were processed for immunohistochemical staining with primary antibodies against GFAP (1:1000, Chemicon) for astrocytes, GFP (1:1000, Millipore) for both GFP labeled HCMECs/D3 and HBVP, Tuj (1:500, Covance) for axon growth, ED-1 (1:500, Serotec) for macrophage, ZO-1 (1;500, Cell signaling) for tight junction, 5-HT (1:20,000, Immunostar) for serotonergic axons. Sections were washed with phosphate buffered saline, blocked with 10% goat or donkey serum for 1hr at room temperature, and then incubated in primary antibodies at room temperature overnight. Species-specific secondary antibodies (goat anti-mouse, goat anti-rabbit, or donkey anti-goat conjugated to FITC or rhodamine, 1:1000, Jackson ImmunoResearch) were applied for 2 h at room temperature and the slides were cover-slipped with fluoromount-G with DAPI (SouthernBiotech).

3.1.11. Immunohistochemical Analysis

Immunohistological sections (20-µm thickness) were imaged with a Nikon A1 laser scanning confocal microscope. Using Nikon Elements software, z-stacks of these slides were generated. For each animal, four adjacent sections on each slide (covering an approximate height of 480-µm) were chosen at a position based on the approximate location of GFP-positive cells in the high cell density condition, in order to assure similar regions of the spinal cord were analyzed across all conditions. Axons inside the scaffolds were quantified using the multi-point tool in ImageJ. To quantify axon density, the approximate injury area was measured using the freehand selection tool in ImageJ. Axon

densities were calculated by dividing the number of axons by the injury area in each section. Neurovascular interaction was quantified by isolating channels for axons (Tuj) and vascular (GFP) structures and using fast Fourier transforms (FFT) to convert spatial coordinates into Fourier frequency data. Gaussian distributions were fit to this frequency data, and alignment was quantified by comparing distributions generated from axon (Tuj) and vessel (GFP) Fourier frequencies from five histological sections per cell density. To determine significance between these distributions, the difference in mean angles were compared using a paired t-test, with $p > 0.05$ indicating no significant difference between the GFP and Tuj signals. Finally, for the measurement of GFAP and ED-1-positive areas, the freehand selection tool was again used to trace the area of positive staining for each marker for four adjacent sections per animal. Mean and standard deviations of these area measurements were then calculated.

3.1.12. Microvessel Quantification

In order to identify the presence of lumens within the peptide scaffold, multicellular structures identified in the maximum projection of the x-y plane were observed in either the x-z or y-z planes to identify the presence of a void within the structure. In the in vitro experiments, the phalloidin stain was used to identify these tubular structures, and the GFP signal was used in the in vivo data. We then measured the length of the microvessels by comparing the maximum projection in the x-y plane to 3D volume views to determine the beginning and end of each microvessel position. This process was completed in both the in vitro and in vivo analyses.

3.1.13. Statistics

One-way ANOVA and post-hoc Tukey's HSD tests were used to calculate statistical significance unless otherwise specified. Statistical significance of the in vitro data and microvessels' quantification were calculated using a Welch Two Sample t-test, assuming normal distributions with unequal variances between groups. Significant difference was denoted with p-values less than 0.05. In vivo measurements (12 animals total) were averaged from 4 histological sections per animal.

3.2. Experimental Methods for Magnetic Alignment of RADA-16I

3.2.1. Hydrogel Preparation

For *in vitro* experiments, peptide hydrogels were constructed by seeding carbonyl iron microparticles (MP) prior to polymerization. 2-mg/mL RADA-16I was mixed with 20% sucrose containing 0.2-wt% MP in a 1:1 mixture to create final concentrations of 1-mg/mL and 0.1-wt% peptide-MP hydrogels. Carbonyl iron magnetic particles (BASF) were obtained to employ magnetic alignment in injectable peptides [119]. A magnetic field of approximately 100-gauss (G) was applied to the hydrogel to induce alignment. Unaligned scaffolds were polymerized in the absence of the field. Scaffold polymerization was replicated by carefully adding Dulbecco's Modified Eagle Medium (DMEM/F12) containing 10% FBS to the hydrogels similar to a previous method [60].

3.2.2. Scanning Electron Microscopy (SEM)

Peptide hydrogels were thoroughly washed and fixed with 5% glutaraldehyde (VWR) for 2 hours at 4°C. After fixation, RADA-16I scaffolds were rinsed with PBS and sequentially dehydrated in 10%, 20%, 30%, 40%, 50%, 60%, 70%, 80%, 90% and 100%

ethanol (VWR) for 5 minutes at room temperature. These samples were lyophilized for 2 hours and sputter coated prior to SEM imaging.

3.2.3. Microfabricated Chamber Fabrication

Unaligned and aligned cell-seeded peptide hydrogels were polymerized inside a polydimethylsiloxane (PDMS)-based device fabricated using soft lithography [32]. Briefly, a chamber was fabricated using positive-feature PDMS stamps with dimensions of 2 mm × 2 mm × 2 mm (L × W × H). The patterned PDMS was cured at 150°C for 7 mins, and then a second layer of PDMS was added on top of the patterned layer to create an enclosed reservoir.

3.2.4. CopGFP Lentiviral Infection

P3 hMSCs cultured in DMEM/F12 were infected with copGFP lentivirus (Santa Cruz) at a MOI of 1 and in culture medium containing 5 µg/mL polybrene for 24 hours. These cells were washed and incubated with DMEM/F12 and exposed to 2 µg/mL puromycin until ~90% of adhered cells expressed green fluorescent protein (GFP). Transfected cells were cultured and used for *in vitro* and *in vivo* experiments.

3.2.5. In-Vitro Alignment and Infiltration

Human mesenchymal stem cells (hMSCs) were cultured in DMEM/F12 containing 10% FBS (VWR) and 1% penicillin-streptomycin (VWR) until confluent. hMSCs were resuspended in 10% sucrose, 0.1 wt% MPs and 1 mg/mL peptide hydrogels at a density of 7.5×10^6 cells/mL, given previous studies have shown that hMSCs promote functional recovery [120], [121]. Following resuspension, the cell-MP-peptide solution was injected into the chamber of the microfabricated device and DMEM/F12 was carefully added to initiate polymerization. A 100-G field was applied to the gels during polymerization to

align fibers, with unaligned hydrogels used as a negative control. To interrogate the effects of hMSCs on promoting axon infiltration, aligned acellular MP-peptide hydrogels were used as an additional control condition.

In order to simulate axon infiltration, 21×10^6 cells/mL of rat-derived E14 neural progenitor cells (NPCs) were seeded on the surface of acellular and cell-seeded peptide scaffolds to interrogate the effects of magnetic alignment on axon alignment. NPCs were isolates using a previously published protocol [122]. Hydrogels were cultured in DMEM/F12 supplemented with 20 ng/mL neurotropic factor-3 (NT-3) (PeproTech) to maintain the viability of NPCs and facilitate their differentiation to neuronal restricted precursors (NRPs), distinguished by Tuj^+ staining.

3.2.6. Immunocytochemistry

Devices were fixed in 4% paraformaldehyde (Alfa Aesar) at room temperature for 20 min. Afterwards, MR-peptide hydrogels were permeabilized with of 0.2% Triton X-100 (Sigma) for 20 min and blocked by 10% normal donkey serum (NDS) (Sigma) for 10 min at room temperature. These gels were incubated with 1:500 Tuj-1 (BioLegend) and 2% NDS for 2 hours followed by incubation of 1:500 DAPI, 1:50 Texas-red phalloidin and 1:500 DyLight 650 conjugate. Images were acquired on a Nikon A1 laser scanning confocal microscope.

3.2.7. Total BDNF Quantikine ELISA

Supernatants were obtained from each condition and total BDNF concentrations were measured using a quantikine ELISA kit (R&D Systems). BDNF-concentrations were prepped and quantified using the manufacturer's protocol. Briefly, supernatants were added onto each well and thoroughly washed, then secondary antibodies and color reagents

were added. Absorbances were read at 450 and 540 nm and the corrected absorbances were taken by the difference between the two wavelengths.

3.2.8. Spinal Cord Surgery and Transplantation

In vivo surgeries were performed at the Drexel University Queen Lane Medical Campus. The Institutional Animal Care and Use Committee of Drexel University College of Medicine approved all animal procures and these experiments were proceeded according to the National Institutes of Health (NIH) Guide for the Care and Use of Laboratory Animals. Six female Sprague-Dawley rats (225-250 g) were housed with a 12-h/12-h light/dark cycle in this work. These rats were administered with 5% of isoflurane until unconscious and the concentration of anesthesia was reduced to 3% during surgery. To induce contusion spinal cord injuries, a laminectomy was performed at C5 and a force of 150 kdyne (impactor tip diameter: 2 mm, Precision Systems and Instrumentation, LLC) was applied to the cord. Muscles and skin were sutured and Buprenex (0.015 - 0.02 mg/kg, Reckitt Benckiser) was subcutaneously administered post-surgery. The rats received cyclosporine A (Sandimmune; Novartis Pharmaceuticals) subcutaneously at a dose of 1 mg/100 g/day 2-3 days prior to transplantation.

Two weeks after injury, rats were anesthetized with isoflurane and lesion area was re-opened during scaffold injection. GFP-labeled hMSCs from confluent plates were washed and suspended in 10% sucrose at a density of 7.5×10^6 cells/mL. The cell solution was centrifuged and the pellet resuspended in 20% sucrose and 0.2-wt% MP and self-assembling peptide, yielding final concentrations of 10% sucrose, 0.1-wt% MP and 1-mg/mL RADA-16I. Prior to injection, permanent magnets were placed under the rat to direct the magnetic field along the rostral-caudal direction. The peptide solution was mixed

immediately before injection in both acellular and cell-seeded conditions. 10 µL of peptide containing 0.1 wt% of MP was injected at a rate of 50 nL/s into the injury site as acellular controls (n = 2). Additionally, four rats received 10 µL of cell-seeded MP-peptide scaffolds with a density of 7.5×10^6 cells/mL and divided the animals into two groups: without magnetic field (unaligned) and magnetic field applied (aligned). Peptide hydrogels polymerized due to injection into physiological pH. Our previous rheological data indicates polymerization occurs within 90 seconds [60]. Furthermore, to ensure rostral-caudal alignment, the magnetic field remained in place until suturing was finished. Thus, 6 total rats were used for these studies. Muscles and skin were sutured and closed with clips. Buprenex (0.015 – 0.02 mg/kg) was subcutaneously administered after the surgery and cyclosporine A treatments were continued daily until the end of the experiments. Animals were sacrificed 2 weeks after peptide injections.

3.2.9. Tissue Preparation

Two weeks following peptide injections, rats were overdosed with Euthasol (J. A. Webster) and transcardially perfused with 100 mL of 0.9% saline and 500 mL of 4% paraformaldehyde in phosphate buffer. Spinal cords were removed and incubated in 4% paraformaldehyde overnight and cryoprotected with 30% sucrose/0.1 M phosphate buffer at 4°C for 3 days. The cords were transferred to M1 medium and cryosectioned with thicknesses of 20 µm. Sagittal sections were separated into six groups (approximately 10 – 15 mm in length) with gelatin coated glass slides. Adjacent sections on glass slides were approximately 120-µm spaced apart within the cord and the histological slides were kept at -20°C.

3.2.10. Immunohistochemical Preparation and Analysis

Histological sections were thoroughly washed and blocked with 10% goat or donkey serum, for 1 hour prior to immunohistochemical staining. Sections were selected for immunohistochemical staining using primary antibodies against GFP (1:1000, Millipore) for hMSC, Tuj (1:500, Covance) for axon growth, GFAP (1:1000, Chemicon) for astrocytes, ED-1 (1:500, Serotec) for macrophage, 5-HT (1:20,000, Immunostar) for serotenergic axons, CGRP (1:2000, Peninsula) for peptide and regenerating sensory axons, and GAP43 (1:1000, Millipore) for regenerating axons. These sections were incubated in primary antibodies overnight at room temperature followed by incubating in species-specific secondary antibodies (goat anti-mouse, donkey anti-goat, or goat anti-rabbit conjugated to FITC or rhodamine, 1:1000, Jackson ImmunoResearch) for 2 hours at room temperature. Sections were cover-slipped with fluoromount-G with DAPI (SouthernBiotech).

Histological sections (thickness: 20-µm) were imaged using a Nikon A1 laser scanning confocal microscope and z-stacks were generated using the Nikon Elements software. To determine the location of the scaffolds, brightfield imaging was used to identify the MPs and 488 laser was used to locate GFP^+ cells within the scaffolds and ensure similar regions across all conditions. Three adjacent sections on each slide (with an approximate height of 360- µm) were imaged and analyzed. Tuj^+ axons, $GAP43^+$ axons, 5-HT fibers and CGRP-fibers inside the scaffolds were quantified using the multi-point tool in ImageJ. Axon densities were calculated by measuring the injury area using the freehand selection tool in ImageJ and dividing the number of axons by the injury area of each histological section. Axon alignment was quantified using the angle tool by drawing a line

with two points in the DIC channel and the third point in the TRITC channel to create an angle between the axons and direction of the magnetic field. Finally, inflammatory responses were calculated by normalizing the intensity of ED-1 within the scaffold to the maximum intensity of an 8-bit image. Mean and standard deviations of the infiltrated axons, glial scars and ED-1 intensities were then calculated.

3.2.11. Alignment Quantification

Fiber alignment was quantified using fast-Fourier transforms (FFT) to convert spatial coordinates to Fourier frequencies and these frequencies were fit into a Gaussian distribution. Elongation factor (E) was quantified using the previous protocol [123]. Briefly, the longitudinal axis of each axon was divided by the width of the corresponding axon and subtract by 1.

3.2.12. Statistics

One-way ANOVA and post-hoc Tukey's HSD tests were performed to calculate statistical significance unless stated otherwise. Statistical analysis of the fiber alignment via SEM was calculated using a Welch Two Sample t-test, assuming normal distributions with unequal variances between groups. Significant differences were denoted with p-values less than 0.05. *In vivo* analysis (6 animals total) was averaged from 3 histological sections per animal.

3.3. Experimental Methods for Dynamically Altering Protein Hydrogels

3.3.1. Hydrogel Preparation

Magnetic-responsive (MR) hydrogels were constructed by seeding carbonyl iron microparticles (MPs) into hydrogels prior to polymerization. Hydrogels either consisted of collagen, fibrin, or a mixture of collagen and high molecular weight (2-2.4 MDa)

hyaluronan. Collagen hydrogels were fabricated using a previous method at concentrations of either 2 or 5-mg/mL [124], [125]. 1 mg/mL fibrin hydrogels were polymerized using 1U/mL of thrombin. Hyaluronan was added to the collagen gels without any additional crosslinking. The collagen and collagen/HA concentrations were chosen to match previous studies of astrocyte-seeded hydrogels [126]. MPs were sterilized with 70% ethanol, dried by evaporation, and subsequently submerged in distilled water at a stock concentration of 100 wt% (w/v) 24 hours prior to hydrogel preparation.

3.3.2 Scanning Electron Microscopy (SEM)

Carbonyl iron microparticle were seeded into 5 mg/mL collagen hydrogels with a concentration of 0.1 wt% for matrix characterization. Hydrogels were thoroughly washed and fixed with 5% glutaraldehyde (VWR) for 30 minutes at 4°C. Following fixation, MR-gels were rinsed with PBS and sequentially dehydrated in 20%, 50%, 70%, 90% and 100% ethanol (VWR) for 10 minutes at room temperature. These samples were lyophilized for 2 hours and sputter coated prior to SEM imaging.

3.3.3. Mechanical Characterization

Rheology measurements of collagen-based hydrogels were conducted on a magnetorheometer attachment for a TA Discovery rheometer (TA Instruments). MR collagen hydrogels were deposited directly onto the 37°C surface plate of the rheometer after mixing. A nonferrous 20-mm Peltier plate was set to a gap height of 300 µm. 1% cyclic strain at a frequency of 1 Hz was applied to the MR gels for a total time of 900 s, with no magnetic field applied during the first 300 s. Magnetorheological properties were measured after hydrogel polymerization for the remaining 600 s. Each magnetic pulse was axially applied for 20 s, with an initial field strength of 500 Oersted (Oe), followed by 2000

Oe and then 4000 Oe. The storage and loss moduli were used to evaluate the tunable mechanical properties of the magnetic-collagen hydrogels. In order to determine whether the direction of the field altered the rheological results, MR collagen hydrogels were polymerized on a non-ferrous Peltier plate (gap height: 24-µm) of a DHR-2 rheometer (TA Instrument) with a 20-mm non-ferrous plate. The cyclic strain and frequency settings matched experiments using the magnetorheometer. A magnetic field of 500-Oe was applied in the transverse direction using permanent magnets. The rheology of fibrin- and PDMS-based materials was measured with an Anton Paar rheometer (MCR502, Anton Paar GmbH, Germany) equipped with a temperature-controlled electromagnet that produces a uniform field perpendicular to the face of a disk-shaped samples between parallel plates. The sample diameter was 20 mm and height varied from 0.3 to 1 mm. Shear storage and loss moduli (G' and G", respectively) were measured as a function of magnetic field at 1% shear strain a frequency of 10 rad/s.

In order to visualize MP displacement within fibrin hydrogels, unpolymerized hydrogels were added to a transparent stage and a 20-mm flat disk applied controlled levels of shear stress using a Bohlin rheometer. For these experiments, a constant magnetic field of 1000-Oe was applied horizontally across the disk-shaped hydrogel using permanent magnets. The instantaneous MP deformation was tracked during the initial application of shear stress, and then tracked during the creep period while the rheometer tracked creep angle.

3.3.4. Confocal Microscopy

Confocal microscopy was used to examine whether the application of the magnetic field caused carbonyl iron MP displacement. For these experiments, 1 wt% of Nile-red

magnetic MPs were embedded in 2 mg/mL and 5 mg/mL collagen hydrogels. After suspending the MPs, gels were either immediately transferred to the stage of a Nikon A1 laser scanning confocal microscope or incubated for an hour to polymerize. Images were taken with a 40X oil immersion objective (Nikon) to visualize displacement over a total period of 40-s. The gels were unmagnetized for the first 20-s and a magnetic field of 2700-Oe was applied to the gel for an addition 20-s for all conditions.

3.3.5. Microfabricated Devices

Cell-seeded collagen hydrogels were polymerized inside a polydimethylsiloxane (PDMS)-based device fabricated using soft lithography [60], [127]. Briefly, a rectangular chamber was fabricated using positive-feature PDMS stamps with dimensions of 4 mm × 6 mm × 2 mm (L × W × H). The feature layers were cured at 150°C for 7 mins. The top of these devices remained open to allow nutrient and oxygen transport. In addition to nutrient transport, we found that adding 3-mm glass spacers on each side of these devices substantially increased cell viability.

3.3.6. Cell Culture

Human coronary artery smooth muscle cells (hCASMC) infected with RFP-LifeAct using an MOI were thawed at passage 6 and cultured in smooth muscle cell growth medium (Lonza) until confluency. P5 normal human astrocytes (NHA) were cultured in astrocyte growth medium (AGM, Lonza) according to a previous protocol [128].

3.3.7. Live Cell Microscopy of hCASMC-Mediated Bead Displacement

Cells were seeded into MR collagen-hyaluronan composite hydrogels at a cell density of 1×10^6 cells/mL. A particle concentration of 0.5 wt% was chosen to visualize local deformation mediated by hCASMCs. Following suspension, the collagen-cell

solution was injected into the central chamber of the microfabricated device and placed in a tissue plastic 35 mm petri dish that contained 5 mL of SMC growth medium. These hydrogels were incubated for 15 min and transferred to a live-cell incubator (Nikon). For gels exposed to a magnetic field, four neodymium magnets (two N52 magnets on each side, 1.5” x 0.5” x 0.125”, BX882-N52, K&J Magnetics) were positioned to apply a horizontally-oriented 500-Oe magnetic field to the hydrogels. Encapsulated cells were imaged using an inverted epi-fluorescent microscope (Nikon) for 3 hours. These images were then analyzed using FIJI and MATLAB.

3.3.8. Cell Viability Assays

To examine the effect of MP concentration on astrocyte viability, P5 NHAs were seeded at a density of 1×10^6 cells/mL into 5-mg/mL collagen hydrogels with the following concentrations: 0 wt%, 0.5 wt%, 2.5 wt%, 5 wt%, 10 wt%, and 20 wt%. After 3 days, cell-seeded hydrogels were washed twice with PBS and stained with 4 mM of calcein AM and 2 mM of EthD-III (Biotium) for 45 minutes at room temperature. Hydrogels were imaged on a Nikon A1 laser scanning confocal microscope. Five frames were used for each condition to quantify cell viability.

3.3.9. Cell Morphology and Mechanotransduction Studies of Normal Human Astrocytes

Similarly, NHAs were seeded into MR collagen hydrogels at a density of 1×10^6 cells/mL. A magnetic particle concentration of 5 wt% was used to increase the effect of the magnetic field on substrate stiffness. The collagen-cell solution was injected into the central chamber of the microfabricated devices, placed in a P100 tissue plastic petri dish, and incubated for 15 minutes. For gels exposed to a magnetic field, eight neodymium magnets (four N52 magnets on top and underneath, 1.5” x 0.5” x 0.125”, BX882-N52,

K&J Magnetics) were positioned with 2-mm spacers to apply a vertically-oriented 7,700-Oe magnetic field. A computational model constructed in COMSOL was used to calculate the magnitude and uniformity of the field in the region of the hydrogels. In order to construct the model, a gauss meter (Model 410, LakeShore) was used to measure the surface field of a single BX882-N52 magnet and at locations 2- and 4-mm removed from the surface. The Br parameter in COMSOL was set at 1.145 to produce the correct surface field (1,780-Oe). The measurements of the gauss meter at 2- and 4-mm from the surface showed good agreement with the computational results . The COMSOL model predicted a field of approximately 7,200-Oe, which was close to the 7,700-Oe field measured by the gauss meter. For negative controls, the same NHA density was seeded into hydrogels without magnetic particles and also exposed to a 7,700-Oe magnetic field. All cell-seeded hydrogels were incubated with AGM throughout the duration of the experiment.

3.3.10. Immunocytochemistry

For immunocytochemical staining, culture medium was aspirated from the gels followed by PBS wash and fixation in 4% paraformaldehyde (Alfa Aesar) at room temperature for 30 min. Gels were then permeabilized with 0.2% Triton X-100 (Sigma) for 30 min at room temperature. MR collagen hydrogels were removed from the central chamber and blocked with 3% bovine serum albumin (BSA) for 30 min at room temperature. The permeabilized hydrogels were incubated with 1:200 yes-associated protein (YAP) primary antibodies overnight at 4°C. These gels were then washed thoroughly with PBS and incubated with 1:250 DAPI, 1:50 TRITC phalloidin, and 1:200 secondary antibody 488 at 37°C for 60 min. Images were acquired on a Nikon A1 laser scanning confocal microscope.

3.3.11. Calcium Transient Measurements in hCASMC-Seeded Hydrogels

To examine the effect of rapidly changing matrix mechanics on cell response, LifeAct-transfected hCASMC were seeded into 2 mg/mL collagen with and without 2.5 wt% MPs at a density of 1×10^6 cells/mL. The cell-seeded hydrogels were incubated at 37°C with smooth muscle cell growth media 24h prior to imaging to preserve optimal spreading. To observe calcium transients in real time, SMCs were incubated with 20 µM Fluo-4 AM (Life Technologies) in DMEM/F-12 medium consisting of 10% FBS, 20 mM HEPES, and 0.25% pluronic acid for 45 minutesMENDELEY CITATION PLACEHOLDER 0. These hydrogels were then washed with F-12 media containing 10% FBS and 20 mM HEPES for 15 minutes and transferred to a live-cell incubator. Images were taken every 1-s for 9 minutes at a wavelength of 488-nm to visualize instantaneous calcium transients with respect to dynamically tuning the mechanical stiffness of the hydrogels. An external field of 2850-Oe was applied to the gels (indicated as "w/ MF") for 3 minutes, removed for 3 minutes ("w/o MF"), and finally reapplied for the final 3 minutes of the experiment. Rheology indicated an increase in storage modulus from approximately 100-Pa to 650-Pa for these conditions. These experiments were conducted with and without magnetic particles to provide a negative control.

3.3.12. Image Analysis

Spreading of NHAs was quantified using ImageJ. Z-stacks images of DAPI/phalloidin stained cells were taken with a laser scanning confocal microscope using a 40X oil immersion objective (Nikon) and condensed to create 2D images. For cell morphology measurements, the freehand selection tool was used to trace the area of the cell. Mean and standard deviations of these morphology measurements were then

calculated. For measurements of cell shape index (CSI) and YAP nuclear localization in 3D, quantification was conducted as previously described [129]. Briefly, binary masks were generated for 3D image stacks of DAPI and actin images by using Otsu's intensity-based thresholding method. The counter function was used to calculate cell volumes (V) and surface areas (A_0). The obtained values were used to calculate 3D CSI using the following equation: $CSI = \frac{\pi^{\frac{1}{3}}(6V)^{\frac{2}{3}}}{A_0}$ [129]. The generated metric defined a line with a CSI of 0 and a sphere with a CSI of 1. For nuclear YAP localization measurements, single cell images were analyzed and quantified. Images were converted into binary masks to create thresholds for each color channel to determine nuclear volume (V_n) and cell cytoskeleton volume (V_c). The counter function was again used to determine V_n and V_c along with the intensity of YAP signal within those regions. The measured values were inserted into the following equation to generate YAP nuclear/cytosolic ratio: $Nuclear\ YAP = \frac{\frac{Nuclear\ YAP\ signal}{V_n}}{\frac{Cytosolic\ YAP\ signal}{V_c}}$ [129]. In order to quantify calcium transients, fluorescent intensities inside of each cell were measured for individual frames during the three phases of the hydrogels. Normalized Fluo-4 fluorescence ratios were expressed as $(F-F_0)/(F_{max}-F_0)$ (instantaneous fluorescence – initial fluorescence/maximum fluorescence - initial fluorescence) to compare differences in calcium cycling. Transients were averaged for each condition, and the initial slope of the transient was measured by fitting a line to the increase in normalized fluorescence.

3.3.13. Statistical Analysis

Two-sample t-tests, one-way ANOVA, two-way ANOVA, and post-hoc Tukey's HSD tests were used to calculate statistical significance. Statistical significance of the

rheological MP deformation was calculated using a paired t-test, assuming normal distributions with unequal variances between groups. For morphology and YAP studies, measurements were averaged from at least 25 cells per condition.

3.4. Experimental Methods for 3D-Printed Scaffolds

3.4.1. Solution Preparation

Dissecting and measuring artificial cerebrospinal fluids were fabricated to maintain the viability of isolated spinal cords using previous methods[130], [131]. Briefly, dissecting artificial cerebrospinal fluid (d-aCSF) was supplemented with 191 mM sucrose, 0.75 mM K-gluconate, 1.25 mM KH_2PO_4, 26 mM $NaHCO_3$, 4 mM $MgSO_4$, 1 mM $CaCl_2$, 20 mM glucose, 2 mM kynurenic acid, 1 mM (+)-sodium L-ascorbate, 5 mM ethyl pyruvate, 3 mM myo-inositol, and 2 mM NaOH. Additionally, measuring artificial cerebrospinal fluid (m-aCSF) was composed of 121 mM NaCl, 3 mM KCl, 1.25 mM NaH_2PO_4, 25 mM $NaHCO_3$, 1.1 mM $MgCl_2$, 2.2 mM $CaCl_2$, 15 mM glucose, 1 mM (+)-sodium L-ascorbate, 5 mM ethyl pyruvate, and 3 mM myo-inositol. The resulting pH of these fluids was ~7.3. All the above reagents were purchased from VWR.

3.4.2. Spinal Cord Preparation

Bovine spinal cords were isolated directly into quart-sized containers of ice-cold dissecting artificial cerebrospinal fluid (d-aCSF) at Bringhurst Meats (Berlin, NJ). After measuring the lengths of the cords, each tissue was divided into three regions: cervical (between 31 and 35 inches from caudal end), lumbar (between 20 and 26 inches from caudal), and sacral (10 inches from caudal). All regions were cut along the transverse anatomical plane, and then immersed in m-aCSF for testing.

3.4.3. Spinal Cord Mechanical Characterization

All spinal cord mechanics were examined within 1 to 2 hours after extraction and experiments were done within 7 to 8 hours, as previous studies have shown that cords preserved in aCSF maintain their mechanical properties over this timespan[130]. The local mechanics of the gray and white matter were examined using AFM. Spinal cord sections were fixed to the petri dishes using transglutaminase that has been shown as a tissue adhesive[132] and fully embedded in m-aCSF during these measurements. AFM measurements were taken in triplicates in regions of both gray and white matter using a 20-μm diameter silicon spherical tip with a cantilever spring constant of 0.6 N/m.

Rheology was conducted at several levels of compressive strain to characterize the macroscopic mechanical properties of the cord at different regions. Measurements were conducted on a rheometer (Kinexus) with a 20-mm parallel attachment. During rheological measurements, m-aCSF was pipetted around the tissue to prevent the cord from drying out. The gap was set with respect to the height of each spinal cord section. The bulk mechanical properties of the cords were evaluated by measuring the shear modulus at a steady frequency of 1 Hz and 1% strain for 90 seconds. The test was repeated for successive compression steps of 100 μm.

A Kibron tensiometer was used to measure the relaxation effects of the gray and white matter of bovine spinal cords. Tissue sections were submerged in m-aCSF during relaxation measurements. A 500-μm probe was lowered in the gray and white matter to interrogate the relaxation profiles within each matter region. The relaxation factors were calculated by measuring the decay in force with time after indentation.

3.4.4. Synthesis of Polymer and Photoinitiator

The polymers and initiators for the prehydrogel solutions, including gelatin methacrylate (GelMA) and lithium phenyl-2,4,6-trimethylbenzoylphosphinate (LAP), were synthesized as previously described [24]. In brief, GelMA was synthesized through dropwise addition of methacrylic anhydride to 10 wt% gelatin (Sigma, derived from porcine skin; type A; gel strength 300) in carbonate/bicarbonate buffer for 4 hours at 50-55 °C, then precipitated in ethanol. The precipitate was allowed to dry for multiple days before resuspension at 20 wt% in PBS. GelMA was sterilized with 0.22 µm filters and stock solutions were aliquoted then stored at -20 °C until use. LAP was prepared by the reaction of dimethyl phenylphosphinite and 2,3,6-trimethylbenzoyl chloride under argon overnight at room temperature. Then 4 molar excess lithium bromide dissolved in 2-butanone was added to the reaction mixture. The solution was heated to 50 °C for precipitation (~10–30 min), cooled to room temperature for 4 hours then filtered with 2-butanone and diethyl ether. The resulting precipitate was allowed to dry for several days before storing under nitrogen at 4 °C until use. Stock solutions were prepared at 200 mM in PBS, sterile filtered, and protected from light until use.

3.4.5. Preparation of 3D-Printed Scaffolds

For all fabrication of hydrogel scaffolds, prehydrogel mixtures were prepared containing 15 wt% GelMA, 17 mM LAP, 2.255 mM tartrazine photoabsorber, and 10% glycerol in sterile 1x PBS. The Volumetric-α Bioprinter used in fabrication was previously developed by the Jordan Miller lab and Volumetric [24]. This stereolithography-based 3D printer used a polydimethylsiloxane (PDMS) coated Petri dish as a vat for the prehydrogel mixture and a build platform with a bonded frosted-glass slide onto which the cured gel

would attach during printing. After transferring the prehydrogel solution into the vat, the build platform was then lowered to the first fabrication layer position to start printing. A custom Matlab script was used to create the 2D photomasks from a 3D model. Grayscale patterning was the method used for outputting a hydrogel with the desired mechanical heterogeneity of localized regions within this specific aim. The grayscale patterning uses light intensity values between 0-100%, representing black to white, to change the extent of polymerization of the hydrogel. This process included an analysis of the 3-dimensional model, separating them into even 50-µm sections in the z-direction, then applying the grayscaled pattern on top of the resulting slices to create the final photomasks. A built-in software on the printer was used to import the photomask and control the apparatus by sending GCode commands for vertical movement of the build platform and images to the projector. The photomasks are projected in sequence for a set exposure time of 14.5 seconds and light intensity of 20 mW/cm^2 (at 100% grayscale) for each projection to build the 3D hydrogel object through layer-by-layer photopolymerization. After printing was complete, the 3D fabricated hydrogels were removed from the glass slide of the build platform with a razor and equilibrated in multiple sterile PBS washes. The 3D models of L4 rat lumbar regions of the spinal cord were created in Blender. The grayscale light intensity value for the simulated white matter was 75% and the gray matter was 100%. The hydrogels were printed in groupings of 8.

3.4.6. Scanning Electron Microscopy (SEM)

The microstructure of 3D-printed GelMA hydrogels was examined using a scanning electron microscope (FEI SEM). The scaffolds were frozen with liquid nitrogen and lyophilized for 2 hours. The freeze-dried samples were cut in cross-section and sputter

coated for 30 seconds per sample. The porosity was analyzed by measuring pore diameters with the measure function in ImageJ.

3.4.7. Scaffold Mechanics Characterization

Raster scans (100 µm x 100 µm) were performed to generate force-distance curves on regions within the regions of gray matter, white matter, and regions that contain both the gray and white matter. The scaffolds were submerged in PBS during the AFM experiments. Measurements were employed using a 20-µm silicon spherical tip with a spring constant of 0.6 N/m. For compression experiments, elastic moduli of 3D-printed scaffolds were performed using a Shimadzu mechanical tester with a 15-mm parallel plate and a 1 kilo-Newton (kN) sensor. A strain rate of 10%/s was used to apply compression to the 3D-printed constructs.

3.4.8. Spinal Cord Surgery and Transplantation

Animal surgeries were conducted at the Drexel University Queen Lane Medical Campus. All animal procedures were approved by the Institutional Animal Care and Use Committee of Drexel University College of Medicine and these experiments were performed according to the National Institutes of Health (NIH) Guide for the Care and Use of Laboratory Animals. Six female Sprague-Dawley rats (225-250 g) were housed with a 12-h/12-h light/dark cycle in this specific aim. These rats were administered with 5% of isoflurane until unconscious and the concentration of anesthesia was reduced to 3% during surgery. To inflict transection spinal cord injuries, a laminectomy was performed at the thoracic 10 (T10) and aspiration was performed to remove the tenth level of the thoracic. Upon transplantation, two scaffold conditions were employed: 1) homogeneous hydrogels that exhibit the same mechanics within the gray and white matter and 2) heterogeneous

scaffolds that mimic the differences in gray and white matter. Muscles and skin were sutured and closed with clips. Buprenex (0.015 – 0.02 mg/kg) was subcutaneously administered after the surgery. Animals were sacrificed 2 weeks after peptide injections.

3.4.9. Bovine Spinal Cord Immunohistochemistry

Bovine spinal cord sections were fixed with 4% paraformaldehyde on ice for 40 minutes, sectioned at 20 µm thick, and mounted onto gelatin-coated slide. The slides were washed with phosphate buffered saline (PBS) and sections were blocked with 1% bovine serum albumin (BSA) for 30 minutes at room temperature. Anti-myelin primary antibodies (VWR) were diluted at a ratio of 1:200 in dilution buffer consisted of 1% BSA (VWR), 0.3% Triton X-100 (Sigma), and 0.01 sodium azide (VWR) and incubated overnight at 2 to 8 °C. The slides were washed thoroughly with PBS and secondary antibodies were incubated at room temperature for 60 minutes at a ratio of 1:500. DAPI stains were added to each slide for an addition incubation time of 5 minutes at room temperature. Finally, sections were washed and mounted in anti-fade mounting media.

3.4.10. Rat Spinal Cord Immunohistology

Two weeks following transplantations, rats were overdosed with Euthasol (J. A. Webster) and transcardially perfused with 100 mL of 0.9% saline and 500 mL of 4% paraformaldehyde in phosphate buffer. Spinal cords were removed and incubated in 4% paraformaldehyde overnight and cryoprotected with 30% sucrose/0.1 M phosphate buffer at 4°C for 3 days. The cords were transferred to M1 medium and cryosectioned with thicknesses of 20 µm. Sagittal sections were separated into six groups (approximately 10 – 15 mm in length) with gelatin coated glass slides. Adjacent sections on glass slides were

approximately 120-µm spaced apart within the cord and the histological slides were kept at -20 °C.

Histological sections were thoroughly washed and blocked with 10% goat or donkey serum, for 1 hour prior to immunohistochemical staining. Sections were selected for immunohistochemical staining using primary antibodies Tuj (1:500, Covance) for axon growth, GFAP (1:1000, Chemicon) for astrocytes, and CGRP (1:2000, Peninsula) for sensory axons. These sections were incubated in primary antibodies overnight at room temperature followed by incubating in species-specific secondary antibodies (goat anti-mouse, donkey anti-goat, or goat antirabbit conjugated to FITC or rhodamine, 1:1000, Jackson ImmunoResearch) for 2 hours at room temperature. Sections were cover-slipped with fluoromount-G with DAPI (SouthernBiotech).

3.4.11. Immunohistochemical Analysis

Immunohistological sections (thickness: 20 µm) were imaged on a Nikon A1 laser scanning confocal microscope to generate z-stacks (approximately 10 slices with a 2-µm step size) in the Nikon Elements software. For DAPI quantification, the number of cell nuclei was normalized to the area of each scan (1 mm^2) and the 488 laser was used to identify the presence of myelin within bovine spinal cord sections. Myelin quantification was performed by normalizing the intensity of myelin stains within 1 mm^2 measured areas. For transplantation analysis, three adjacent sections on each slide (approximately 360 µm in height) were scanned and analyzed. Tuj+ axons and CGRP fibers inside the scaffolds were quantified using the multi-point tool in ImageJ. Infiltration distance was analyzed using the measure tool in ImageJ to determine the lengths of which axons infiltrate.

3.4.12. Statistics

One-way ANOVA and post-hoc Tukey's HSD tests were performed to calculate statistical significance unless stated otherwise. Statistical analysis of mechanical heterogeneity was calculated using a Welch Two Sample t-test, assuming normal distributions with unequal variances between groups between the gray and white matter of the scaffolds. Significant differences were denoted with p-values less than 0.05. In vivo analysis (6 animals total) was averaged from 3 histological sections per animal.

Chapter IV

Results

4.1. Vascularization of Self-Assembled Peptide Scaffolds for Spinal Cord Injury Repair

4.1.1. RADA-16I Polymerization Within a Microfabricated Well

Initial experiments were conducted to verify that the RADA-16I hydrogel could support the formation of BSCB-integrity microvessels in vitro within a microfluidic device. Previous studies have demonstrated the ability of RADA-16I to support the growth of microvasculature [47], but vessels exhibiting tight junctions have yet to be fabricated within these scaffolds. First, a microfabricated reservoir created an enclosed, three-dimensional environment for vascularization and featured ports for nutrient and ion exchange with the surrounding culture medium. Fig. 1A shows a schematic of the device indicating the location of the nine ports within the 4 mm × 6 mm × 1 mm rectangular reservoir that encloses RADA-16I hydrogel seeded with cerebral-derived endothelial cells. Fig. 1B provides a photograph of the device, with red food dye (Allura Red AC) added to the sucrose used in the scaffold formulation to indicate the position of the peptide within the device.

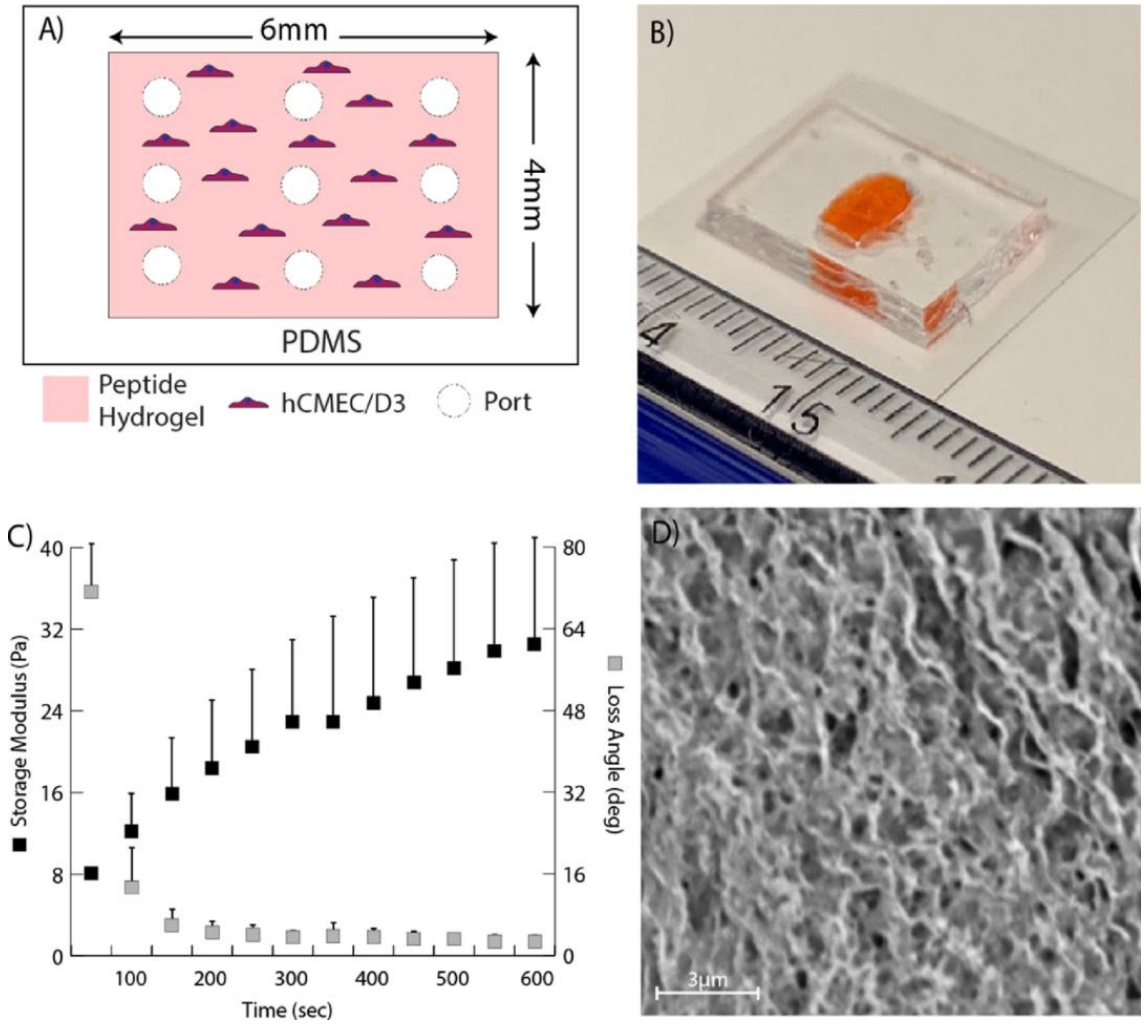

Figure 1. 3D vascularization in vitro. Microfluidic device (A) schematic and (B) photograph. (C) Storage modulus and loss angle of RADA-16I during scaffold polymerization. (D) Scanning electron micrograph showing hydrogel microstructure (scale bar = 3-µm).

Rheology was then used to characterize the mechanical properties of the self-assembling peptide outside the device, and to study the viscoelastic properties during polymerization of the scaffolds. Ten minutes after exposing the peptide to culture medium, the RADA-16I hydrogel reached an equilibrium storage modulus of 31 Pa and loss angle

of 3° (Fig. 1C). These results suggest that RADA-16I is primarily elastic and has a lower storage modulus than both healthy CNS tissue and glial scars that form after CNS injury [31,32]. Scanning electron microscopy (SEM) (Fig. 1D) was used to characterize the microstructure of RADA-16I within the microfluidic device, demonstrating the formation of 59.8 ± 12.7 nm-diameter fibrils and 111 ± 32.0 nm pore sizes, which is consistent with previous analyses of RADA-16I peptide scaffolds [47].

4.1.2. Fabrication of Blood-Spinal Cord Barrier (BSCB) Integrity Microvessels In-Vitro

Having characterized the peptide hydrogel, experiments were conducted to verify that the device could support the formation of BSCB-integrity microvessels within the peptide scaffold. Endothelial cells were seeded into the scaffold and cultured in endothelial medium containing VEGF and PMA, two factors known to induce vascular formation in 3D scaffolds [133]. After five days of incubation in static conditions, actin staining revealed the presence of clearly defined lumens (diameter: 22 ± 6.2 µm, length: 195 ± 70. µm, n = 6) within the multicellular structures, indicating the formation of microvessels within the scaffold (Fig. 2A). In order to determine whether the endothelial cells maintained their tight-junction forming phenotype, the microvessels were stained for zonula occludins-1 (ZO-1), a scaffolding protein that localizes to cell-cell junctions in the BSCB. Confocal microscopy revealed that the microvessels within the RADA-16I hydrogel stained positive for ZO-1 at cell-cell junctions.

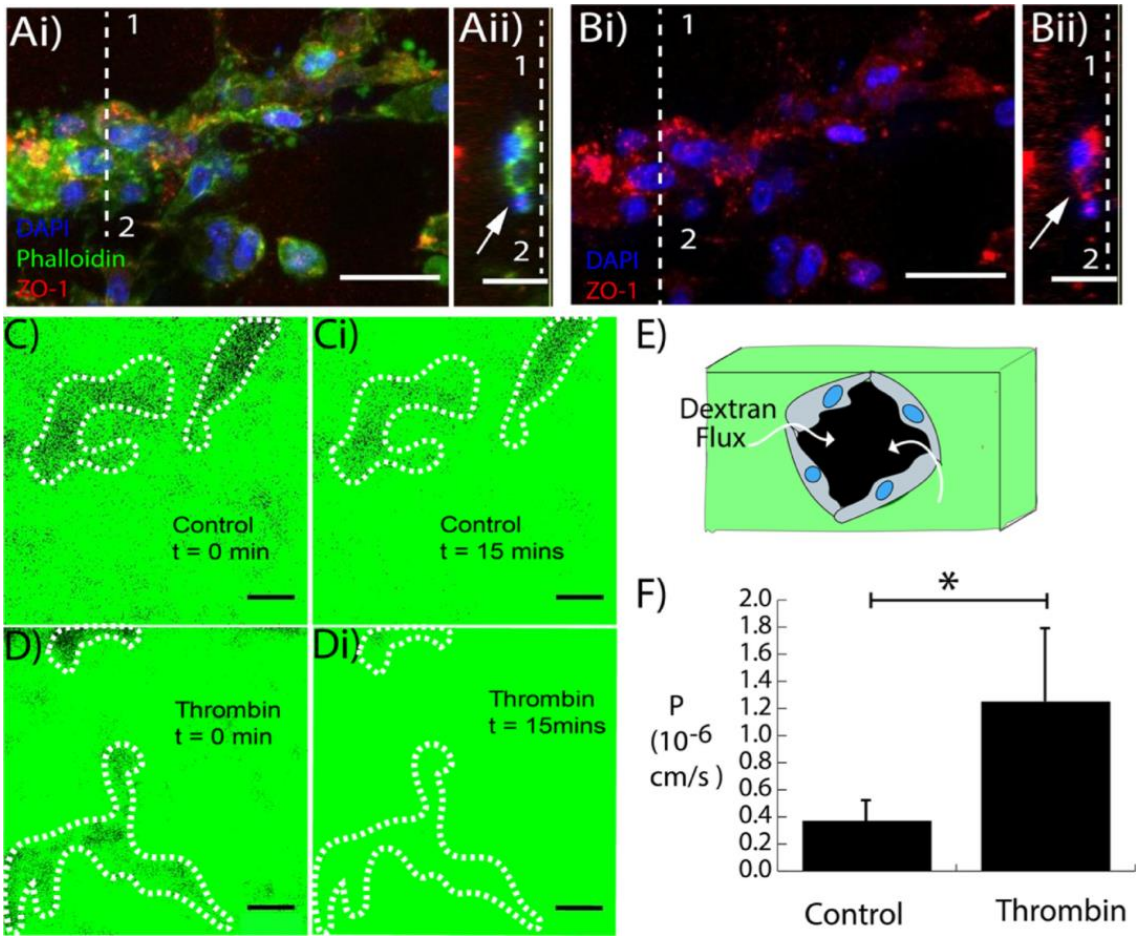

Figure 2. Microvessel formation within RADA-16I peptide scaffolds after 5 days. (A,B) Confocal microscopy stacks (i) and their cross-sections (ii) showing lumens (white arrows) labeled with FITC-phalloidin (green), ZO-1 (red), and DAPI (blue). Scale = 50-µm (Cross-section scale = 15-µm). (C) 4-kDa FITC-dextran permeability test for control conditions at time 0 and 15 min (i). (D) Permeability test with thrombin at time 0 and 15 min (i). White dashed lines display microvessels. Scale = 20-µm (E) Schematic of permeability measurements. (F) Permeability quantification, data presented as mean ± *s*.d. $*p < 0.05$, ($n = 4$).

To further validate the barrier function of these microvessels, permeability testing with 4-kDa dextran was performed to measure transport across the microvessels. Resonance scanning confocal microscopy facilitated high-scan rates (1.5 s per scan) that

measured the diffusion of the dextran into the microvessel lumens at 10-second intervals for a period of 15 min. During that period, a minimal amount of dextran diffused into the lumens of untreated microvessels (Fig. 2C). 10 U/mL of thrombin was added to the surrounding culture medium to disrupt the integrity of the barrier and to serve as a positive control for dextran transport across the microvessel wall, given its ability to disrupt endothelial tight junctions. In the presence of thrombin, dextran was able to diffuse into the microvessel lumens at a faster rate, as shown in Figure 2D. By measuring the rate at which the fluorescence intensity changed within the microvessels, a permeability coefficient was calculated for both the control and thrombin test conditions. The permeability coefficients displayed in Figure 2E indicated that thrombin significantly increased the permeability of the barrier, and that the control permeability agreed with previous results for tight-junction-containing microvessels [32]. The permeability experiments also provided insight into microvessel interconnectivity: there were separate regions of dextran exclusion, indicating multiple and distinct microvessel structures within the scaffold at the five-day time point. Overall, these findings demonstrate the ability of the RADA-16I hydrogel to support the formation of microvessels with BSCB-integrity in an in vitro setting.

4.1.3. Characterization of Microvessel Formation in RADA-16I Post-Transplantation

After demonstrating the formation of microvessels in vitro, a preliminary in vivo experiment was designed to examine whether microvessels would also form in RADA-16I hydrogels after injection into a rat spinal cord injury model. One week after a contusion injury at the cervical level, three scaffold conditions were injected into the site of injury: acellular, low cell density (2.4×10^6/mL), and high cell density (5.0×10^6/mL). GFP-

labeled endothelial cells were combined with GFP-labeled pericytes, due to previous studies that have shown pericytes to support microvessel viability post-transplantation [32]. Cell density was varied to determine whether the delivery of more cells would produce an increased vascular density, given previous results indicating that higher densities of astrocytes in collagen-hyaluronan hydrogels induced hypoxia within the scaffold [125]. Furthermore, the two conditions also yielded insight into whether the response to the transplant was dependent upon the density of cells delivered to the injury.

Immunohistochemistry examined the morphology of microvessels and their interactions with host axons at two weeks post-transplantation. Confocal imaging indicated the presence of clearly defined lumens similar to those observed in vitro in both conditions (Fig. 3A-B). The diameters of these lumens were measured to be 9.0 ± 3.1 μm ($n = 31$) for the low cell density condition and 7.4 ± 2.4 μm ($n = 26$) in the high cell density condition. The microvessel length was also quantified and found to be $99 \pm 60.$ μm ($n = 31$) in the low cell density condition and 100 ± 46 μm ($n = 26$) in the high cell density condition. Two-sample t-tests indicated no significant difference in the number, diameter, and length of the lumens between the two cell density conditions. These measurements are consistent with previous studies that quantified capillary diameters in the blood-brain barrier [134], [135], in microvessels within previously described in vitro scaffolds [32], and in the rat spinal cord, where the smallest vessel diameter was found to be 7.4 μm [136]. Positive ZO-1 staining (shown in the low cell density condition in Fig. 3C) suggested that the microvessels maintained their tight junction phenotype after two weeks following transplantation. The ZO-1 appeared more punctate in vivo compared to the in vitro

microvessels described in Figure 2. This difference could be due to vessel maturity; microvessels were evaluated after day 5 in vitro and after two weeks in vivo.

In addition to characterizing the microvessel structure, neurovascular interaction between the GFP-positive microvessels and Tuj-positive host axons was also quantified. For both cell densities, the microvessels were in close proximity to the surrounding host axons which grew into the scaffold transplant (Fig. 3Aii and Bii, white arrows). To quantify neurovascular interaction, fast Fourier transforms (FFT) were calculated for microvessels and host axons in both cellular conditions to convert spatial coordinates into Fourier frequency data, and Gaussian distributions were fit to this data. Fig. 3D,E shows similar distributions between the two signals for both low and high cell density conditions, which suggests alignment between GFP-positive microvessels and Tuj-positive axons in the site of injury. Paired t-tests were calculated from the difference of means of these Gaussian distributions, and the resulting p-values of 0.39 and 0.72 for low and high cell conditions respectively indicate insignificant differences between the distributions and therefore alignment between the microvessels and axons (Fig. 3F). This result is consistent with previous results regarding neurovascular interaction in the aftermath of SCI.

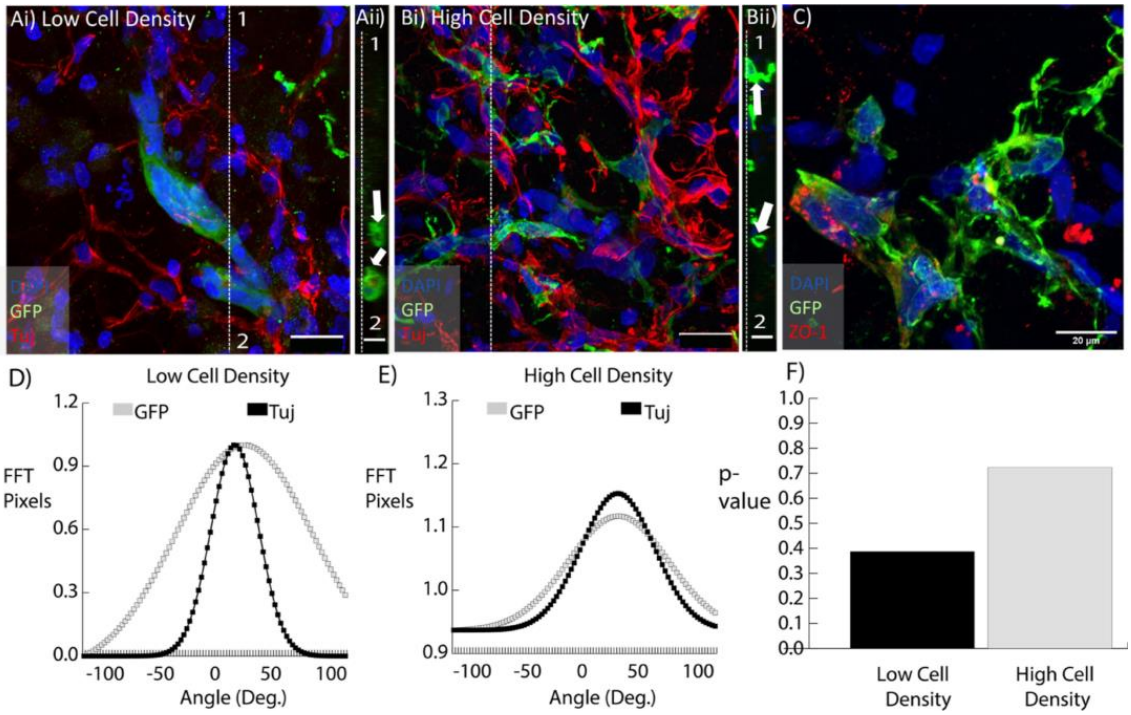

Figure 3. Microvascular structures form in the peptide scaffold following transplantation and facilitate neurovascular interaction. Lumen formation in (A) low cell density and (B) high cell density, (Ai) and (Bi) x-y plane, (Aii) and (Bii) y-z plane, providing an orthogonal view to visualize lumens. DAPI (blue), GFP (green), Tuj (red). (C) Examination of tight junctions in low cell density condition. DAPI (blue), GFP (green), ZO-1 (red). Scale = 20-µm (8-µm for cross-sections). FFT pixels showing alignment of microvessels and axon interaction in (D) low cell density and (E) high cell density. (F) p-values comparing the FFT distributions of GFP-microvessels and axons in both conditions using paired t-tests from the means of the Gaussian distributions (n = 5 per condition).

4.1.4. Cellular Peptide Hydrogels Augment Host Axon infiltration in Spinal Cord Injury Model

Having shown that the scaffold supported microvessel formation in vivo, we interrogated whether the presence of microvessels within the peptide increased the density of Tuj-positive axons at the site of the contusion injury. Due to the nature of contusion injury, we could not distinguish between spared axons and axons infiltrating into the scaffold. Therefore, serial histological sections were imaged in a confocal microscope and stacked to create a volume rendering of the injury site. Supplemental videos 1 (low cell density) and 2 (high cell density) provide 3D renderings of four individual 20-µm sections separated by approximately 120 µm. Representative sections from these stacks are provided in Fig. 4A. As the images show, the scaffolds seeded with microvascular cells resulted in significantly higher axon density in the injury site in both cell-seeded conditions compared to acellular controls (Fig. 4B,C). 5-HT was also probed in these samples to evaluate the potential presence of descending, motor specific tracts. Although there was no significant difference between total axon density, quantification of 5-HT-positive axons indicated that scaffolds seeded with the low cell density resulted in significantly more serotonergic-specific axons at the site of injury compared to both acellular and high cell density conditions (Fig. 4D,E), though the high cell density condition still had a significantly higher number of 5-HT-positive axons than the acellular control.

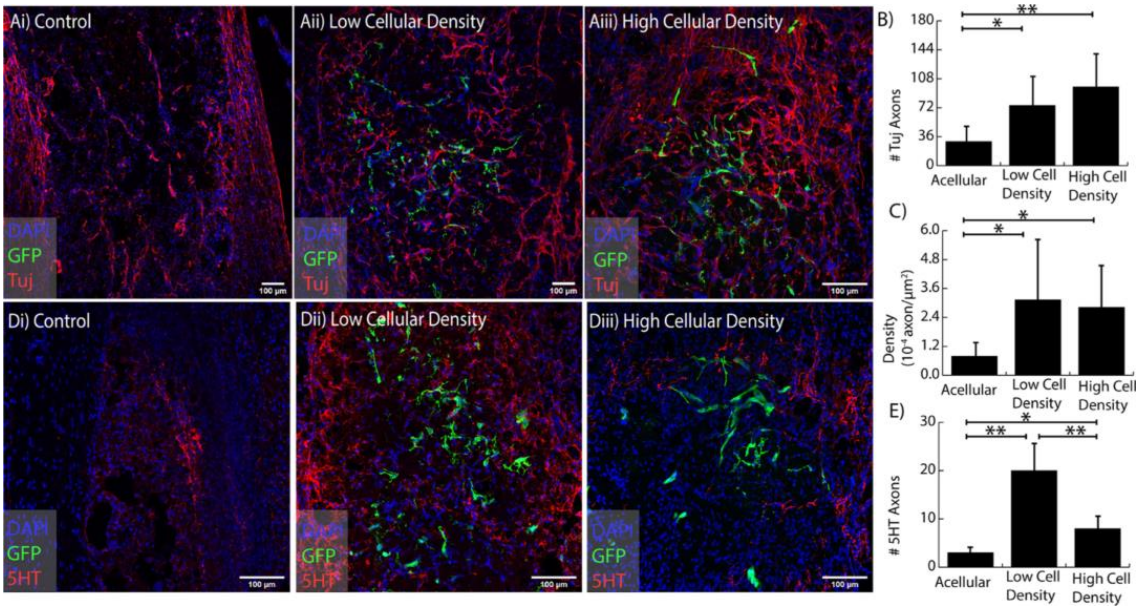

Figure 4. Regeneration of spinal and serotonergic axons in the injury area. General axons stained with Tuj grew into (Ai) acellular scaffold, (Aii) low cell density scaffold, and (Aiii) high cell density scaffold. DAPI (blue), GFP (green), and Tuj (red). (B) General axon quantification. Data presented as mean ± s.d. *$p < 0.05$. (C) Axon density quantification. Data presented as mean ± s.d. *$p < 0.05$ and **$p < 0.001$. Serotonergic axon (5HT) grew into (Di) acellular scaffold, (Dii) low cell density scaffold, and (Diii) high cell density scaffold. DAPI (blue), HCMEC/D3 and HBVP GFP (green), and 5HT (red). (E) Serotonergic axon quantification values. Data presented as mean ± s.d. *$p < 0.05$ and **$p < 0.001$. Scale = 100-µm.

However, staining for GAP43 (Fig. 5) indicated that the high cell density resulted in a significant increase in the presence of regenerating axons within the injury area compared to both the acellular and low cell density condition, though the low cell density condition still had significantly higher GAP43-positive axons compared to the acellular condition. Therefore, whereas low cell density results in significantly higher 5-HT-positive axons, the high cell density results in significantly higher GAP43-positive axons. Overall, these results demonstrate that vascularizing RADA-16I can effectively increase axon

growth and density following SCI, and that characteristics of this response are dependent upon the concentration of microvascular cells injected with the peptide.

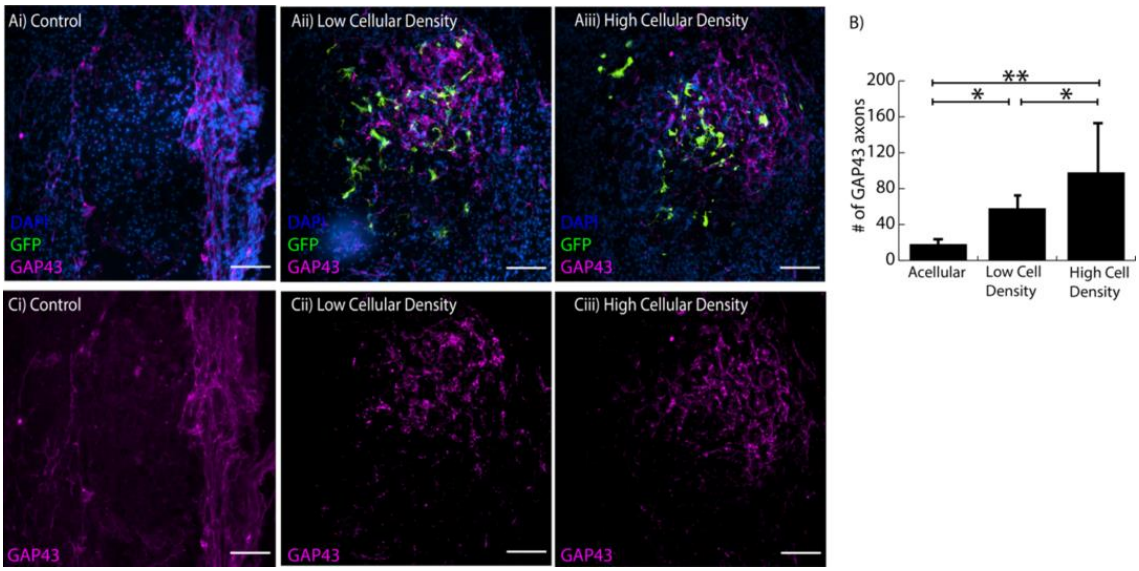

Figure 5. Microvascular structure formation guides axons regrowth. Regenerating axons stained with GAP43 proliferated into (Ai) acellular, (Aii) low cellular density, and (Aiii) high cellular density conditions. DAPI (blue), GFP (green), and GAP43 (magenta). (B) Quantification of GAP43 axons within injury area. Data presented as mean ± s.d. *$p < 0.05$ & **$p < 0.001$. (Ci-iii) provides isolated channel for GAP43. Scale = 100-µm.

4.1.5. Evaluation of Injury Area and Inflammation Following Transplantation

After demonstrating that the presence of microvessels significantly increased the density of both general and serotonergic axons at the injury site, we interrogated the effect of the vascularized peptide on inflammation and scar formation in this region. Antibodies for glial fibrillary acidic protein (GFAP) and ED-1 were used to assess the presence of activated astrocytes and macrophage/microglia, respectively. Figure 6A indicated that the GFAP-positive area was significantly reduced in animals receiving cell-seeded peptide injections, though there was no significant difference between the two cell densities (Fig. 6B). This result demonstrates that the vascularized scaffolds reduced the size of the injury area, given previous studies that have quantified injury area based on GFAP staining [122], [137]. This finding is also consistent with previous studies showing that cell-seeded scaffolds reduce the injury area [138].

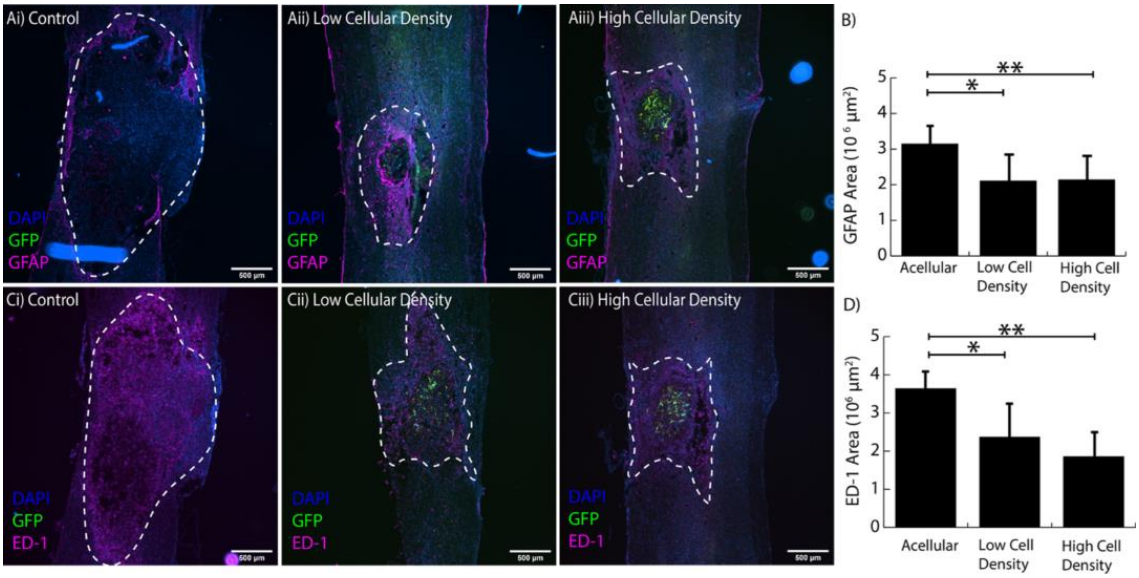

Figure 6. Quantification of injury area and inflammation following injection of peptide hydrogels. Reactive gliosis in response to peptide hydrogels in (Ai) acellular peptide, (Aii) low cell density, and (Aiii) high cell density. DAPI (blue), GFP (green), GFAP (magenta). (B) Injury area quantification. Data presented as mean ± s.d. *$p < 0.05$, **$p < 0.001$ (C) Inflammatory response following scaffold transplantation, (Ci) acellular peptide, (Cii) low cell density, and (Ciii) high cell density. (D) Inflammation area quantification. Data presented as mean ± s.d. *$p < 0.05$, **$p < 0.001$. Scale = 100-µm.

A similar response was found when staining for ED-1. In the acellular condition, ED-1-positive staining was present throughout the injury site. However, the ED-1 staining was localized to the location of the peptide injection in both the low and high cell density conditions (Fig. 6C). Quantification of the positive-ED-1 area indicated a significant reduction in both cell-seeded conditions compared to the acellular controls. Higher magnification images of the GFAP and ED-1 staining are provided in Figure 7. Thus, these results again show that the presence of the microvascular structures within the peptide has a beneficial effect on the healing response.

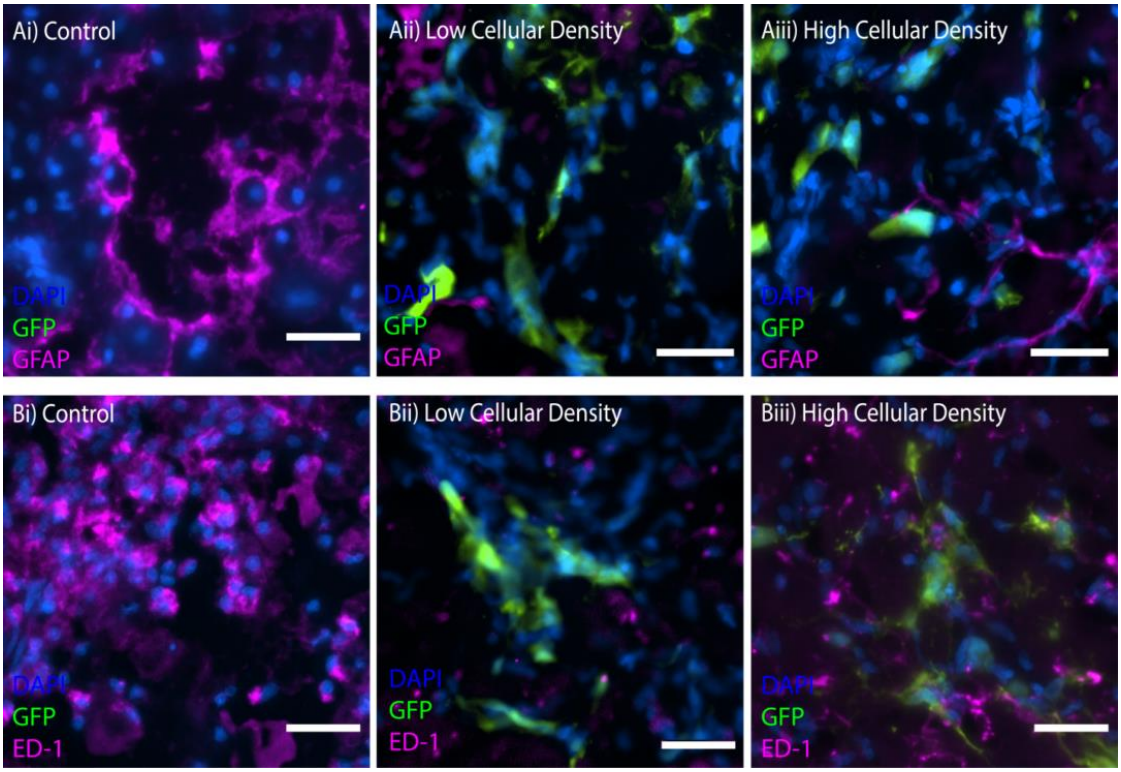

Figure 7. High magnification images of GFAP. (A,Bi) Control (acellular), (A,Bii) low cellular density, and (A,Biii) high cellular density scaffolds. DAPI (blue), GFP (green), and GFAP (A) or ED-1 (B) (magenta). Scale = 35-µm.

4.2. Magnetic Alignment of Injectable Hydrogel Scaffolds for Spinal Cord Injury Repair

4.2.1. Fiber Alignment Within a Microfabricated Device

In vitro experiments were first performed to validate the approach of aligning fibrous networks by applying magnetic fields to hydrogels containing carbonyl iron magnetic microparticles (MPs). Given our previous work using interstitial flow to align microvessels in collagen hydrogels [32], experiments were conducted to determine whether a similar degree of alignment could be achieved by applying magnetic fields to MP-seeded peptide gels. In order to determine the minimum threshold of carbonyl iron particles to facilitate fiber orientations, RADA-16I hydrogels polymerized within a 2 mm × 2 mm × 2 mm (L × W × H) microfabricated chamber were seeded with various particle concentrations: 0.01 wt%, 0.05 wt%, and 0.10 wt%. A 100-G magnetic field was applied to the hydrogels to induce fiber alignment during the polymerization process. Brightfield images demonstrated alignment of MPs under the presence of a 100-G field (Fig. 8A-C) compared to hydrogels polymerized in the absence of a field (Fig. 8D).

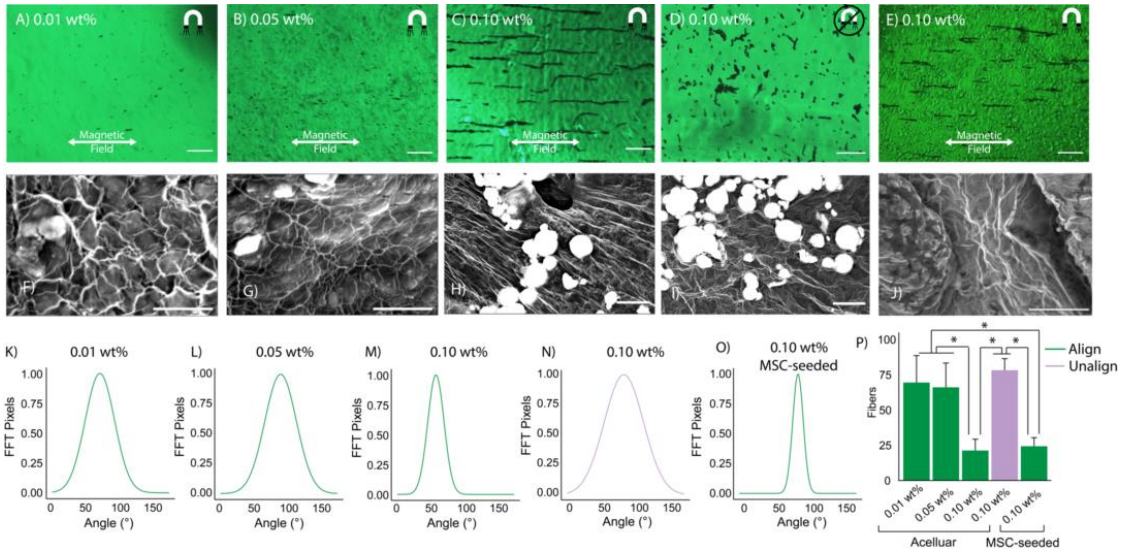

Figure 8. 3D alignment in vitro. (A–E) Brightfield images various concentrations of MPs in peptide hydrogels. Scale = 50 μm. (F–J) SEM images of fibers. Scale = 5 μm. (K–O) Fast-Fourier transform quantification of fiber orientations. (P) Average widths of the FFT distributions. Data presented as mean ± s.d. *P < 0.05.

Furthermore, aligned scaffolds were also seeded with human mesenchymal stem cells at a density of 7.5×10^6 cells/mL to interrogate whether initial cell seeding mitigated magnetic-induced fiber alignment (Fig. 8E). To assess fiber alignment, scanning electron microscopy (SEM) was used to determine fiber orientations with respect to the magnetic field. Although the magnetic field was applied to peptide hydrogels containing 0.01 wt% and 0.05 wt% of MPs (Fig. 8F,G), SEM indicated that fibers were arranged in random orientations. However, Figure 8H demonstrated that the orientation of fibers aligned with the applied magnetic field at a concentration of 0.10 wt% of MPs, indicating a minimum particle threshold needed to align peptide networks. Moreover, peptide hydrogels were

seeded with 0.1 wt% of MPs in the absence of a magnetic field to provide an unaligned control. Figure 8I shows random alignment of fibers without the magnetic field applied. Additionally, cell-seeded scaffolds verified that magnetic-induced fiber alignment was not affected by initial cellular integration (Fig. 8J). In order to quantify the alignment observed by electron microscopy, fast-Fourier transforms (FFT) were calculated from the images. FFT pixels revealed that fibers in the 0.1 wt% MP-aligned condition appeared to have smaller distributions compared to the other conditions (Fig. 8K-O). To quantify these Gaussian curves, the widths of these distributions at their half-heights were averaged across both conditions. Figure 1P shows that the averaged width of fibers exposed to an external magnetic field at 0.1 wt% exhibits a significantly higher correlation to aligned particles. These results are consistent with previous studies regarding magnetically aligned collagen fibers [17].

4.2.2. Facilitated-Orientation of Axon Infiltration In-Vitro

Having demonstrated the ability to align peptide scaffolds using a magnetic field, initial *in vitro* experiments were conducted to interrogate whether fiber anisotropy altered morphology and migration of neural cell types. In these studies, hMSCs were embedded within the hydrogel due to their established neurotrophic effects [120], [121]. A magnetic field of 100-G was applied to both acellular and cell-seeded MP-peptide hydrogels to align the peptide hydrogels. Furthermore, live/dead and BrdU assays validated whether carbonyl iron magnetic particles affected hMSC viability and proliferation in peptide hydrogels with and without the particles. Quantification of viability and proliferation markers indicated no significant difference between MP-seeded and non-MP scaffolds (Fig. 9).

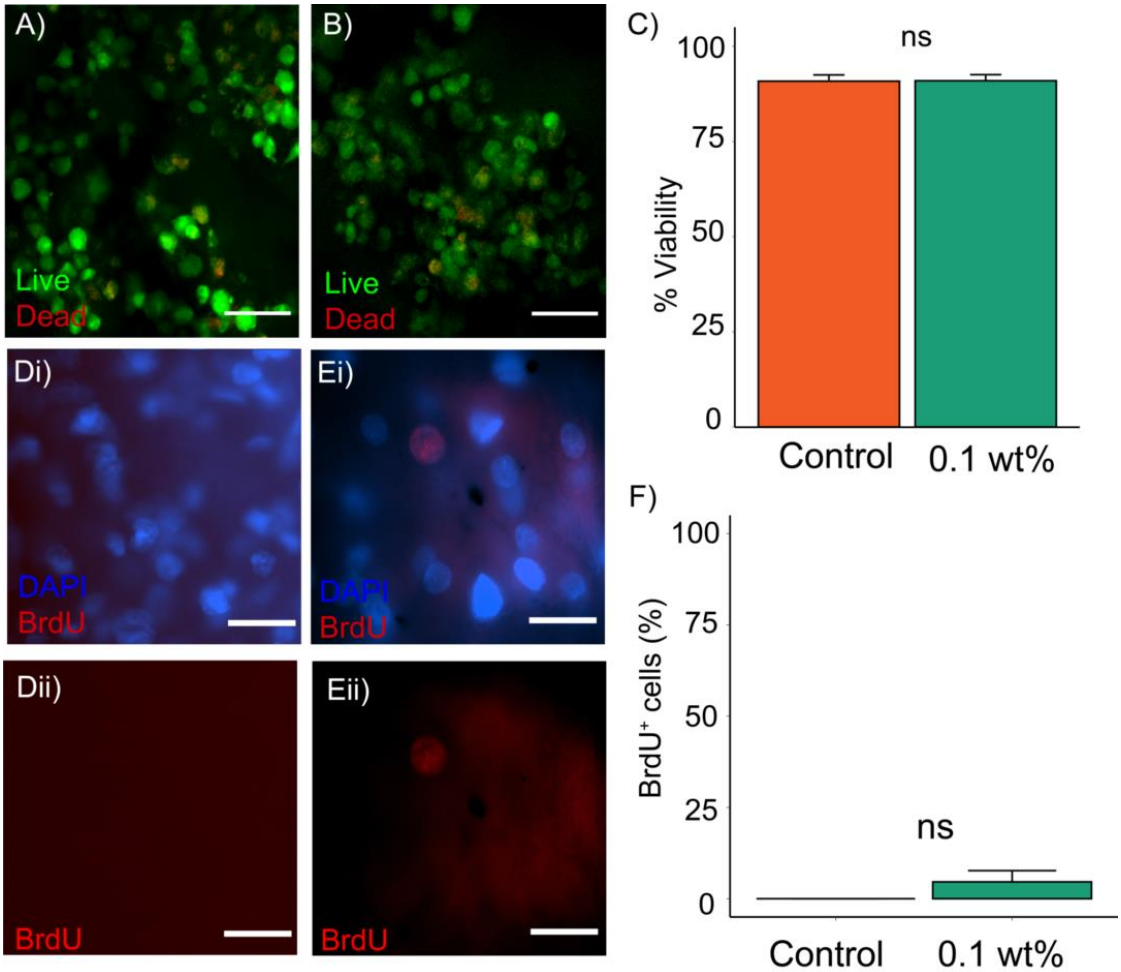

Figure 9. Viability assays in (A) control hydrogels and (B) 0.1 wt% of MPs. Green = calcein AM, Red = ethidium homodimer. Scale = 100 µm. (C) Quantification of live/dead assay. BrdU assays in (D) control (E) and 0.1 wt% MP-seeded hydrogels. Blue = DAPI, red = BrdU. Scale = 25 µm. (F) BrdU+ cells quantification. Data presented as mean ± s.d.

After 4 days of incubation, Tuj stains were used to identify the neuronal phenotype and validate the sufficient timeframe for axon alignment (Fig. 10A). Figure 10Ai shows NPCs attached to the surface of the hydrogels with minimal axon infiltration into the scaffolds in the acellular condition. In contrast, Figure 10Aii-Aiii reveal substantially more

Tuj^+ fibers within hMSC-seeded MP-peptide hydrogels, which is consistent with previous studies given that cell-seeded hydrogels augment axon infiltration following spinal cord injury [60]. Quantification of axon orientation verified that the presence of a magnetic field during polymerization significantly increased alignment along the direction of the magnetic field compared to unaligned controls (Fig. 10B). Figure 10C demonstrates that the elongation factor, E, of Tuj^+ fibers was also significantly longer in the aligned hMSC-seeded peptides compared to the unaligned hMSC-seeded condition, which is consistent with previous observations of topographical cues for neuronal differentiation [139]. ELISAs were conducted to interrogate BDNF in various hydrogel conditions: MP-seeded, MP + hMSC-seeded, aligned MP NPC-seeded, unaligned MP hMSC+NPC-seeded, and aligned MP hMSC+NPC-seeded. Quantification revealed that the aligned scaffolds seeded with hMSCs and NPCs exhibit a significant increase in BDNF concentrations compared to unaligned scaffolds containing both cell types (Fig. 10D). These results are consistent with previous results given that aligned scaffolds improved neurite growth compared to unaligned controls [49], [50]. Overall, these results demonstrate the efficacy of magnetic alignment to direct axon regrowth and differentiation for spinal cord regeneration.

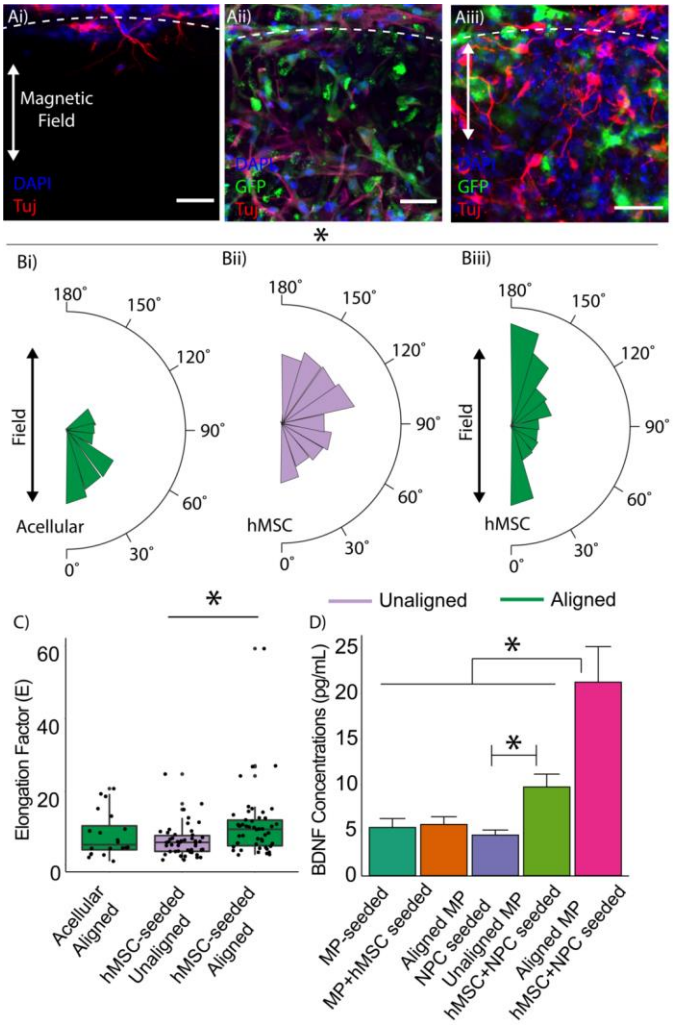

Figure 10. Magnetic alignment of Tuj$^+$ fibers in vitro. Axon infiltration in (Ai) aligned acellular (Aii) unaligned hMSC-seeded and (Aiii) aligned hMSC-seeded peptide hydrogels (white dotted line indicates the approximate edge of the hydrogel). DAPI = blue, GFP = green, Tuj = red. Polar graphs showing axon alignment in (Bi) aligned acellular, (Bii) unaligned hMSC-seeded and (Biii) aligned hMSC-seeded peptide scaffolds after day 4. (C) Elongation factor of infiltrated axons. (D) Total BDNF quantification with respect to each condition. Data presented as mean ± s.d. *P < 0.05. Scale = 50 μm.

4.2.3. Interrogation of Magnetically-Aligned Axons Post-Injection

The *in vitro* experiments verified that 0.1 wt% of MPs were sufficient for scaffold alignment in response to a 100-G magnetic field. These parameters were then extended to a proof-of-concept *in vivo* experiment using an animal model of spinal cord injury. A contusion injury model was used to increase the clinical relevance of these studies. Two weeks following a cervical contusion, several conditions were examined for scaffold injection: (i) acellular with a magnetic field applied, (ii) hMSCs in the absence of a magnetic field, and (iii) hMSCs with a magnetic field applied. A 100-G magnetic field oriented in the rostral-caudal direction was applied by placing permanent magnets spaced 16-mm apart underneath the rat during all injections (Fig. 11A,B). Furthermore, a computational model constructed in COMSOL was used to calculate the magnitude of the field applied to the cord at approximately 20-mm from the center of the magnets (Fig. 11C). Animals were sacrificed and the orientation of infiltrated axons was examined by immunohistochemistry two weeks post-injection. Both confocal and brightfield microscopy were used to identify the location of transplanted GFP-positive cells and MPs.

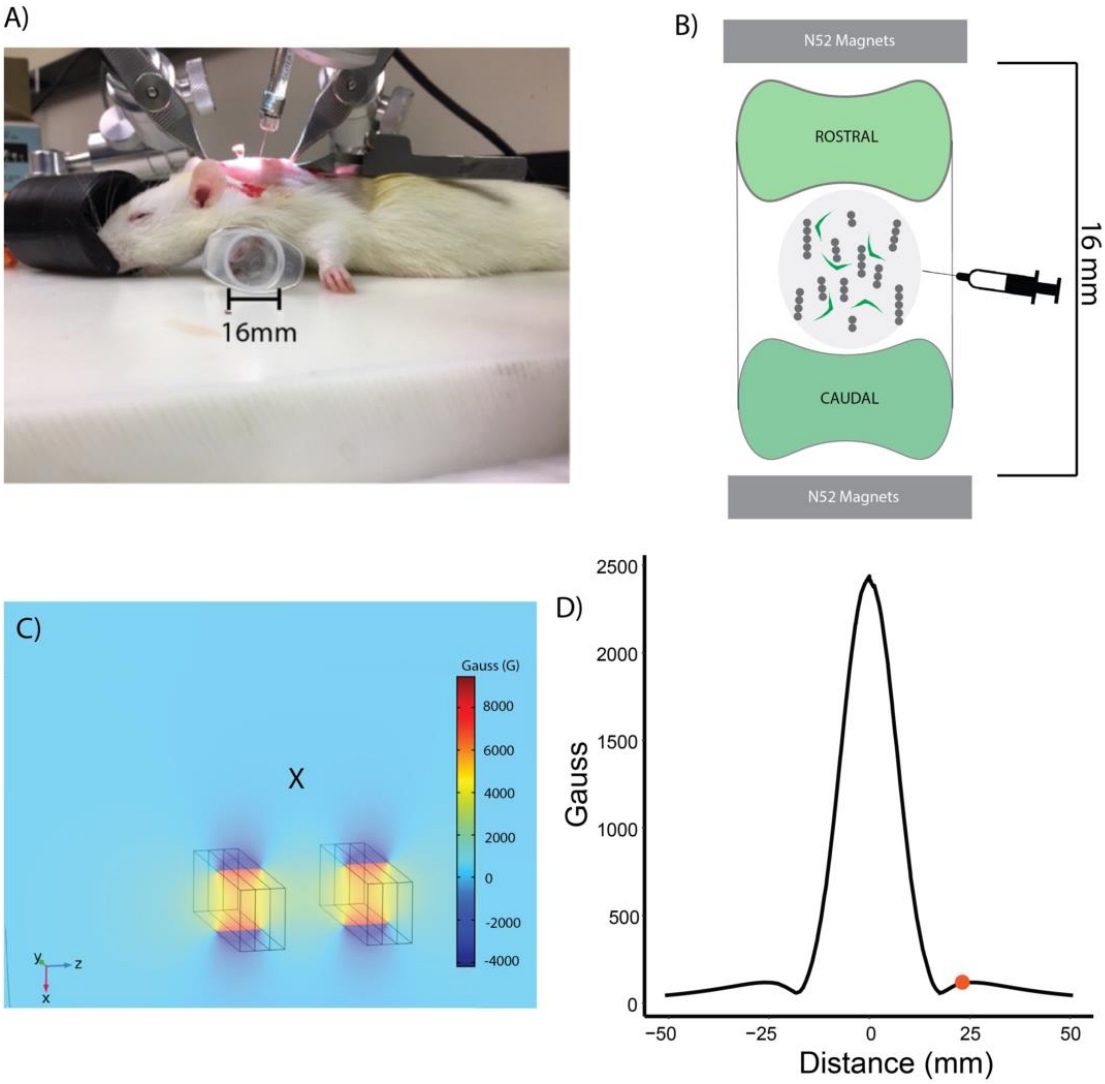

Figure 11. Schematic of post-injection alignment. (A) Photograph of real-time scaffold injection at the cervical 4-5 following contusive spinal cord injury. (B) Schematic of alignment set-up during injection. (C) Computational model of the magnetic field applied to the cord. X indicates the location of the cord with respect to the position of the magnets. (D) Magnetic field strength along the Xdirection. The orange dot reveals the magnetic field strength at approximately 20-mm away from the center of the magnets.

Figure 12A provides low-magnification images of positively-labeled Tuj fibers infiltrating the injection site. Figures 12Bi,Biii focus on segments within the scaffolds highlighting the axons aligned along the rostral-caudal direction while Figure 12Bii shows random orientations of infiltrated axons. Figure 12C shows that MPs are retained following the two-week survival. Alignment quantification showed Tuj^+ fibers in scaffolds exposed to an external magnetic field exhibited orientations along the rostral-caudal direction, consistent with the direction of the field applied during the injection (Fig. 12Di,Dii). In contrast, axons in the unaligned scaffolds displayed random orientations in the absence of the magnetic field (Fig. 12Dii). ANOVA tests with post-hoc Tukey tests revealed statistically significant difference in Tuj^+ fiber orientations between all conditions. Quantification of infiltrated axons demonstrated that scaffolds seeded with hMSC resulted in significantly higher axon infiltration in the injury site compared to the acellular controls (Fig. 12E). Therefore, although application of the magnetic field resulted in significantly higher alignment in acellular and cell-seeded conditions, the presence of cells significantly increased the number of infiltrating axons.

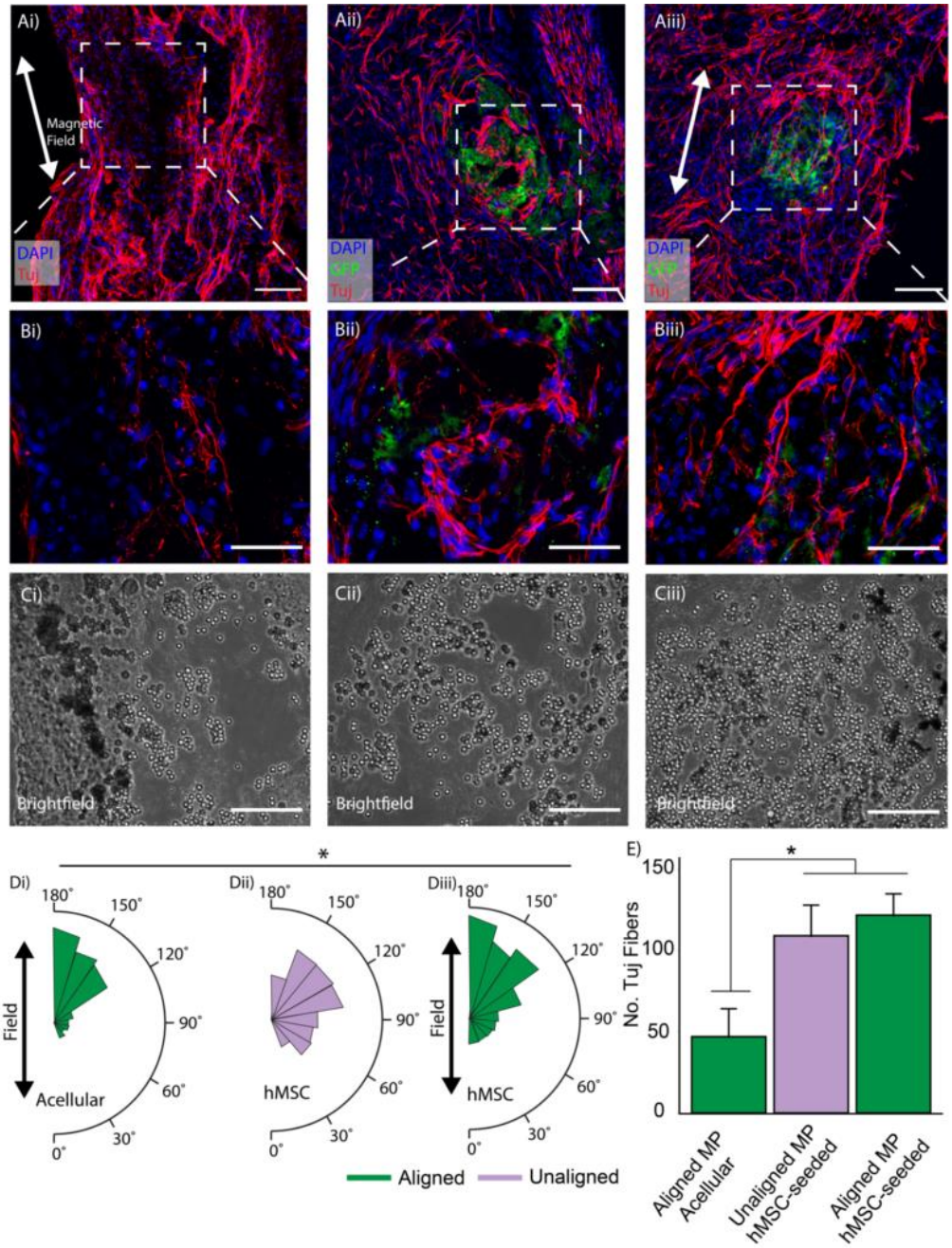

Figure 12. Facilitation of Tuj$^+$ axon alignment following MP-peptide injections post spinal cord injury. Fluorescent images showing axon infiltration in (Ai) aligned acellular, (Aii) unaligned hMSC-seeded and (Aiii) aligned hMSC-seeded scaffolds. White arrows represent the direction of the magnetic field during surgery. Scale = 100 µm. (Bi–Biii) Higher magnification images from A. Scale = 50 µm. DAPI (blue), GFP (green), Tuj (red). (Ci–Ciii) Brightfield images displaying magnetic particles in each condition. (D) Quantification of Tuj$^+$ axon fibers in each scaffold condition. (E) Quantification of axon infiltration with respect to each injected condition. Data presented as mean ± s.d. *$P < 0.05$.

4.2.4. Evaluation of Sensory and Serotonergic Axons Following Transplantation

In addition to evaluating axon infiltration post-injection, we also evaluated the presence of ascending sensory-specific and descending motor-specific tracts within the injected peptide hydrogel. Calcitonin gene-related peptide (CGRP), a peptide widely expressed in sensory neurons [140], and 5-HT, a monoamine neurotransmitter that is essential for modulating locomotion [141], were probed to determine the regeneration of both sensory and serotonergic axons. Figure 13A,B show representative immunofluorescent images of CGRP and 5-HT axons in all three conditions. Quantification of sensory axons demonstrated that cell-seeded scaffolds significantly augmented the CGRP regeneration compared to acellular controls (Fig. 13C). Though the length of CGRP axons were significantly longer in the unaligned hMSC-seeded compared to the aligned hMSC-seeded hydrogels, both cell-seeded scaffolds resulted in significantly longer CGRP length in the injury area compared to acellular controls (Fig. 13D). Interestingly, quantification of 5-HT positive axons indicated no significant difference amongst all conditions (Fig. 13E), suggesting that the incorporation of magnetic particles did not hinder these axons from regenerating into the scaffolds, and additionally that the presence of hMSC did not improve recruitment of these fibers.

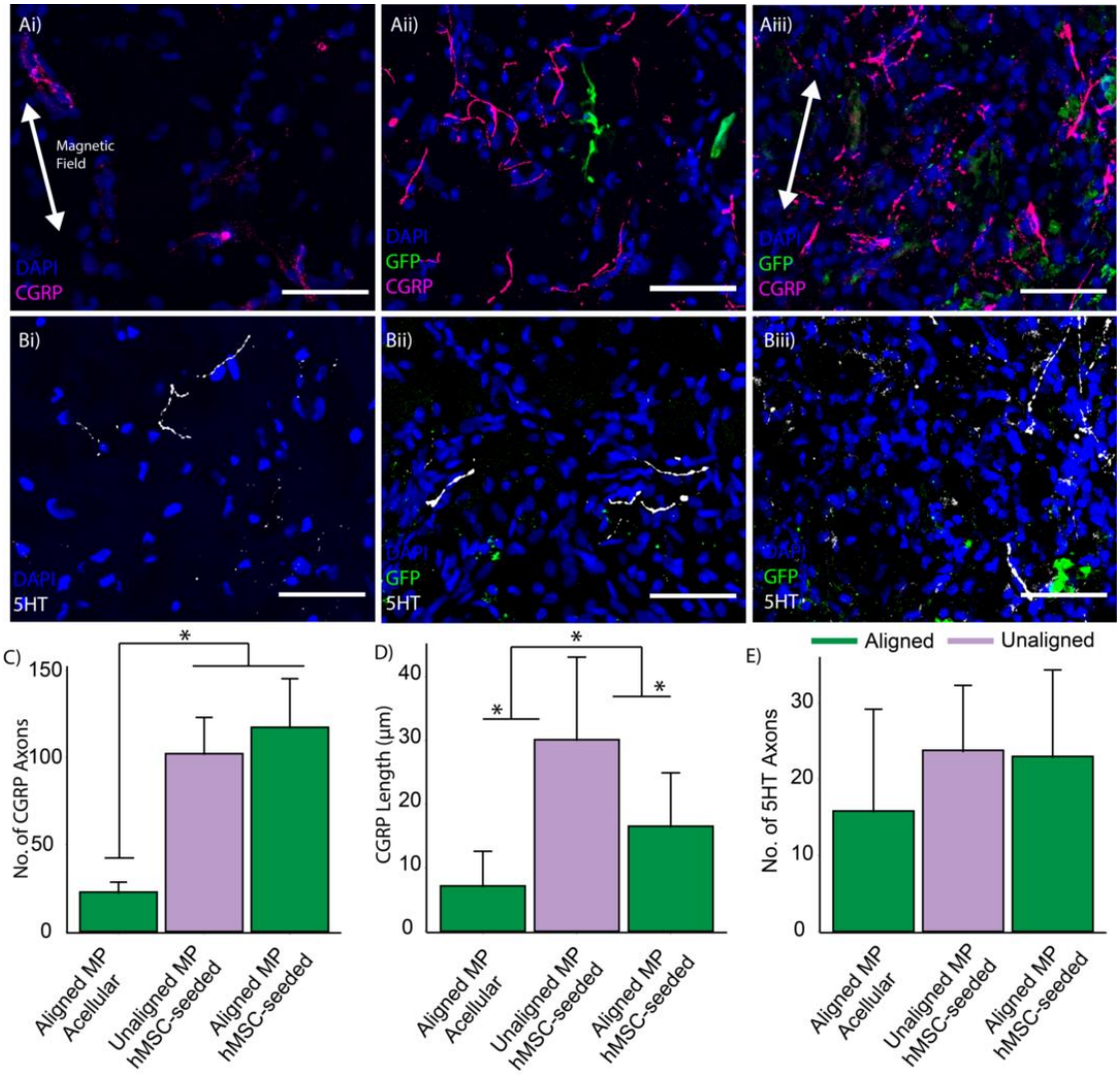

Figure 13. Regeneration of sensory and serotonergic axons at the injury site. (A) Sensory axons stained with CGRP grew into (Ai) aligned acellular, (Aii) unaligned hMSC-seeded and (Aiii) aligned hMSC-seeded hydrogels. DAPI (blue), GFP (green), CGRP (magenta). White arrows represent the direction of the magnetic field during surgery. (B) Serotonergic axons infiltrated into (Bi) aligned acellular, (Bii) unaligned hMSC-seeded and (Biii) aligned hMSC-seeded scaffolds. (C) CGRP axon quantification within the scaffolds. (D) CGRP length quantification. (E) Serotonergic axon quantification values. Data presented as mean ± s.d. $*P < 0.05$. Scale = 50 μm.

Since we could not distinguish between infiltrated axons and spared axons in the contusion injury, growth associated protein 43 (GAP43), a marker for axonal regeneration [142], was used to access the growth of axons within the scaffolds (Fig. 14). Immunofluorescence and quantification revealed a significant increase of GAP43 axons; GAP43 density was augmented within the cell-seeded scaffolds compared to acellular controls. Overall, these results validate that the magnetic particles did not inhibit the growth of sensory and motor tracts, and that axon regeneration was stimulated in the hMSC-seeded scaffolds.

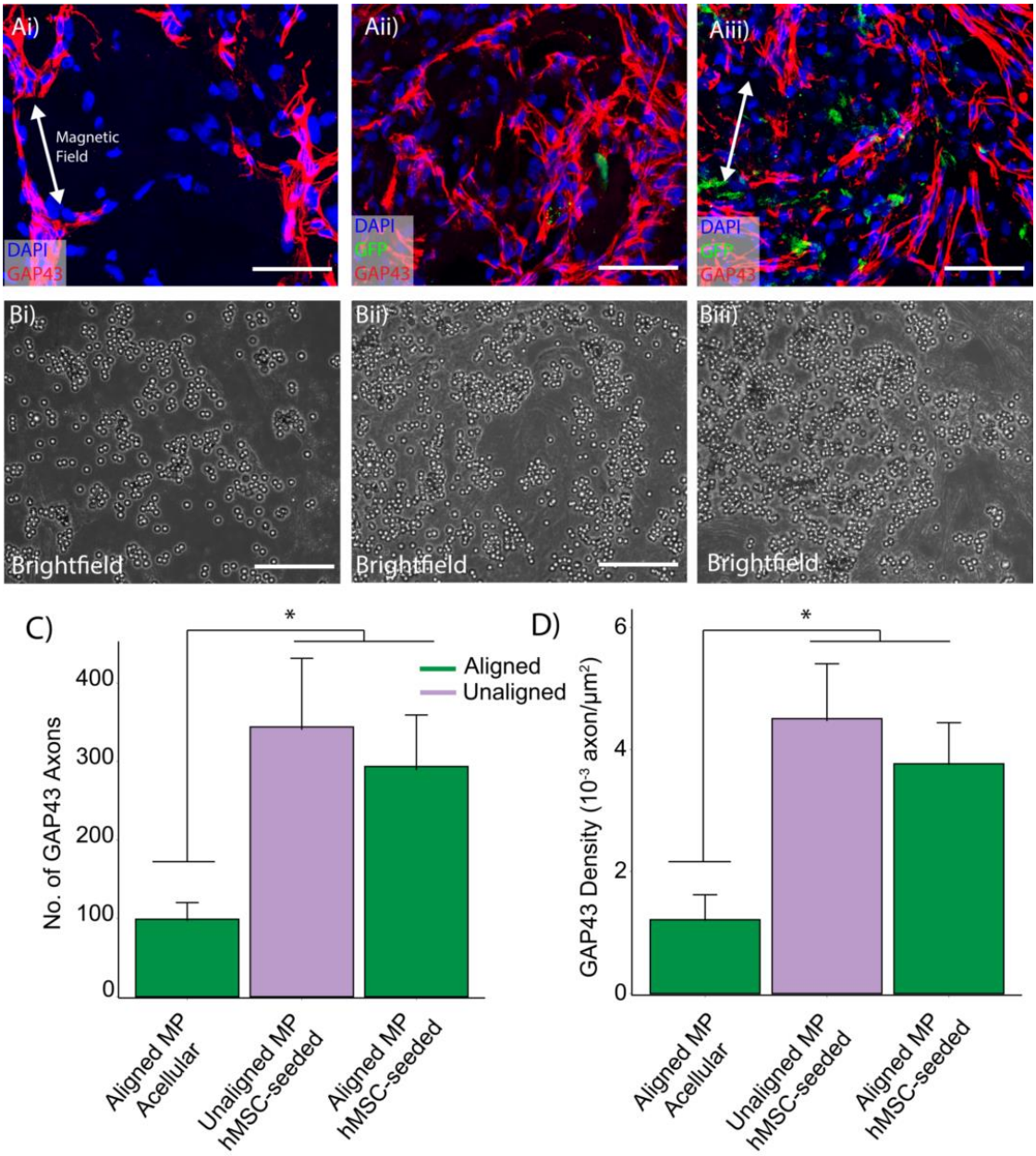

Figure 14. Assessment of regenerated axons post-injection 2 weeks after spinal cord injury. (A) Representative images of GAP43 within (Ai) aligned acellular, (Aii) unaligned hMSC-seeded and (Aiii) aligned hMSC-seeded hydrogels. DAPI (blue), GFP (green), GAP43 (red). (B) Brightfield images of each condition. (C) GAP43 axon quantification. (D) Axon density quantification. Data presented as mean ± s.d. *$P < 0.05$. Scale = 50-μm.

4.2.5. Effects of MP-Seeded Peptide Hydrogels on Inflammation and Astrogliosis Post-Surgery

Having demonstrated that magnetically aligned cell-seeded scaffolds facilitated host-axon infiltration and alignment, we interrogated whether the presence of MPs exacerbated inflammation and scarring. ED-1, a marker for microglia/macrophage was probed to access the inflammation in response to the injected scaffolds. ED-1 fluorescence intensities were used to track the immune profile within each experimental group, given that previous studies have quantified ED-1 by normalizing pixel intensity within the injury lesion. The histological section indicated the presence of microglia/microphage throughout the injury site (Fig. 15A). However, ED-1 intensities were significantly reduced in animals receiving cell-seeded scaffolds (Fig. 15C). This result revealed that hMSC-seeded scaffolds reduce inflammation, consistent with previous results that cell-seeded injectable hydrogels attenuate inflammation [60]. Moreover, glial fibrillary acidic protein (GFAP), a marker for activated astrocytes was used to examine the glial scar formation at the site of injection. As Figure 15B displayed, GFAP area was consistent throughout all experimental groups, given previous studies quantified astrogliosis based on GFAP staining [122], [137]. Quantification of GFAP revealed no statistical differences amongst all conditions (Fig. 15D), indicating that hMSC-seeded magnetic injectables did not induce an increase in glial scar formation. Taken together, these results demonstrate that hMSC-seeded aligned peptide scaffolds have beneficial effects on inflammation and do not contribute to reactive gliosis.

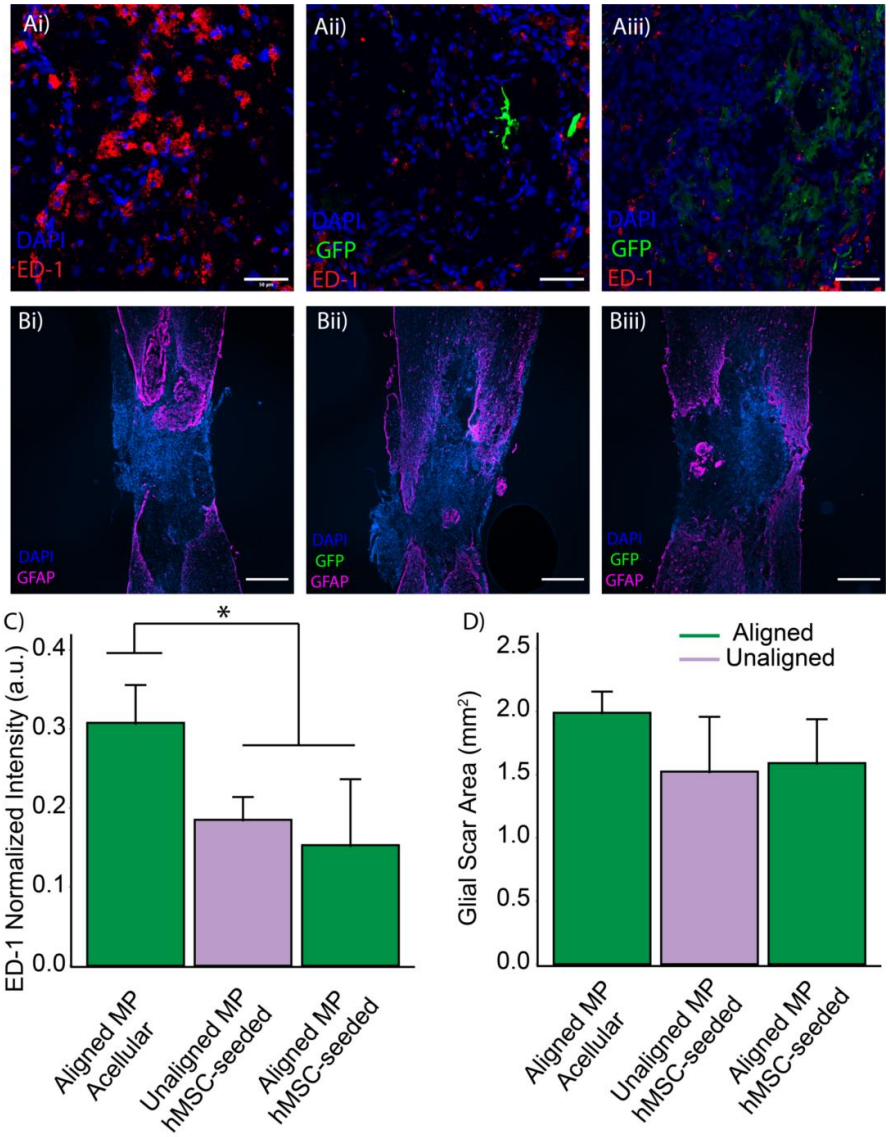

Figure 15. Quantification of inflammation and astrogliosis following injection. (A) Microglia stained with ED-1 within (Ai) aligned acellular, (Aii) unaligned hMSC-seeded and (Aiii) aligned hMSC-seeded hydrogels. (B) Reactive gliosis in response to peptide containing MP scaffolds in (Bi) aligned acellular, (Bii) unaligned hMSC-seeded and (Biii) aligned hMSC-seeded scaffolds. DAPI (blue), GFP (green), ED-1 (red), and GFAP (magenta). (C) Intensity of ED-1 within the scaffolds. (D) Injury area quantification. Data presented as mean ± s.d. $*P < 0.05$. (A) Scale = 50 μm. (B) Scale = 500 μm.

4.3. Dynamic Tuning of Protein Hydrogel Mechanics with Carbonyl Iron Microparticles Guides Three-Dimensional Cell Mechanotransduction

4.3.1. Magnetorheology of Collagen and Fibrin Hydrogels Seeded with Magnetic Particles

Initial experiments were used to quantify the effect of magnetic fields on the viscoelastic properties of collagen and fibrin hydrogels seeded with carbonyl iron MPs. Magnetic fields of increasing strengths were transiently applied to the hydrogels following polymerization within a cone-plate rheometer fitted with a coil to apply an axial magnetic field to the hydrogel (Fig. 16A). To demonstrate the dynamic nature of this effect, 5 mg/mL collagen hydrogels were seeded with different concentrations of magnetic particles exposed to three increasing magnitudes of magnetic field for a duration of 20 seconds, with approximately 2 minutes in between application of the fields of 500-Oe, 2,000-Oe, and 4,000-Oe (Fig. 16B). The storage and loss moduli are plotted as a function of time in Figure 16C-D. The largest increase in storage and loss modulus was observed in collagen hydrogels containing 10 wt% MPs and exposed to a 4,000-Oe magnetic field (Figures 16Ci,Di). The increase in storage modulus appeared to be proportional to the strength of the field for the range of conditions tested. Moreover, for all conditions, removing the magnetic field reversed the increase in viscoelastic properties, which is consistent with previous results [79]. Decreasing the concentration of magnetic particles reduced the effects of the magnetic field, although the increase remained proportional to the field strength.

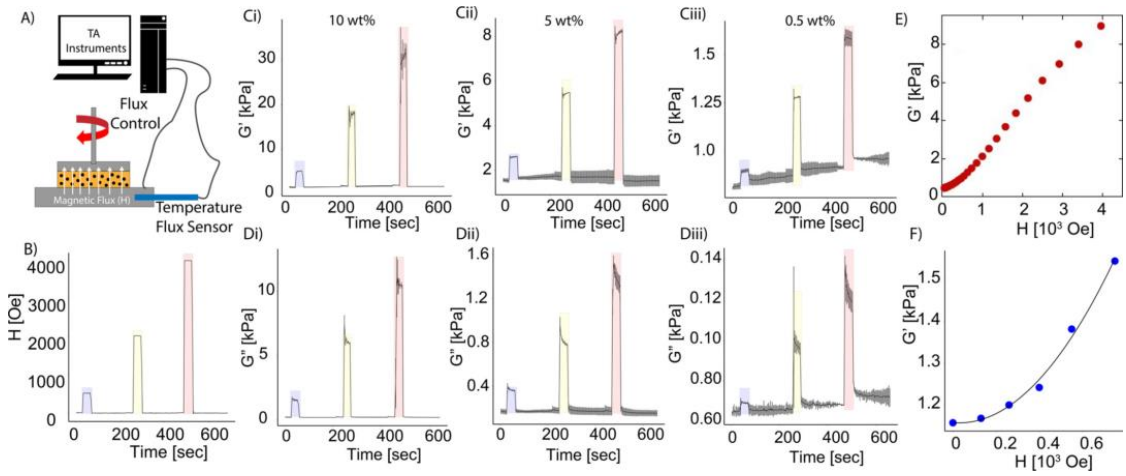

Figure 16. Magnetorheological characterization of common hydrogels and model validation. (A) Magnetorheology test setup with axial application of the magnetic field to hydrogels within a cone and plate geometry. (B) Variation of the magnetic field controlled by the magnetorheometer. Collagen hydrogel storage moduli with (Ci) 10, (Cii) 5, and (Ciii) 0.5 wt % MPs. Loss moduli of (Di) 10, (Dii) 5, and (Diii) 0.5 wt % MPs. Data presented as mean ± s.d. (n = 3). (E) Dependence of 1 mg/mL fibrin storage modulus on magnetic field strength. (F) Measurement of the PDMS storage modulus, embedded with 10 wt % MPs, as a function of the magnetic field (blue circles) and prediction of the analytical model (line).

Next, the magnetic field was applied in the transverse direction to determine whether the direction of the field could alter the rheological measurements. Similar to the rheological tests on a magnetorheometer, a magnetic field of 500-Oe was transiently applied to 5-mg/mL collagen hydrogels seeded with 5 wt% and 10 wt% of MPs for a period of 20 seconds. The data demonstrated that the storage and loss modulus resulted in similar magnitudes as the measurements in the magnetrorheometer, which applied a field in the axial direction (Fig. 17). Increasing the magnitude of the magnetic field also resulted in an

increase in the storage modulus of a 1 mg/mL fibrin hydrogel, as shown in Figure 16E, demonstrating the broad applicability of this approach. Overall, these results verify that previous observations of magnetoviscoelasticity in MR-composite gels [143], [144] can be extended to protein-based hydrogels containing MPs.

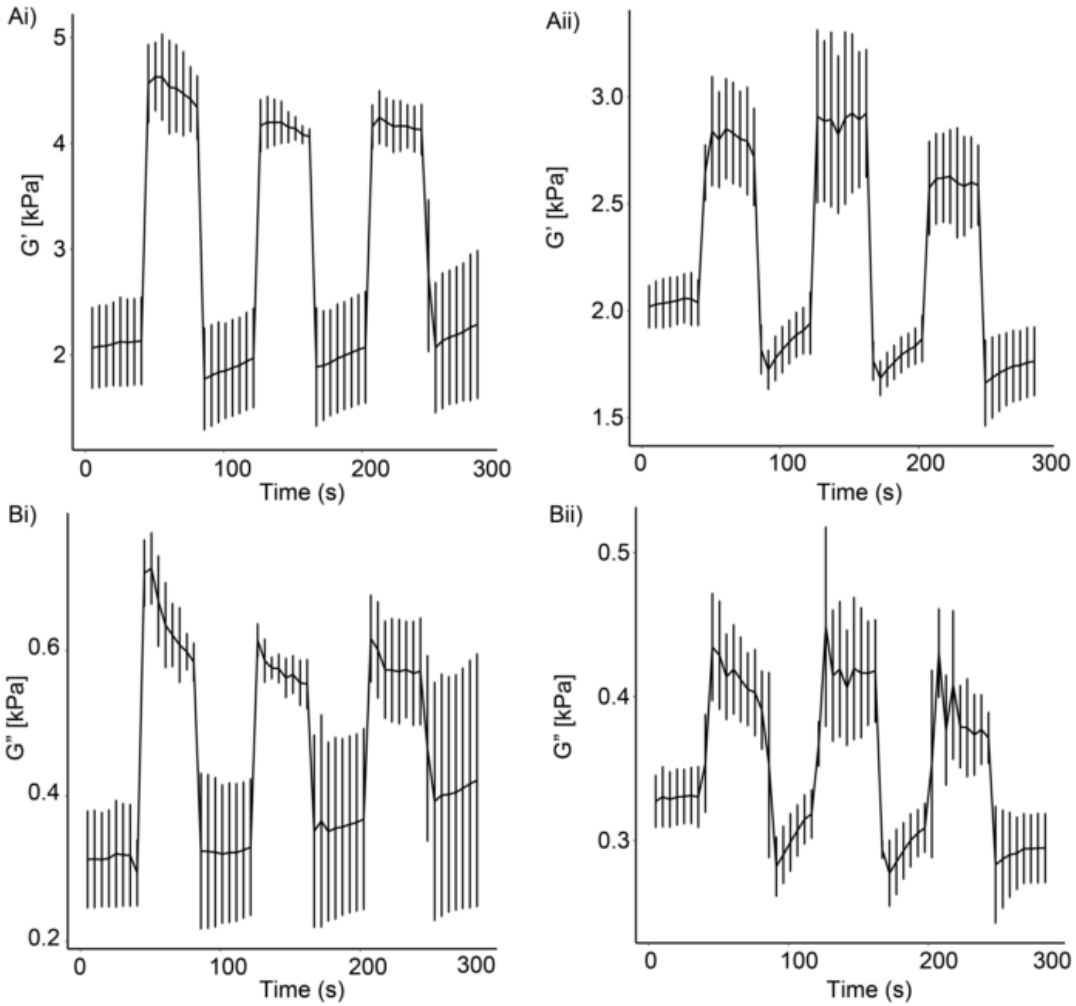

Figure 17. Rheology data for 5 mg/mL collagen embedded with 5 wt% of MPs with a field of 500-Oe in the transverse direction. (A) Storage modulus and (B) loss modulus. Data presented as mean ± std (n = 3).

4.3.2. Analytical Model of Magnetic-Induced Changes to Hydrogel Mechanics

An analytical model was used to provide a mechanistic basis to the rheological measurements, and MPs were seeded within a polydimethylsiloxane (PDMS) elastomer to validate the model. PDMS was chosen to test the theoretical model because, unlike collagen or fibrin, it is a nearly ideal linear, incompressible elastomer with a constant Poisson's ratio, affine deformation, and a very small mesh size that ensures no rotation or slippage of MPs when the field is applied or the sample is sheared. In the presence of a magnetic field, shear deformation of the gel causes the ferromagnetic MPs in the elastomer to become misaligned with the imposed field causing volume-distributed torques. The magnetic permeability of the gel becomes a function of the deformation tensor [145], u_{ik}. In Einstein summation notation:

$$\mu_{ik} = \mu^0 \delta_{ik} + a_1 u_{ik} + a_2 u_{ll} \delta_{ik} \tag{1}$$

where μ^0 is the relative permeability of the undeformed gel, δ_{ik} is the Kronecker delta, and a_1 and a_2 are constants. Since the hydrogels are incompressible, $u_{ll} = 0$, and the last term can be omitted. The magnetic anti-symmetric stress, as in magnetic liquids, is

$$\sigma_{ik} = \frac{1}{2} \epsilon_{ikl} [\boldsymbol{M} \times \boldsymbol{H_0}]_l \tag{2}$$

where ϵ_{ikl} is the Levi-Civita symbol, $\boldsymbol{M}$ is the magnetization, and $\boldsymbol{H_0}$ is the external magnetic field. Taking the z-direction to be the axial direction of the rheometer plate, the shear stress is then

$$\sigma_{xz} = \frac{1}{2} M_x H_z \tag{3}$$

The deformation tensor for oscillatory rheometry can be modeled assuming linear shear

$$u_{xz} = \frac{1}{2} \frac{\partial u_x}{\partial z} \tag{4}$$

The x-component of magnetization can be written as follows:

$$M_x = \frac{\mu_{xz}}{4\pi} H_z \tag{5}$$

where μ_{xz} is the xz component of the magnetic permeability, and H_z is the z component of the internal magnetic field within the hydrogel taking the demagnetization into consideration. Writing μ_{xz} in terms of equation (1), and accounting for linear strain in (4) yields:

$$\mu_{xz} = a_1 u_{xz} = a_1 \left(\frac{1}{2}\frac{\partial u_x}{\partial z}\right) \tag{6}$$

In the case of an incompressible gel, $H_z = \frac{H_0}{\mu^0}$, so the shear stress can be written as:

$$\sigma_{xz} = \frac{1}{16\pi} a_1 \left(\frac{H_0}{\mu^0}\right)^2 \frac{\partial u_x}{\partial z} \tag{7}$$

using the value of a_1 from a previous experiment[146] and noting $\sigma_{xz} = G' \frac{\partial u_x}{\partial z}$, the shear modulus as a quadratic function of the external field is as follows:

$$G' = \frac{1}{40\pi} \frac{(\mu^0 - 1)^2}{\mu^0} H_0^2 \tag{8}$$

From eq. 8, a plot of G' vs H was predicted to be quadratic in H, and the quantity μ^0 could be calculated from the fitting parameter. Experimentally, G' should have a finite value in the absence of a field due to the elastic properties of the elastomer in which the ferromagnetic particles are embedded. This value was treated as a constant in the fitting of the data. This theory was tested with 10 wt% MPs distributed homogenously in PDMS. As shown in Figure 1F, the increase in shear modulus was well fit by eq. 8, where $a = \frac{1}{40\pi} \frac{(\mu^0 - 1)^2}{\mu^0}$ = 6.88 x 10^{-3}. From this parameter, the magnetic permeability μ^0 = 2.5 was in reasonable agreement with the value obtained from magnetometry measurements, μ^0_{exp}= 1.1. Although the increasing rates were similar during the application of the magnetic field, the relative stiffening effect of the fibrin and collagen gels was much greater than in PDMS.

Moreover, the increases in G' of fibrin and collagen were closer to linear than to quadratic in H. The reason for discrepancy with the theory is unknown but could be due to larger mesh sizes in these hydrogels compared to PDMS, the highly non-affine deformation of these networks in shear, or the non-linear elastic response of these fiber networks. Nevertheless, this model provides a mechanistic basis of the observed rheological results, and implies that the change in stiffness results from the intrinsic properties of the iron particles and not from an internal stress that they apply to the network in which they are embedded.

4.3.3. The Effect of Magnetic Fields on Magnetic Particle Displacement Within Hydrogels

A key assumption of the analytical model is that the magnetic particles are constrained within the network. In order to evaluate this assumption, fluorescently-labeled MPs were seeded within collagen hydrogels and observed by a resonance laser scanning confocal microscopy. Labeled MPs were tracked over a period of 20 seconds during the application of a magnetic field in collagen hydrogels of two different concentrations (2 and 5 mg/mL). In contrast to the rheology conducted in Figure 16, the magnetic field was applied perpendicular to the z-axis using permanent, neodymium magnets (the direction of the field is shown in Figure 18) to allow higher resolution detection of small displacements. In order to assess the effect of fiber formation within the hydrogels, the MPs were tracked before and after polymerization. As Figure 18A-B indicates, a 2,500 Oe magnetic field caused measurable displacement of the MPs only before polymerization of the 2 mg/mL collagen gel. Once the hydrogel solidified, the magnetic field did not induce any measurable displacement of the particles. Figure 18C-D demonstrates a similar effect in the higher concentration collagen gel. Again, the magnetic field did not cause any measurable displacement in the polymerized hydrogel. The distribution of MP displacement over the 20-second period is graphed in Figure 18E-F for the 2 and 5-mg/mL hydrogels. Figure 18G shows that the collagen concentration had no significant effect on the total displacement of the MPs prior to polymerization. These findings indicate that the application of a magnetic field did not cause substantial displacement of the MPs in the polymerized collagen hydrogels even at the lowest concentration of collagen, indicating

that the change in viscoelastic properties observed during magnetorheology was not caused by prestress on the fibrous network.

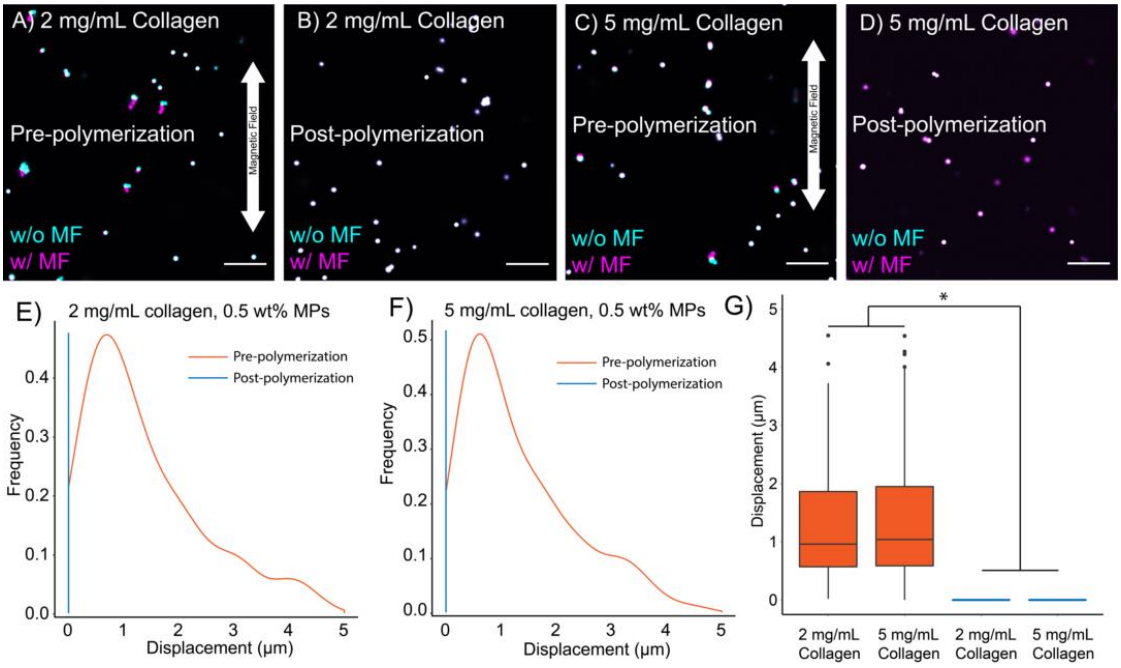

Figure 18. Displacement of magnetic particles within 2 mg/mL and 5 mg/mL collagen hydrogels. Confocal images of 0.5 wt% magnetic particles in 2 mg/mL collagen hydrogels (A) prior to polymerization and (B) post polymerization (20-seconds between images) (n = 115). Fluorescent images of 0.5 wt% magnetic particles in 5 mg/mL collagen hydrogels (C) prior to polymerization and (D) post polymerization, (n = 115). Cyan = without magnetic field, magenta = with magnetic field of 2,500-Oe. Scale = 50-µm. (E,F) Quantification of MP displacement in response to a magnetic field in 2 mg/mL and 5 mg/mL collagen hydrogels. (G) Box plots of MP displacement. *$p < 0.05$.

4.3.4. Tracking Magnetic Particle Displacement Within Hydrogels Under Shear Stress

In order to determine the effect of magnetic fields on the displacement of MPs in the presence of externally applied stress, a constant shear stress was applied by a flat plate rheometer fitted with a fluorescence microscope [147], so that MP displacement could be tracked during the initial application of stress and subsequent creep in the hydrogel (Fig. 19A-B). These measurements were conducted at regions located at the same radial distance from the rotational axis for consistency. In order to demonstrate the broad applicability of this effect, these experiments used 1-mg/mL fibrin hydrogels containing 1 wt% fluorescently-labeled MPs. Figures 19C-E indicate the distribution of MP displacement with and without the presence of a 1,000-Oe field immediately following the application of 10, 25, and 50-Pa. These findings are consistent with previous studies that found a distribution of local strain within a fibrous network exposed to global strain [148]. For each magnitude of stress, the instantaneous MP displacement was substantially reduced in the presence of a magnetic field. The disparity was most apparent at the lowest level of applied stress (10 Pa). Not only did the magnetic field reduce the instantaneous displacement, but it also reduced the spread of the distribution, attenuating non-affine motion. To quantify this effect, the widths of the distributions at their half-heights were averaged across the three levels of stress and compared between magnetic and non-magnetic conditions (Figure 19F). The magnetic field also affected the creep behavior of the fibrin hydrogels. The creep rate was measured with two metrics: the deformation rate of the MPs as well as the creep angle recorded by the rheometer. Figure 19G shows that the magnetic field significantly decreased the deformation rate of the MPs at a stress of 50 Pa. These results are consistent with the creep rate measured by the rheometer plate for stress levels of 25 and 50 Pa plotted

in Figure 19H. Overall, these results indicate that the magnetic field restricted the displacement of the MPs within hydrogels exposed to the external mechanical stimulus of shear stress, suggesting that the presence of the field reduces relative motion between MPs.

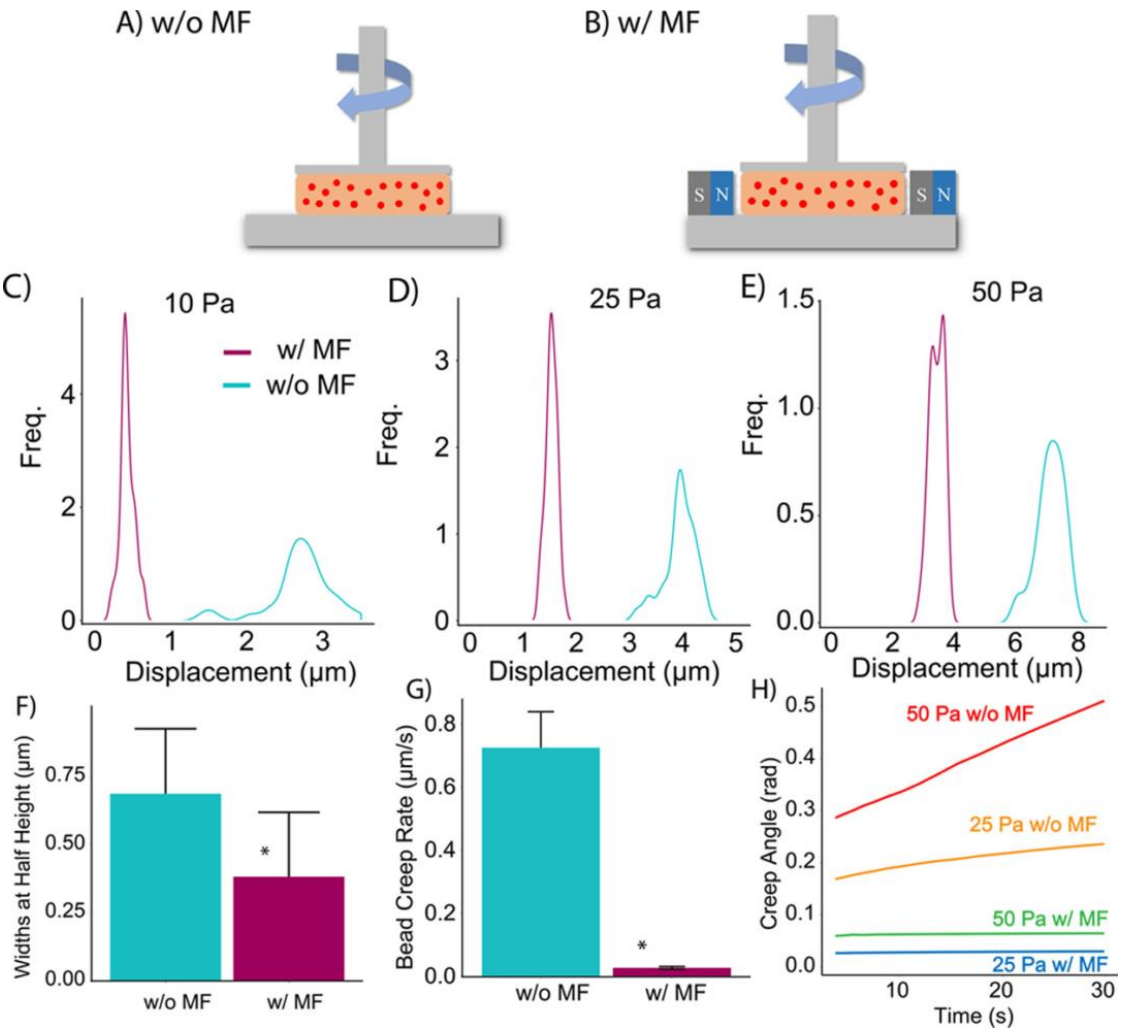

Figure 19. Schematic of the rheometer setup of magnetically responsive fibrin hydrogels (A) without and (B) with a magnetic field (MF). Quantification of instantaneous MP displacement undergoing (C) 10, (D) 25, and (E) 50 Pa shear stresses with and without a 1000 Oe magnetic field (n = 35 per condition). (F) Average width of the instantaneous displacement distribution. (G) Creep rate measured by tracking MP displacement in fibrin gels exposed to 50 Pa shear stress over 30 s (n = 3). (H) Creep angle measured from the rheometer. These fibrin hydrogels contained 1 wt % MPs. *$p < 0.05$.

4.3.5. Cell-Mediated Magnetic Particle Displacement

Although rheological experiments revealed the effect of magnetic fields on MP displacement within a globally deformed fibrous network, this approach could not elucidate the effect of magnetic fields on local deformation of MPs entrapped within the fibers. Therefore, live cell experiments were conducted by seeding 1×10^6 cells/mL human coronary artery smooth muscle cells (hCASMCs) into 5 mg/mL collagen and 1 mg/mL hyaluronan composite hydrogels containing 0.5 wt% MPs. The concentration of MP was chosen to visualize particle displacement in brightfield microscopy. A schematic of the microfabricated device containing the hydrogel is shown in Figure 20A. Additionally, a scanning electron microscopy image of the hydrogel containing 0.1 wt% MPs is shown in Figure 20B.

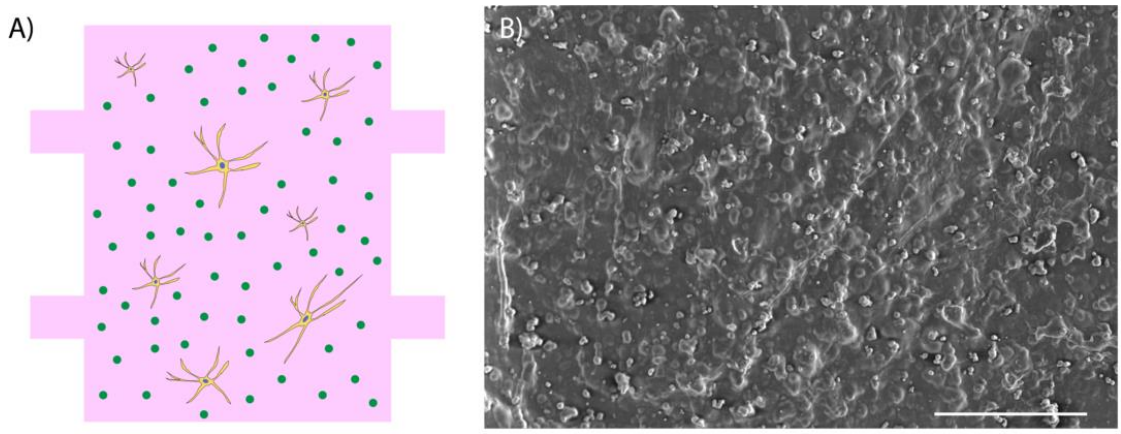

Figure 20. Physical properties of collagen-MP hydrogels. (A) Schematic of microfabricated chamber. (B) SEM image of collagen fibers containing MPs. Scale = 100 µm.

Figure 21A provides a schematic of the cell-seeded hydrogels polymerized within a microfabricated device, and Figure 21B shows how the magnetic field was applied to the hydrogel while on the stage of an epifluorescence microscope using neodymium magnets. The magnets were positioned to apply a uniform field of 500 Oe to the cell-seeded hydrogels. This combination of magnetic field strength and MP density was chosen to increase hydrogel storage modulus without affecting the contractility of the smooth muscle cells: rheological results indicated that the application of a 500-Oe field to collagen hydrogels seeded with 0.5 wt% MPs increased the storage modulus by a modest amount (from 500 Pa to approximately 650 Pa).

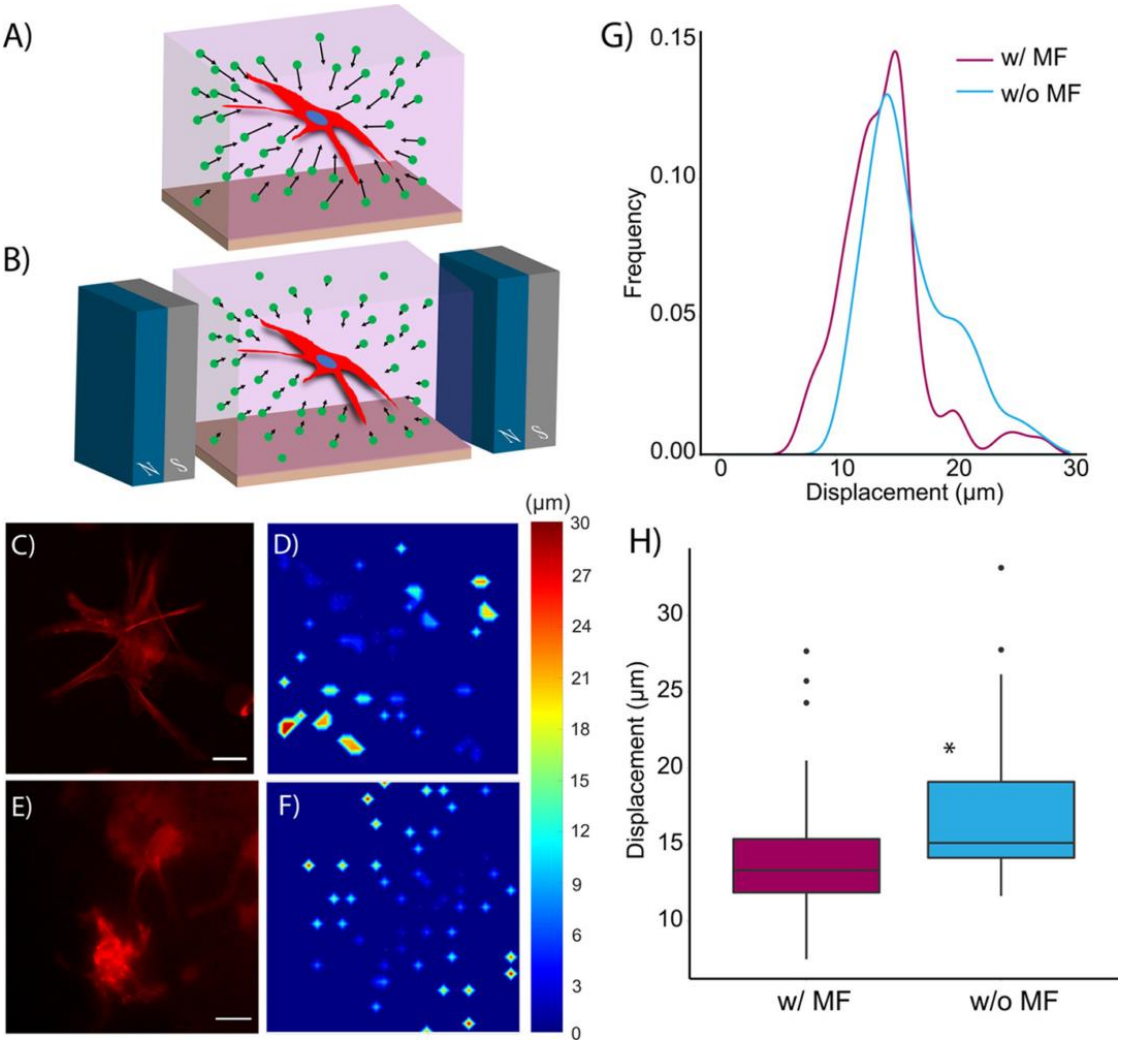

Figure 21. Schematic of 3D hydrogels used for live cell microscopy (A) without and (B) with a 500 Oe magnetic field (MF). RFP-LifeACT-labeled hCASMC in 5 mg/mL collagen, 1 mg/mL HA, and 0.5 wt % MPs (C) without a magnetic field and (D) corresponding heat map of MP displacement. (E) Cells and (F) heat map with a magnetic field. Quantification of MP displacement due to cell motility with (G) 0 (w/o MF) and 500 Oe (w/ MF) (n = 75 MPs per condition). Box-and-whisker plots of (H) MP displacement. Scale = 25-μm. *$p < 0.05$.

We found no significant difference between cell morphology and alpha-smooth muscle cell actin expression in the hCASMCs between this range of storage moduli (Fig. 22), suggesting similar levels of cell contractility in both conditions. Figure 21C shows a representative cell at 6-hrs post gel polymerization in the absence of a magnetic field. The displacement of the MPs in that time was quantified and displayed in the form of a heat map in Figure 21D. Both the cell and the displacement of adjacent MPs in the presence of a 500-Oe magnetic field are presented in Figure 21E. As the heat map indicates, the displacement of the MPs was substantially reduced in the presence of the magnetic field (Fig. 21F). Quantification of total MP displacement distributions verified that application of the magnetic field reduced MP displacement (Fig. 21G). Box plots provided in Figure 3H indicate a significant difference in MP displacement. These results are consistent with the rheological findings: the MPs are constrained from moving relative to one another in the presence of a magnetic field. Since the MPs are effectively trapped within the fibrous network, the magnetic field then increases the storage modulus of the hydrogel. This increase in stiffness was apparent in both global deformation (Figure 19) and local, cell-mediated matrix deformation (Figure 21).

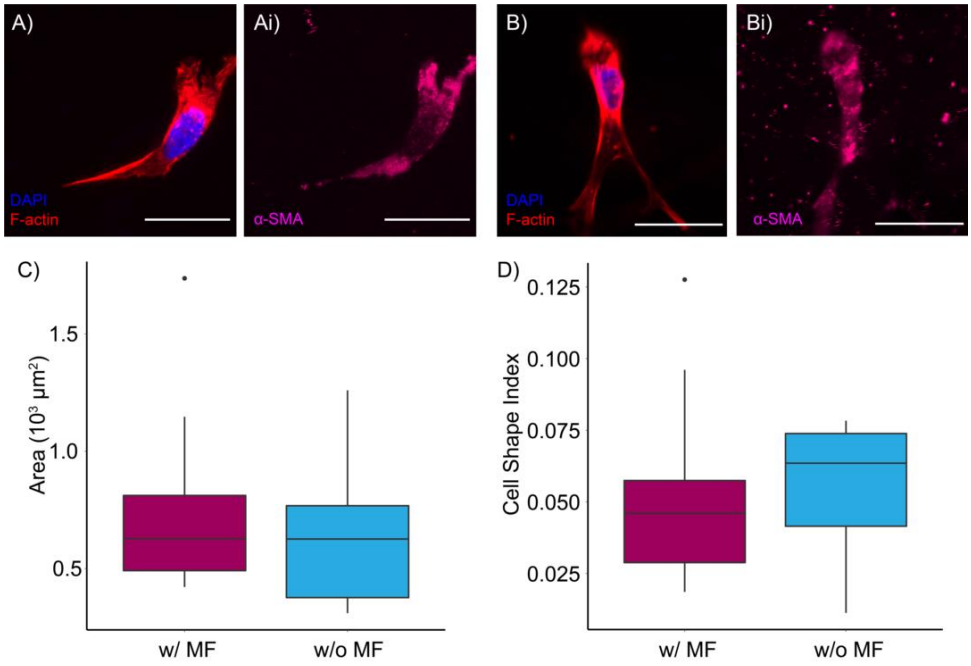

Figure 22. Live-cell morphological studies. Representative images of RFP-LifeACT-labeled HCASMC (A) with and (B) without magnetic field. Quantification of (C) cell area and (D) cell shape index. Scale bar = 25 µm.

4.3.6. Alteration of ECM Mechanics Instantaneously Affects Calcium Transients

In order to highlight the ability of MR hydrogels to instantaneously change 3D substrate mechanics to an extent that alters the cell response, calcium transients were measured in smooth muscle cells seeded inside collagen hydrogels with and without MPs. 1×10^6 HCASMC/mL were seeded into 2-mg/mL collagen hydrogels without magnetic particles as negative controls. The same cell density was seeded into 2 mg/mL collagen hydrogels containing 2.5 wt% of MPs to observe the dynamic effects of calcium transients. Application of a magnetic flux of 2850-Oe increased the storage modulus from approximately 100-Pa to 650-Pa (Fig. 23), yielding a substantial increase in the stiffness of the hydrogel and providing an opportunity to interrogate how this change in stiffness altered calcium signaling**.**

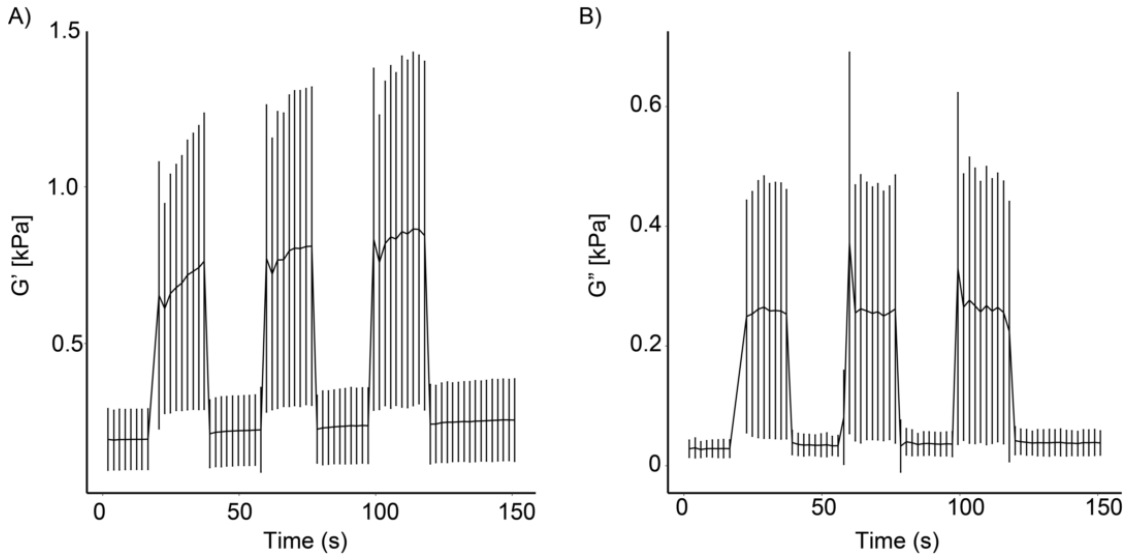

Figure 23. Rheology data for 2 mg/mL collagen embedded with 2.5 wt% of MPs at 5,000-Oe. (A) Storage modulus and (B) loss modulus. Data presented as mean ± std (n = 3).

Spontaneous calcium transients were observed to occur at a frequency of approximately one cycle per three minutes in both MR and non-MP-seeded collagen hydrogels, so the magnetic field was applied for three minutes (increased storage modulus), removed for the next three minutes (decrease storage modulus), and subsequently reapplied for three minutes (re-increase storage modulus).This "on-off-on" provided a means to directly evaluate how the increase in stiffness affected calcium signaling in the hCASMC (Fig. 24A). Figure 24B provides an image of Fluo-4-labeled hCASMC in hydrogels without any magnetic particles as a negative control, whereas Figure 24C shows an image of hCASMC in MP-seeded collagen hydrogels. Averaged calcium transients indicate no

significant difference in cells when the field is applied compared to no magnetic field (Fig. 24D). Quantification of the rate of calcium influx also indicated no significant effect caused by the magnetic field in the absence of MPs as a function of time (Fig. 24E) and averaged over all measured transients with and without the field (Fig. 24F). The magnetic field also did not appear to alter the frequency of spontaneous calcium transients in the cells embedded in the non-MP-seeded collagen gels. Figure 24G shows that the application of a magnetic field significantly altered the dynamics of calcium transients of hCASMC in MR-hydrogels. The period of the transient was significantly shorter and the rate of initial influx was significantly higher. Quantification of the slope of the transient indicated that the SMCs increased their rate of calcium influx in response to the higher storage modulus yielded by the application of a magnetic field, but there was no difference between the slope of the transient between the first and last three minutes (Fig. 24H). Two-sample t-tests between the "on" and "off" condition revealed a significant difference in the slope of the transient in MR hydrogels (Fig. 24I). These measurements can be compared to previous studies using smooth muscle cells [149] and cardiomyocytes on 2D substrates with tunable stiffness[150] and myofibroblasts in collagen gels of differing concentrations [151], though these experiments were performed under conditions where the time scale for the response to dynamic changes to stiffness could not be measured. In contrast, the results in Figure 4 are measured after dynamically and reversibly altering stiffness on a second time scale without any alteration to the pore size of the collagen fibrous matrix. Taken together, these findings provide new insight into the effect of ECM stiffness on calcium handling in cells in 3D, and pave the way for future mechanotransduction experiments to interrogate the mechanisms by which cells respond to dynamically altered ECM mechanics.

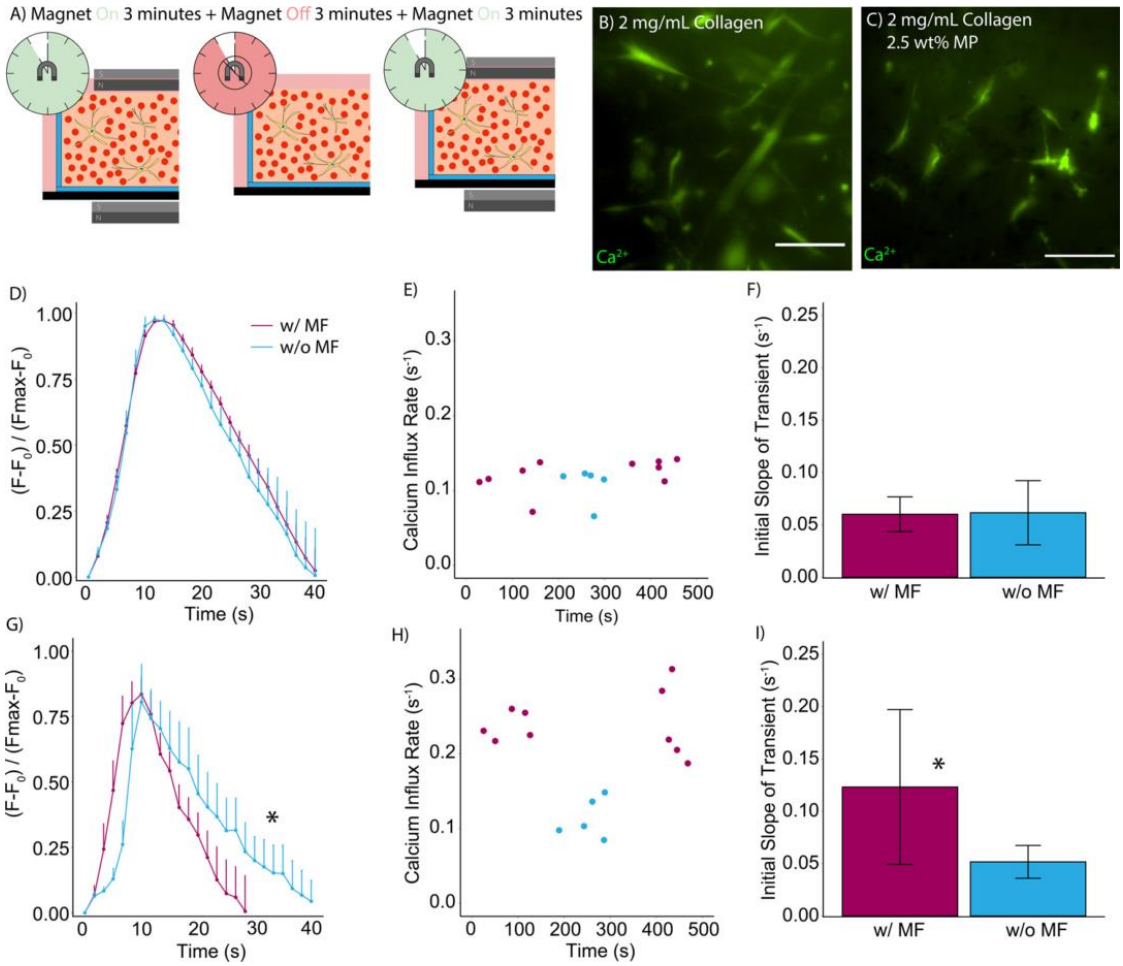

Figure 24. Effects of dynamically altered hydrogel mechanics on cellular calcium transients. (A) Schematic of the "on–off–on" regimen for both non-MP-seeded and MP collagen hydrogels. Fluorescence image of Fluo-4 as Ca2+ reporter in (B) 2 mg/mL collagen and (C) 2 mg/mL collagen and 2.5 wt % MP hydrogels. (D) Average calcium transients in non-MP-seeded collagen hydrogels with field on (w/ MF) and off (w/o MF). (E) Slope of calcium transients and (F) initial slope of calcium transients in non-MP-seeded collagen hydrogels. (G) Average calcium transients in MP-seeded hydrogels with field on (w/ MF) and off (w/o MF). (H) Slope of calcium transients and (I) initial slope of calcium transients in MP-seeded collagen hydrogels. Scale = 100 μm. *P < 0.01. (n = 5 cells per condition, 10 transients for MF on and 5 transients for MF off per condition).

4.3.7. Cell Morphology in Response to Hydrogel Stiffness in 3D

Having demonstrated the short-term, immediate cell response to changing substrate mechanics, experiments were then conducted to assess long-term changes in cell behavior. For these experiments, normal human astrocytes (NHA) were used to demonstrate the flexibility of the approach. Cells were seeded at a density of 1×10^6 cells/mL into 5 mg/mL collagen hydrogels containing 5 wt% of MPs. Rheological testing indicated that a magnetic field of 7,700 Oe increased the hydrogel stiffness from 0.8 kPa to 8.5 kPa (Fig. 25), which represented a sufficient increase to describe the changes in cell morphology.

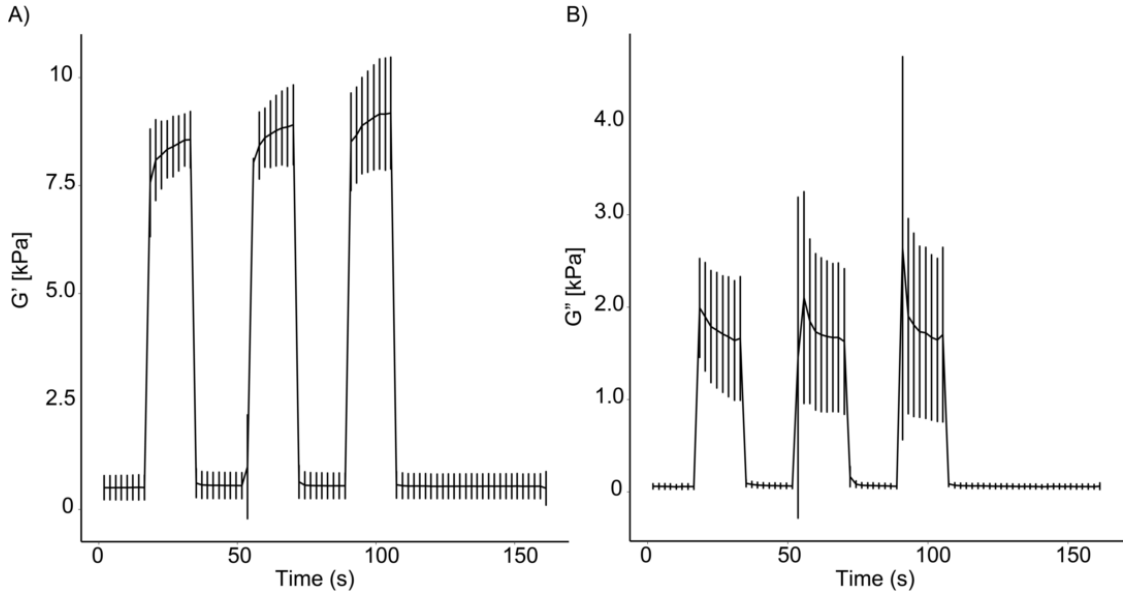

Figure 25. Rheology data for 5 mg/mL collagen embedded with 5 wt% of MPs at 7,700-Oe. (A) Storage modulus and (B) loss modulus. Data presented as mean ± std (n = 3).

Furthermore, 5 wt% MPs was chosen due to the high viability of cells seeded in hydrogels containing that concentration of MPs (Fig. 26). Three conditions were tested: a magnetic field applied to the cell-seeded hydrogel in the absence of MPs (Fig. 27A), cell-seeded hydrogels containing MPs in the absence of a magnetic field (Fig. 27B), and cell-seeded hydrogels containing MPs and exposed to the 7,700-Oe magnetic field (Fig. 27C). Cell morphology was measured at 11 and 22 hours by fixing the cells and staining with DAPI and phalloidin.

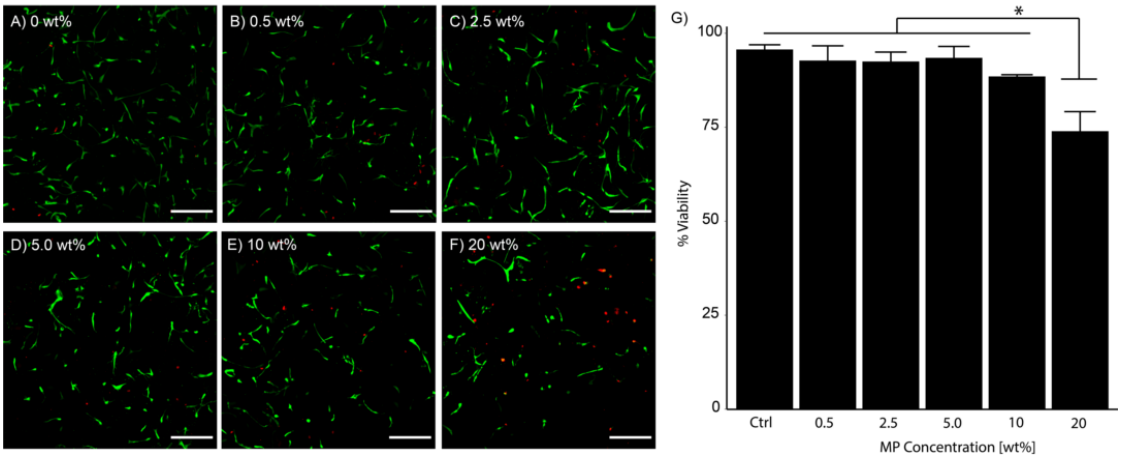

Figure 26. Examination of cell viability in 5 mg/mL collagen with various MP concentrations. Representative images of Live/Dead stains in (A) 0 wt%, (B) 0.5 wt%, (C) 2.5 wt%, (D) 5 wt%, (E) 10 wt%, and (F) 20 wt%. (G) Quantification of cell viability. Scale = 250-µm.

At 11 hours, the spread area of the cells in hydrogels containing the MPs and exposed to the magnetic field was significantly reduced, and the cell shape index was significantly increased compared to the other conditions (Fig. 27D,E). Moreover, the cells in MP-seeded hydrogels exposed to the magnetic field continued to exhibit reduced spread area and increased cell shape index (Fig. 27F-I). These findings are consistent with previous studies in 3D hydrogels showing that one phase, non-degradable hydrogels with high stiffness reduce cell spreading due to the inability of cells to elastically deform/mechanically remodel the ECM in 3D [129], [152]. Although the mechanical properties of these synthetic hydrogels have exhibited a capacity to study mechanotransduction, the photo-active dynamics affect the hydrogel's pore sizes. Previous studies have shown that the stiffening effect in photocrosslinkable hydrogels resulted in a decrease of dextran diffusivity [153], limiting the ability to dynamically tune substrate stiffness without altering porosity. The cells in the hydrogels seeded with MPs and exposed to a magnetic field sense a substantially increased substrate stiffness, even though the hydrogel composition and pore size is unaffected by the presence of MPs and magnetic field.

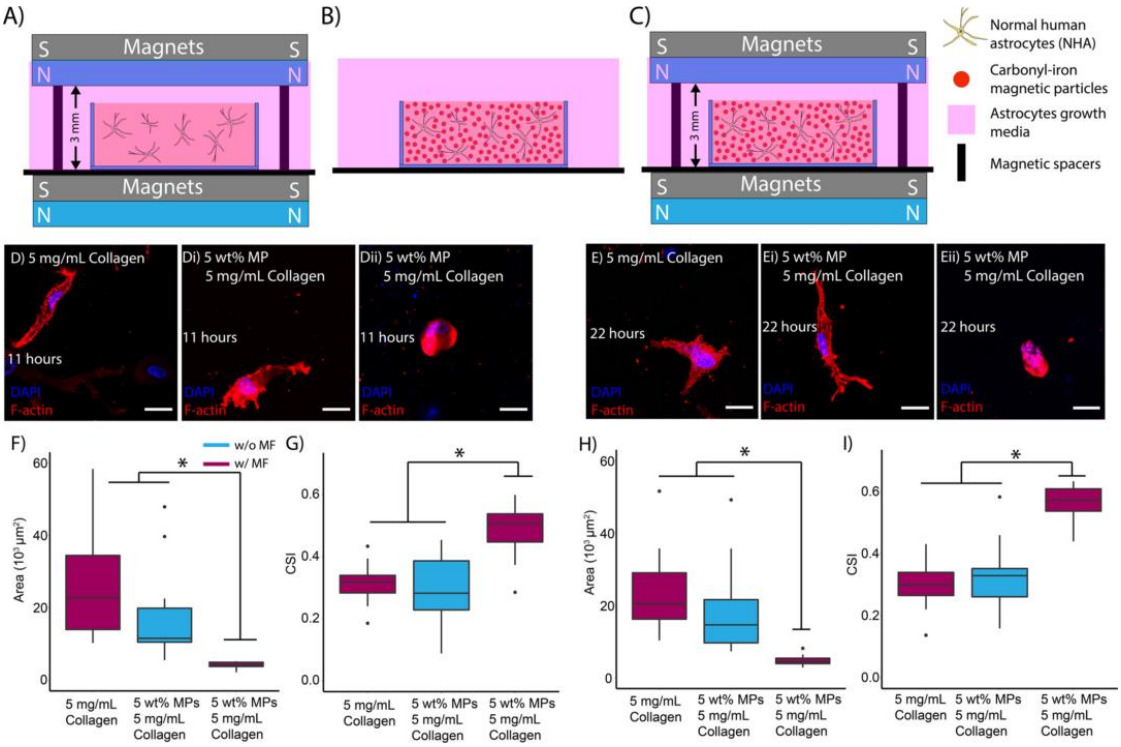

Figure 27. Schematic of cell experiments with (A) 5 mg/mL collagen in the presence of a 7,700 Oe magnetic field, (B) 5 mg/mL collagen and 5 wt % magnetic particles (MPs) without a magnetic field, and (C) 5 mg/mL collagen and 5 wt % magnetic particles (MPs) with a 7,700 Oe field. Representative images of cells (D) for the three conditions at 11 h. Representative images of cells (E) for the three conditions at 22 h. Quantification of (F) cell area and (G) cell shape index (CSI) for the 11 h time point and (H) cell area and (I) cell shape index (CSI) for the 22 hour time point. DAPI (blue) and F-actin (red). Scale = 50 µm. *$P < 0.05$. (n = 15 per condition).

4.3.8. Dynamic Tuning of Hydrogel Mechanics to Control Cell Mechanotransduction

Altering hydrogel mechanics with magnetic fields yields a useful tool to study cell mechanics in 3D environments, but the reversibility of the effect substantially amplifies its impact. These studies interrogated whether tuning hydrogel mechanics with transient application of a magnetic field (Fig. 28A-B) could control mechanosensing by the astrocytes. Three different conditions in MP-seeded hydrogels were evaluated: (i) NHA were allowed to spread in the absence of a magnetic field for a full 22-hr period, ("off-off"), (ii) NHA experienced 11-hrs in the absence of a field and then a magnetic field was applied for the remaining 11-hrs ("off-on"), and (iii) a magnetic field was applied for the first 11-hrs and then removed for the remaining time ("on-off"). Figures 28A-C provide schematics summarizing these conditions. At the end of the 22-hr period, all hydrogels were fixed and stained with DAPI, phalloidin, and an anti-YAP antibody, given previous findings that substrate mechanics affects translocation of the transcription factor to the nucleus [66]. As Figure 28D shows, astrocytes in the "off-off" condition spread and YAP was diffuse throughout the cytoplasm. In contrast, in Figure 28E, the astrocytes in the "off-on" condition exhibited increased YAP staining within the cell nucleus, especially when compared to cells exposed to the "on-off" condition (Fig. 28F). The was no significant difference in both the spread area and cell shape index between the "off-on" and "on-off" conditions, though both were significantly different from the "off-off" control (Fig. 28G,H). Quantification of the YAP staining verified that the "off-on" condition exhibited significantly increased nuclear translocation in Figure 28I. These results suggest that cells in the "off-on" condition initially sense a more compliant ECM and begin to spread, but once the magnetic field is applied the cells sense a stiffer environment and YAP

translocation increases. In contrast, cells in the “on-off” condition are initially constrained from spreading by the increased stiffness, but once the magnetic field is removed the cells sense a softer environment and begin to spread and reduce YAP translocation. These results mirror the findings in other approaches to dynamically tune substrate stiffness with more complex alterations to hydrogel properties [72], [129], [150], [154]. Yet, this approach requires no alteration to hydrogel composition or chemistry to dynamically tune hydrogel mechanics and interrogate cell mechanotransduction.

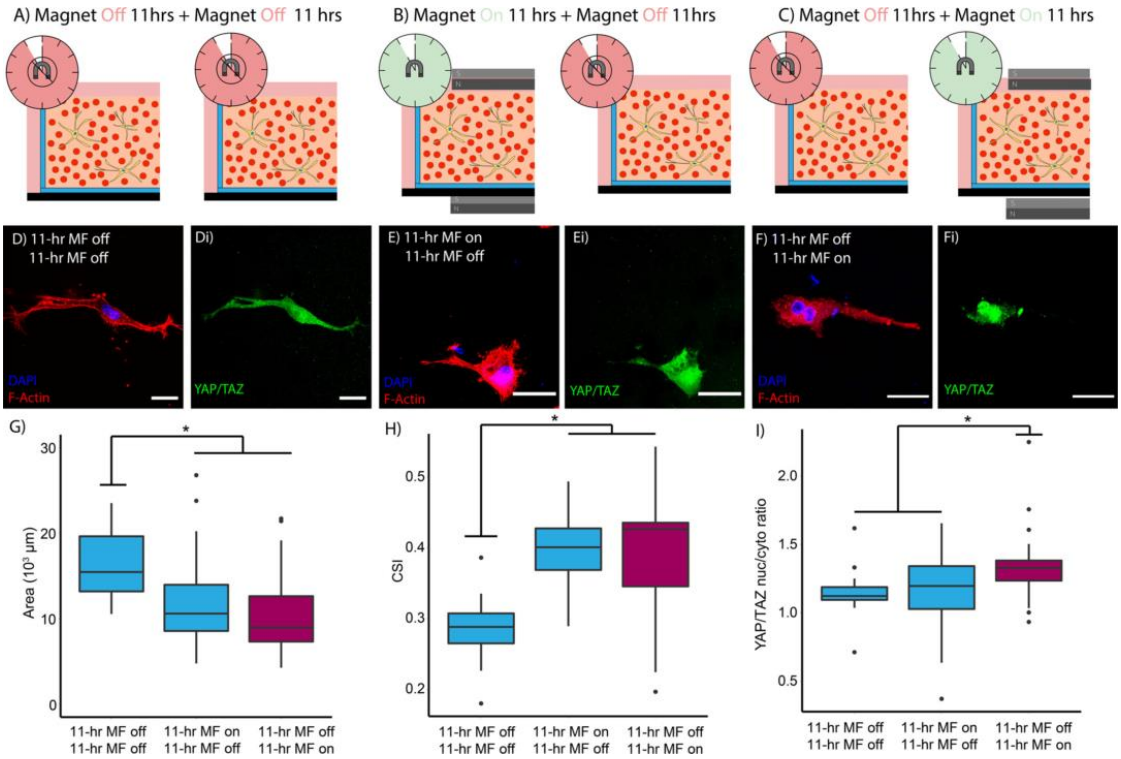

Figure 28. Dynamically tunable hydrogels by transient application of a 7,700 Oe magnetic field to 5 mg/mL collagen. (A–C) Schematics of "off–off", "off–on", and "on–off" regimens. Representative images of cell morphology in (D) "off–off", (E) "on–off", and (F) "off–on" conditions. Immunofluorescence images showing YAP in (Di) "off–off", (Ei) "on–off", and (Fi) "off–on" conditions. Quantification of (G) cell area, (H) cell shape index, and (I) nuclear to cytoplasmic YAP ratio. DAPI (blue), F-actin (red), and YAP (green). Scale = 25 µm. *P < 0.05. (n > 25 cells per condition).

4.4. Matching Mechanical Heterogeneity of the Native Spinal Cord Augments Axon Infiltration in 3D-Printed Scaffolds

4.4.1. Microstructural Characterization of Spinal Cord Mechanical Properties

In order to examine the heterogeneity of spinal cord tissue, initial experiments using AFM and tensiometry were conducted to interrogate differences in gray and white matter along the transverse anatomical plane. Previous experiments have found that the gray matter is stiffer than white matter in all anatomical plans (coronal, sagittal and transverse) [130], though there is also conflicting evidence that no significant different between gray and white matter exists [90]. To rectify the discrepancies between these studies, AFM and tensiometry experiments were performed on the spinal cord (Fig. 29A,B).The tissue was divided into three regions: sacral, thoracic/lumbar, and cervical to assess whether anatomical level affected the mechanical properties of the cord. AFM revealed that the gray matter exhibits significant higher elastic moduli compared to white matter, though there were no statistical differences between the three levels (Fig. 29C). Post-hoc Tukey tests indicated significant differences between gray and white matter at each level. Tensiometry examined the relaxation factors of both gray and white matter by measuring stress relaxation following indentation. Figure 29D shows the relaxation factors for both gray and white matter in all three regions, and two-factor ANOVAs revealed a statistical difference between the gray and white matter, though again there is no difference between levels. Taken together, these results presented here indicate that the gray matter exhibits stiffer and more viscoelastic mechanics compared to white matter, and that there is no difference in the microstructural mechanical properties of gray and white matter along the length of the cord.

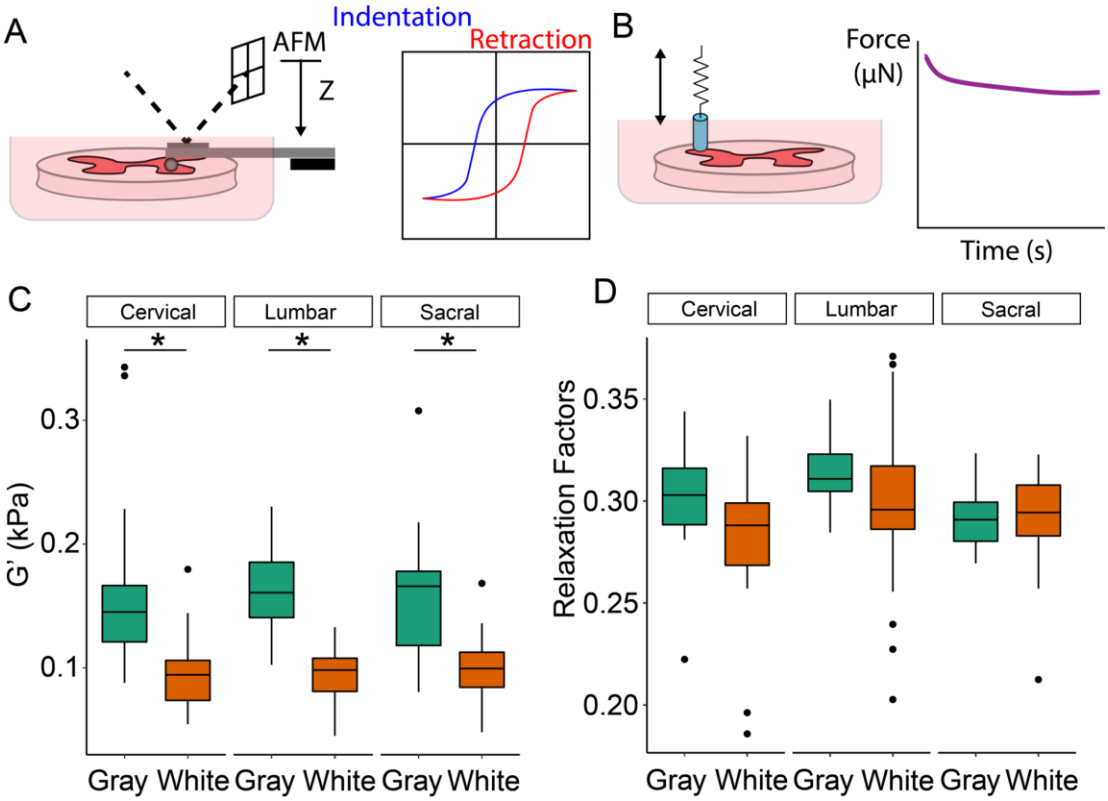

Figure 29. Microstructural mechanical properties of bovine spinal cord tissues. (A,B) Schematic of atomic force microscopy (AFM) and tensiometer. (C) Measurements of gray and white matter using AFM. (D) Relaxation factors of gray and white matter via tensiometer. The box plots depict the median, 25 and 75 percentiles, and the whiskers represent 1.5x the interquartile range. *$p < 0.05$ ($n = 3$).

4.4.2. Macrostructural Mechanical Properties of Spinal Cord Tissue

Rheology was conducted to characterize bulk mechanics of the cord at cervical, lumbar, and sacral levels. Given the results of the AFM testing, these experiments tested the hypothesis that the disparity in bulk mechanical properties of anatomical levels is due to differences in the ratio of gray-to-white matter. Therefore, shear storage and loss moduli as well as cross-sectional area of gray and white matter were measured in 5-6-mm thick transverse spinal cord sections taken from different levels. Figures 30A-C show rheological experiments performed on three different bovine spinal cords. The highest storage and loss moduli were measured in cervical regions of two of the animals and in the sacral region in the third animal.

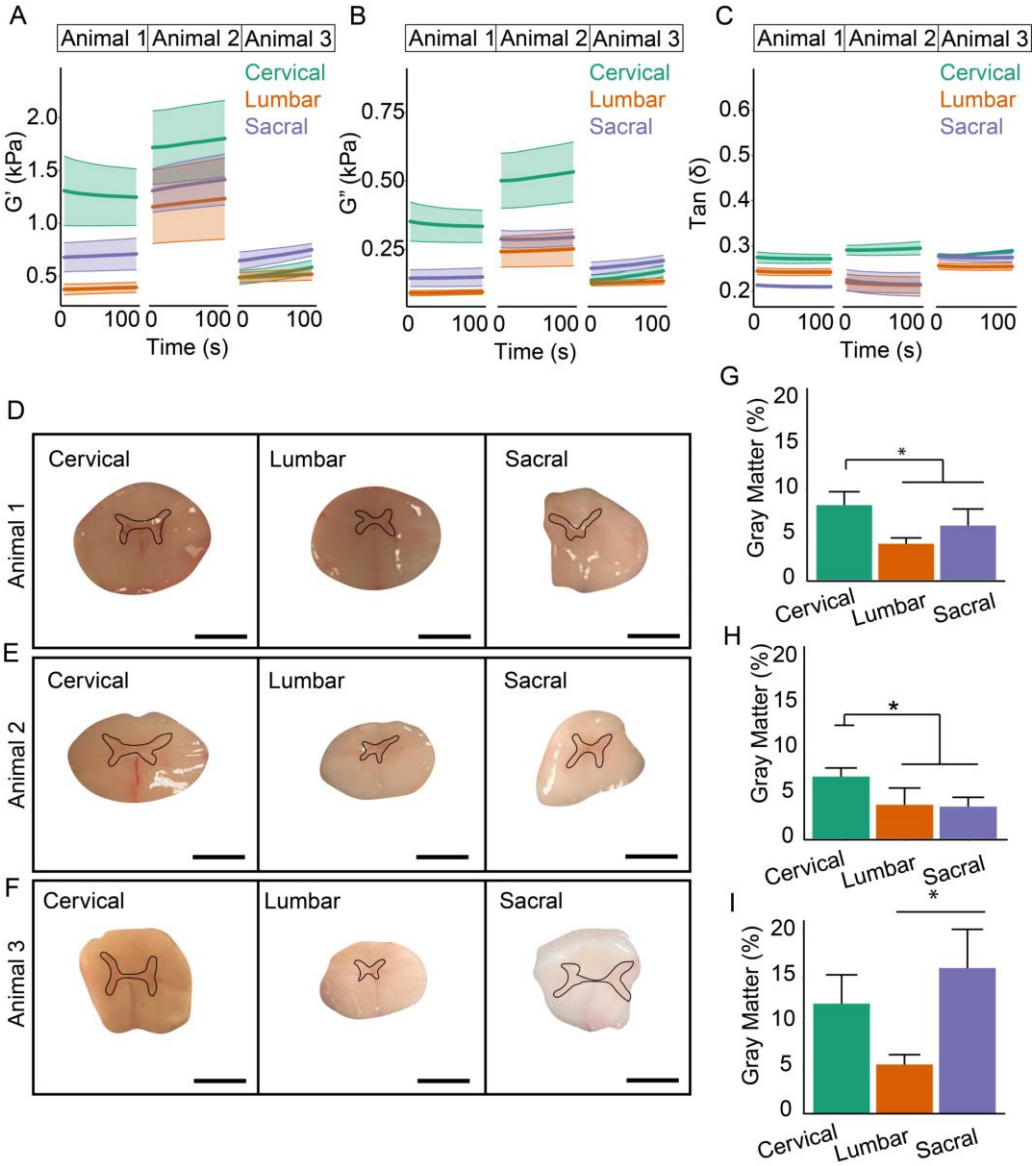

Figure 30. Characterization of macrostructural mechanical properties of bovine spinal cord tissues. Rheological experiments of cervical, lumbar and sacral regions of spinal cords from 3 animals showing (A) storage modulus, (B) loss modulus and (C) tan(δ). Data presented as mean ± s.e.m. (D-F) Images of spinal cords and (G-I) quantification of gray-to-white matter ratios. The black lines indicate the representative regions of quantified gray matter. Data presented as mean ± s.d. *$p < 0.05$ ($n = 3$).

Moreover, Figure 31 displays the sections were tested at increasing magnitudes of compressive strain to determine whether the cord exhibits the compression stiffening observed in other tissues [155], [156]. In order to reconcile the bulk testing with the AFM measurements that found no difference in gray or white matter along the cord, transverse spinal cord sections (Fig. 30D-F) were imaged and the percentage of gray matter in the cross-section was expressed as a percentage of the total area (Fig. 30G-I). The gray matter in the cervical region was significantly higher compared to the lumbar and sacral regions in the experiment from the first two cords, and highest in the sacral region in the third animal. Therefore, these results suggest that differences in the bulk rheological properties along the cord are due to differences in the amount of the stiffer gray matter in the cross-section of the cord.

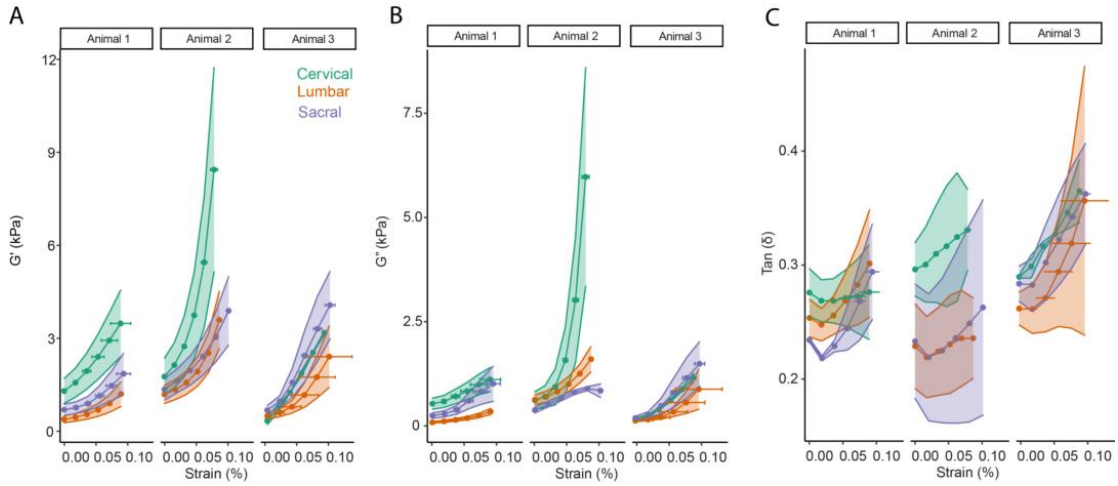

Figure 31. Compression stiffening effects of bovine spinal cord Rheological experiments of cervical, lumbar and sacral regions of spinal cords from 3 animals showing (A) storage modulus, (B) loss modulus and (C) tan(δ). Data presented as mean ± s.d.

4.4.3. Microstructural Analysis of Gray and White Matter

In order to provide insight into structural differences between gray and white matter that give rise to mechanical heterogeneity, immunohistochemistry was performed to examine differences in cell nuclei and myelin expression in both regions. Sections from the beginning and end of the experiment were analyzed to determine whether the cords undergo substantial demyelination over the course of the experiment. Figure 3 shows cervical sections fixed at the beginning (Fig. 32A) and end (Fig. 32B) of the mechanical characterization experiments. These histological sections were stained for DAPI and myelin to examine differences between gray and white matter. Quantification revealed there is significantly higher DAPI staining in gray compared to white matter at both the beginning and end of the experiment (Fig. 32C), which is consistent with a previous study [130]. There was no significant difference between the myelin at the beginning of the experiment compared to the end of the experiment, validating that the tissue did not undergo substantial degradation during our testing (Fig. 32D) and suggesting that the difference in gray and white matter mechanics is not due to differences in myelination.

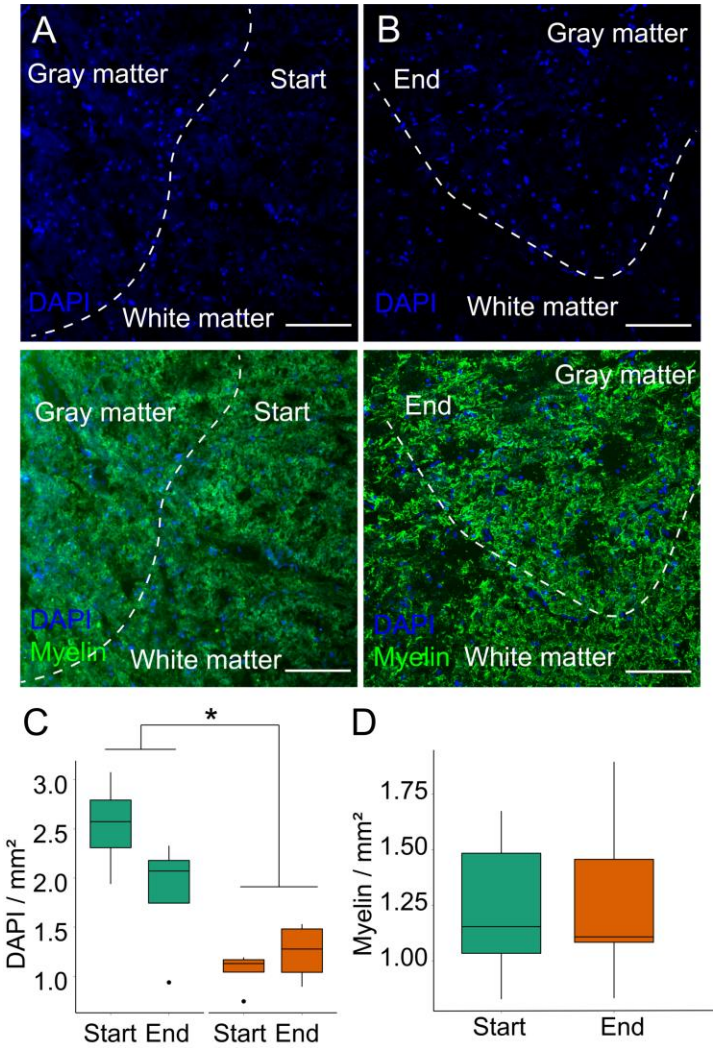

Figure 32. Immunohistochemical analysis of gray and white matter. (A) Images of cervical sections fixed at the start of the experiment and (B) immunofluorescence of sacral regions at the end of experiment. (C) Quantification of DAPI within the gray and white matter at both the beginning and end of experiment. (D) Myelin quantification normalized between gray and white matter at the beginning and end of experiment. The box plots depict the median, 25 and 75 percentiles, and the whiskers represent 1.5x the interquartile range. *$p < 0.05$ ($n = 3$).

4.4.4. 3D-Printing a Heterogeneous Spinal Cord Scaffold

A novel DLP approach was developed to fabricate a scaffold that mimicked the difference in stiffness between gray and white regions observed by microstructural mechanical testing. Figure 33A shows a schematic of the printing method, which applies varying levels of light intensity to a single z-plane using a grayscale mask. Grayscale patterns were created to alter light intensity values between 0-100%, representing black to white, to modulate the extent of polymerization of the GelMA hydrogel. In order to verify this approach, test patterns of alternating intensity were printed in square blocks. Figure 33B shows the grayscale mask used for these preliminary prints, with stripes of 1-mm thickness in a 10 x 10 x 3-mm block. Tensiometry was used to validate differences in mechanical properties. Quantification of this data and subsequent statistical analysis reveal significant differences between each stripe, demonstrating that the regions exposed to higher light intensities exhibit stiffer mechanics than the regions with lower light intensities (Fig. 33C). These results verify that heterogeneity can be achieved within the 3D-printed scaffolds to mimic the difference in stiffness between gray and white matter regions.

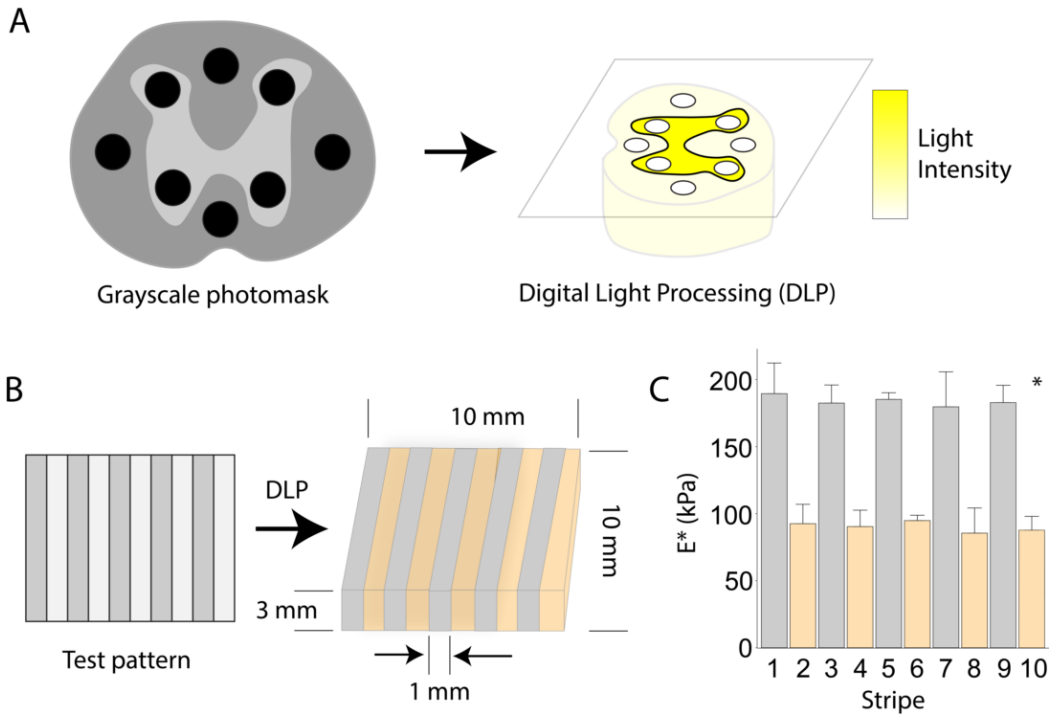

Figure 33. 3D-printing scaffolds with heterogeneity. (A) Schematic of grayscale patterns to facilitate printing of a single plane with varying levels of light intensity. (B) Preliminary 3D-printed hydrogels with heterogeneity. (C) Mechanical quantification of each stripe within the 3D-printed hydrogels. Data presented as mean ± s.d. *$p < 0.05$ ($n = 3$).

4.4.5. Characterization of Heterogeneous Scaffolds Microstructure and Mechanical Properties

Mechanical and microstructural assays were conducted to characterize the heterogeneous spinal cord scaffolds, with regions mimicking gray and white matter. Previous studies have shown that the stiffening effect in photocrosslinkable hydrogels decrease dextran diffusivity, the porosity of these scaffolds was examined using a scanning electron microscope (SEM). Figure 34A displays images of the gray and white matter regions within the homogeneous and heterogeneous scaffolds. Quantification demonstrated that the pore diameters were decreased as a result of the stiffening effect (Fig. 34B), which is consistent with a previous study [157]. In order to interrogate the mechanics of gray and white matter within the 3D-printed scaffolds, compression tests were performed on hydrogels that were exposed to higher pixel intensity to possess stiffer mechanics compared to hydrogels that were crosslinked under lower light intensities. Compression tests revealed that hydrogels exposed to the light intensity used to create the gray matter region exhibited a significantly higher elastic modulus compared to hydrogels representing white matter (Fig. 34C). Nonetheless, the compression indicated no significant difference in the Poisson ratio of the hydrogels: both white and gray matter were nearly incompressible ($\nu \sim 0.4$) (Fig. 34D). Having validated that there is a difference between the mechanical properties of scaffolds exposed to different pixel intensities, two hydrogel conditions were printed with a rat T10 geometry: homogeneous with the same mechanics throughout the conduit and heterogeneous that exhibit stiffer mechanical properties in the “butterfly” pattern to match the gray matter (Fig. 34E). Cylindrical channels with diameters of 325 μm were added to the scaffolds due to their functional

benefits of aligning axons along the rostral-caudal direction [23], [94]. Raster scans were performed on the surface of these scaffolds to provide two-dimensional elasticity maps. Figures 34F,G display representative elastic heatmaps in both the homogeneous and heterogeneous scaffolds. Two-factor ANOVAs with post-hoc Tukey tests revealed that the elasticity of the gray matter within the heterogeneous scaffolds exhibited significantly higher Young's moduli than the white matter of those scaffolds and the homogeneous hydrogels (Fig. 34H). Taken together, the data presented here demonstrate that heterogeneity in mechanics can be achieved using our 3D-printing approach to mimic native tissue.

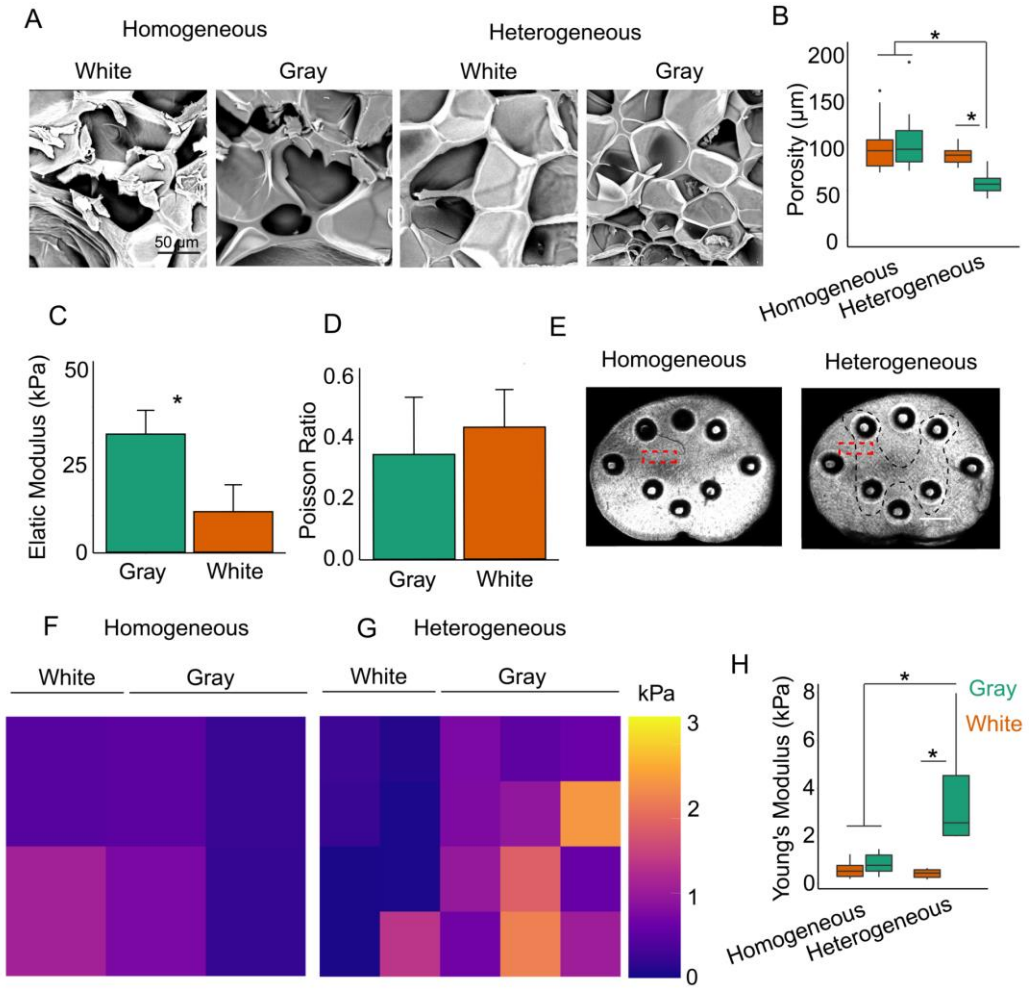

Figure 34. Interrogation of 3D-printed heterogeneous scaffolds. (A) SEM images of the gray and white matter in homogeneous and heterogeneous hydrogels. (B) Quantification of porosity within the scaffolds. (C) Mechanical testing of 3D-printed scaffolds that exhibit the mechanics of gray matter and white matter. (D) Poisson ratios of 3D-printed scaffolds. (E) Brightfield images of 3D-printed scaffolds that mimic the T10 level of rat's spinal cord and exhibit homogeneous or heterogeneous mechanics within the constructs. (F,G) Elasticity heatmaps of homogeneous and heterogeneous scaffolds. (H) Young's moduli in both the gray and white matter within homogeneous and heterogeneous hydrogels. The data in the bar graphs are represented as mean ± s.d. The box plots depict the median, 25 and 75 percentiles, and the whiskers represent 1.5x the interquartile range. *$p < 0.05$ ($n = 3$).

4.4.6. Assessing Axon Infiltration into Scaffolds with Heterogeneous Mechanical Properties

Transplantation studies were then conducted to determine whether the heterogeneous scaffolds would elicit increased axon infiltration compared to homogeneous controls. Given that specific axonal tracts are located in the white matter [23], the homogeneous scaffold exhibited mechanical properties that matched the "white matter" of the heterogeneous scaffolds. Figure 35A displays a schematic of hydrogel fabrication, injury model and transplantation of the implantation of T10 scaffolds. Immunohistochemistry examined the infiltration of axons into the channels within the white matter region of the transplanted scaffolds two weeks post-transplantation. The presence of ascending sensory-specific tracts was measured using calcitonin gene-related peptide (CGRP), a peptide widely expressed in sensory axons [140] (Fig. 35B). Quantification of $CGRP^+$ fibers demonstrated that heterogeneous scaffolds significantly augmented the infiltration of sensory axons compared to the homogeneous conditions (Fig. 35C). To further assess axon infiltration into the scaffolds, both the rostral and caudal regions of the transplanted scaffolds were examined for the presence of beta-tubulin III (Tuj) fibers. Figure 35D displays the presence of Tuj^+ axons located only in the rostral region of the scaffolds with homogeneous mechanics. However, the infiltration and outgrowth of Tuj^+ fibers were observed in both the rostral and caudal sections of the heterogeneous scaffolds (Fig. 35E), demonstrating that the mechanical heterogeneity stimulated neuronal regeneration. In order to determine whether the stiffness disparity stimulated axon growth, quantification of Tuj fibers was evaluated in the white matter regions of both scaffold types and indicated that the heterogeneous scaffolds significantly

promoted the growth of Tuj^+ fibers (Fig. 35F) and stimulated the infiltration distance compared to the homogeneous hydrogels (Fig. 35G). Overall, these results demonstrate 3D-printed scaffolds with heterogeneous mechanical properties matching the anisotropy of host tissue have beneficial effects on the infiltration and regrowth of axons, providing the basis for a new regenerative strategy to repair spinal cord injury.

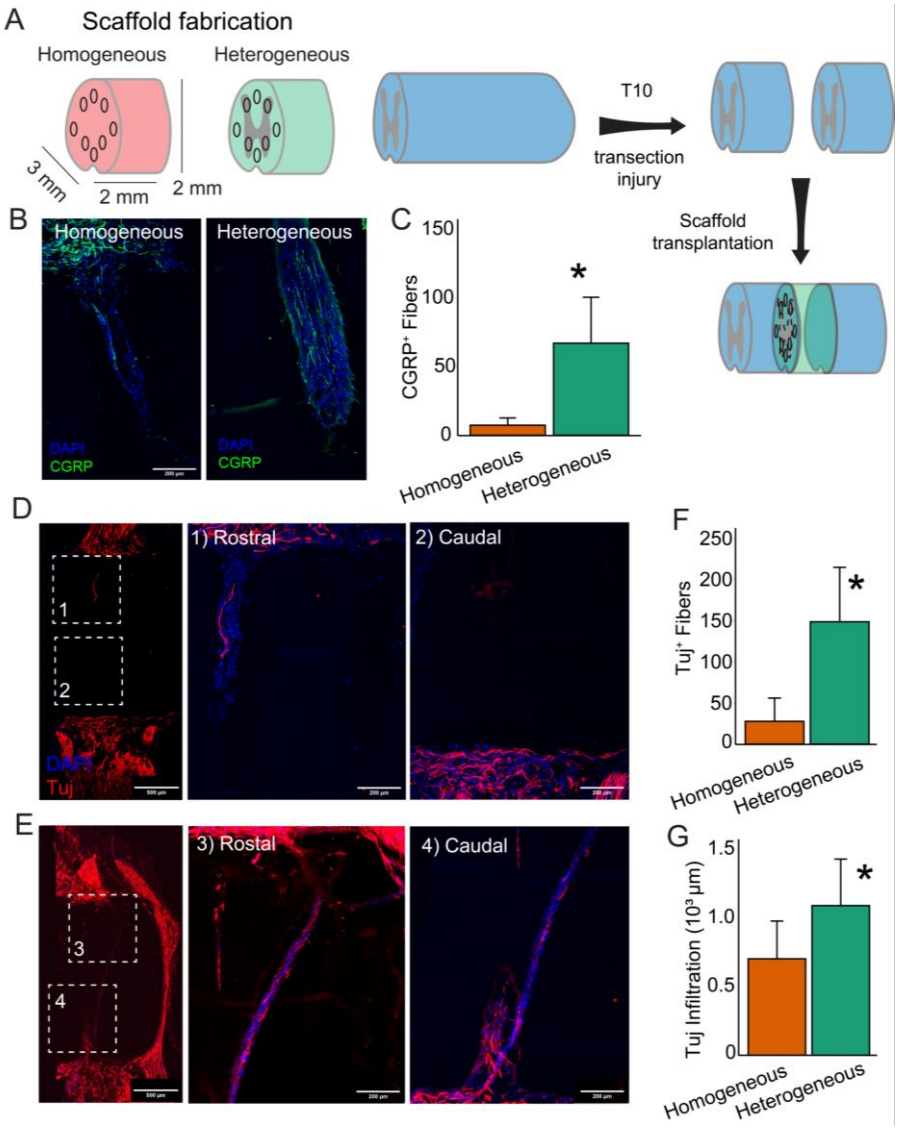

Figure 35. Examination of axon infiltration post-transplantation. (A) Schematic showing scaffold fabrication to transplantation. (B,C) Immunofluorescence and quantification of $CGRP^+$ axons infiltrating the white matter of both the homogeneous and heterogeneous scaffolds. (D,E) Infiltration of Tuj^+ fibers within the cylindrical channels located in the white matter in both scaffold conditions. Quantification of (F) Tuj+ fibers and (G) infiltrating distance in the white matter in homogeneous and heterogeneous scaffolds. The data in the bar graphs are represented as mean ± s.d. *$p < 0.05$ ($n = 3$).

Chapter V

Discussion

5.1. Vascularization of Self-Assembled Peptide Scaffolds for Spinal Cord Injury Repair

The results presented here suggest that the formation of BSCB-integrity microvessels within a self-assembling RADA-16I hydrogel reduces inflammation and scar formation at the site of a contusion SCI and increases axon infiltration into the injury site. Although it's unclear whether the observed axons were sprouting and/or regenerating from host spinal cord, the presence of the microvessels had a positive effect by either supporting the viability of the spared axons or encouraging the growth of infiltrating axons. Given that previous studies have demonstrated the ability of transplanted microvessels to anastomose with host vasculature, it is possible that the microvessels benefit the injury site through the delivery of oxygen and nutrients, though further studies are required to characterize perfusion within these transplanted vessels. Nonetheless, recent studies have also showed that vascular cells secrete neuroprotective factors [104], which is another possible mechanism by which the transplanted microvessels can augment axon density. Regardless of the underlying mechanism, the results of this work establish the benefit of transplanting microvessels within a RADA-16I peptide hydrogel.

Previous studies have demonstrated the effectiveness of RADA-16I scaffolds to incorporate with the damaged CNS and to be permissive to axon growth [37], [39], [46], [158]. Our results support these previous findings by showing both axon infiltration and strong incorporation with the host tissue in the acellular condition. Yet, our findings indicate that the presence of microvessels significantly improves the performance of the

peptide following transplantation. However, a caveat of this approach is the lack of alignment of the microvessels prior to transplantation, given that a previous study has found that transplanted microvessels can guide axon growth [8] and the results here suggest that there is strong neurovascular interaction between general axons and the microvessels. The reduced storage modulus of the peptide hydrogel precludes the ability to polymerize the scaffold prior to transplantation, necessitating the injection technique described here. Yet, exerting control over axonal orientation, specifically in the rostral-caudal direction, is a substantial advantage for scaffolds to treat SCI. Therefore, future studies to control the orientation of the microvessels that form within the peptide hydrogel are crucial. Patterning vasculature within a permissive peptide scaffold like RADA-16I holds great promise for an alternative treatment strategy to treat spinal cord injury.

Future work is also required to assess the functional benefits of transplanting vascularized scaffolds into the site of spinal cord injuries. Although 5-HT staining was used here to identify descending tracts and their interaction with the transplanted microvessels, tracing of these tracts can provide further insight into the regenerative response to the scaffolds. Beyond being limited by low sample numbers, the in vivo experiments also involved the use of cyclosporine A to limit the immune response to the transplanted scaffold and human-derived immortalized microvascular cells. Future experiments can capitalize on recent methods to differentiate induced pluripotent stem cells to tight junction forming cells [159], [160] to limit the immune response and conduct the experiments in the absence of cyclosporine A. Lastly, more studies are required to understand the dynamics of RADA-16I degradation following transplantation into the site of spinal cord injury. Previous work has demonstrated that RADA-16I can be degraded

through multiple routes [47]. In the current experiment, the scaffolds were assessed at a single two-week time point, and therefore it is unclear how much and how quickly the scaffold degrades during that time and whether the presence of the microvascular cells accelerates remodeling and degradation of the transplanted scaffold.

Nonetheless, despite the limitations of the preliminary animal experiments described here, the results establish vascularization as a general approach to improve scaffolds for SCI repair. Our findings indicate that the presence of the microvessels improves the secondary aspect of SCI, since both GFAP and ED-1 staining, markers for activated astrocytes and macrophage/microglia respectively, were reduced in response to cell-seeded scaffolds. Attenuating the detrimental effects of secondary injury and in turn decreasing the size of the injury area has the potential to facilitate neuroregeneration, and several other approaches including using chondroitinase ABC [161] and other enzymes to degrade the scar have the same goal. However, the approach of delivering a vascularized scaffold can potentially reduce scar formation while concurrently delivering nutrients and oxygen to regenerating axons. Yet, in order to fully validate the strategy of vascularized scaffolds for SCI repair, future studies must evaluate the functional benefit of these scaffolds by quantifying the behavioral response of injured animals.

5.2. Magnetic Alignment of Injectable Hydrogel Scaffolds for Spinal Cord Injury Repair

Both the *in vitro* and *in vivo* results of this work validate the strategy of using magnetic fields to align fibrous matrices, and establish magnetic alignment of injectable hydrogels as a means to provide topological cues to guide neurite growth in the damaged spinal cord. Although previous studies have demonstrated that fiber alignment can be

manipulated by magnetism in various scaffolds [17]–[19], [21], the findings presented here demonstrate the validity of this approach to *in vivo* applications. The results show that magnetically aligned peptide hydrogels provide topological cues as guidance for axon alignment *in vitro*, and that this method of post-injection alignment can be applied to spinal cord injury. Magnetic alignment creates an anisotropic environment that is physiologically relevant to the native ECM of the spinal cord since previous results have determined the importance of aligning structures in the rostral-caudal direction [32], [54]. Our findings highlight the biocompatibility of MP-seeded scaffolds on cell viability via *in vitro* studies using co-cultures of hMSCs and NPCs to assess axon growth and *in vivo* experiments to quantify host axon infiltration. Taken together, the results demonstrate the benefits of post-injection alignment through magnetism to rapidly facilitate fiber orientation.

In addition to verifying the ability of magnetic fields to align fibrous matrices following transplantation, the results also suggest that cell therapies augment the regenerative effects of magnetic alignment. Although previous studies have shown that topology harnesses physical cues to control neurite extension along the direction of alignment [162]–[164], the presence of hMSC provides a complementary effect on supporting the growth of infiltrating axons and amplifying axon alignment. The BDNF ELISA results reveal that the additive effects of scaffold alignment and hMSC seeding significantly increases the production of the neurotrophic factor *in vitro*. Future studies are needed to determine whether the hMSC-seeded scaffolds encourage axon infiltration through BDNF secretion in the animal model. In addition, further studies will interrogate whether the increase in axonal alignment and growth causes a functional benefit as well. Nevertheless, the results here exhibit the benefits of combining magnetic alignment with

cell-seeded scaffolds to encourage axons to regrow into the injury site in the rostral-caudal direction.

The ability to align hydrogel fibers from outside the body distinguishes this approach from previous means to modify scaffolds *in vivo*. Previous studies have evaluated various complex light- and pH-sensitive hydrogel platforms as potential therapies for tissue engineering. However, tissue density prevents light from penetrating into various areas of the body such as the skull and spine [62], [74], [75], [129]. Here, we demonstrate the ability to align scaffold fibers with magnetic fields, which are not limited by the restrictions of UV-light used for photocrosslinkable hydrogels [62], [165], [166]. Magnetic fields can conceivably be applied during transplantation in human patients, though future studies are required to determine potential issues involved with clearance of carbonyl iron microparticles and long-term remodeling of the scaffold. Furthermore, this work also facilitates future studies interrogating the use of magnetic fields to dynamically tune ECM mechanics *in vivo*. Previous work has found that glial scars exhibit lower stiffnesses than surrounding tissue in the days and weeks following CNS injury, which may contribute to neurodegeneration [165]. Our previous results have demonstrated that scaffold mechanics can be rapidly and reversibly altered by applying and removing an external magnetic field to control astrocyte morphology and mechanotransduction [166]. Thus, injecting hydrogels seeded with MPs into the nervous system can potentially be used to tune mechanical properties to encourage neuroregeneration. Therefore, these results identify a new strategy to tune both the mechanics and alignment of scaffolds for spinal cord recovery.

5.3. Dynamic Tuning of Protein Hydrogel Mechanics with Carbonyl Iron Microparticles Guides Three-Dimensional Cell Mechanotransduction

The results presented here demonstrate that magnetic tuning of hydrogel mechanics yields a new means to study cell mechanobiology in 3D environments. One of the advantages of using MPs to dynamically alter 3D hydrogel mechanics is the ability to generalize this approach across multiple hydrogel systems and platforms. Several recent studies have examined the magnetorheological properties of MPs embedded in various hydrogels including carrageenan [79], [167], alginate [168] and acrylamide [82]. Here, we demonstrate that the stiffness of several different hydrogel formulations (collagen, fibrin, collagen-hyaluronan) compatible with multiple different cell types (smooth muscle cells and astrocytes) can be altered without any modification to crosslinking chemistry or ligand density. Therefore, researchers using in vitro systems to study cell mechanobiology in 3D geometries can use MPs to dynamically alter ECM mechanics by the simple application of a magnetic field. Showing that the magnetic field does not cause measurable displacement of the MPs after gel polymerization suggests that the pore size and microstructure of the hydrogel is not altered, indicating that the magnetic field changes hydrogel mechanics independent of any effect on ligand density or topology. Therefore, magnetically active hydrogels can complement the complex light- and pH-sensitive approaches that have been used previously [74], [75], [129], which all require specific chemistries and substrates, providing a broadly adaptable alternative [169], [170]. The results presented here mirror several results from studies using photo-crosslinkable chemistries, specifically the inability of cells to spread within hydrogels exhibiting storage moduli that exceed 10 kPa [74], [129]. But they also demonstrate the potential for magnetically tunable hydrogels to

provide new insight into the dynamics of cell mechanotransduction, showing that cells allowed to spread in a lower stiffness environment increase their nuclear translocation of YAP as the hydrogel becomes stiffer and instantaneous alteration of ECM mechanics results in immediate changes to calcium handling within cells in 3D.

The near-instantaneous effect of magnetic stiffening and its rapid reversibility distinguish this approach from previous means of dynamically altering 3D substrate mechanics. As shown in the rheological tests, removal of the magnetic field returns the hydrogel to its original mechanical properties nearly instantaneously. The analytical model and confocal microscopy experiments provide some insight into the mechanisms underlying these effects. In the presence of a magnetic field, the MPs likely form dipoles that resist any motion relative to adjacent particles. The application of an external mechanical stimulus causes the ferromagnetic particles to become misaligned and results in antisymmetric stresses, and thus contributes to the increase of shear modulus as demonstrated in rheological studies. Due to the stiffening effect, this resistance gives rise to the increase in hydrogel stiffness in the presence of the magnetic field, and also explains how removal of the magnetic field returns the fibrous networks to their original state. Previous studies that have demonstrated the concentration of carbonyl iron MPs substantially affect the stiffness of the hydrogel conclude that particle dispersibility contributes to a drastic change in elastic modulus compared to highly organized magnetic chains [79], [80], which supports this proposed mechanism. The rheological data and live cell experiments, which represent the global and local application of force respectively, both demonstrate that MP displacement is impeded in the presence of magnetic fields and subsequently stiffen the fibrous network. Thus, removing the magnetic field abruptly ends

the stiffening effect, yielding a means to transiently and reversibly alter hydrogel mechanics.

The rapid and reversible nature of magnetic stiffening provides new insight into both short-term and chronic characteristics of the cell response. As evidenced by the calcium transient studies, smooth muscle cells respond to the stiffness of the surrounding matrix within seconds by altering the rate of calcium influx and period of the calcium transient. The MR hydrogels therefore provide a platform for future studies to interrogate the underlying molecular mechanisms by which cells sense the mechanics of their environment and alter calcium handling and actomyosin force generation within very short time scales. The morphology and YAP measurements in astrocytes also demonstrate how this technique can be used to study longer term aspects of the cell response. A previous study has shown that cells readily uptake magnetic microparticles with diameters as large as 5.8 μm without affecting cell function [171]. Therefore, the effect of dynamic stiffness on gene expression can be evaluated by probing the transcriptional state of the cells in hydrogels undergoing controlled changes in rheological properties. In this way, magnetic hydrogels provide a new means to study cell-ECM interactions in the context of various tissues. There are several physiological and pathological processes involving time-dependent changes to ECM mechanics that can be mimicked by dynamic and reversible modification of hydrogel stiffness: cardiac fibrosis [172]–[174], wound healing [175], [176], tumor metastasis [177], [178], and atherosclerosis [179], [180] are all relevant examples. Beyond the time-dependent studies presented here, focusing of magnetic fields within sub-millimeter loci can create well-defined spatial gradients. Therefore, MP-seeded

hydrogels can interrogate the effects of local stiffening within 3D in vitro blood vessel models and other microfluidic applications.

There is also the potential to use protein-based MR hydrogels in applications related to tissue engineering, given the cytocompatibility of the MPs [78], [82] and the ability of magnetic fields to penetrate further into tissue than the UV light used for photocrosslinkable chemistries [62], [165], [166]. There is specific relevance for central nervous system (CNS) injury, given the results related to controlling astrocyte morphology and YAP translocation to the nucleus. Previous studies have found glial scars that form in the aftermath of CNS injury exhibit a lower stiffness than surrounding tissue, which may affect neuroregeneration [16]. Implanting hydrogels seeded with MPs into the cord provides a means to dynamically alter the stiffness of the scaffold during the healing process to encourage axon infiltration and outgrowth from the injury area. Due to the presence of the skull and spine, the CNS is also a good example of a tissue that would not be compatible with UV-photocrosslinkable means of tuning scaffold mechanical properties [62]. Overall, the flexibility of magnetic hydrogels amplifies its potential use for both in vitro and in vivo applications.

5.4. Matching Mechanical Heterogeneity of the Native Spinal Cord Augments Axon Infiltration in 3D-Printed Scaffolds

The results demonstrate that mimicking the stiffness disparity between gray and white matter in an implantable scaffold encourages axon growth at the site of a rat spinal cord transection injury. Previous studies have demonstrated that multicellular migration is enhanced along a gradient in the rigidity of the extracellular matrix, referred to as durotaxis, in both in vivo [181] and in vitro [182], [183] microenvironments. In contrast, the stiffness

gradient used here is orthogonal to the direction of axonal growth, though this gradient is more representative of native spinal cord tissue. The mechanical testing conducted in this work indicates that the inner gray matter is stiffer than the surrounding white matter in the cord, and the mechanics of the cord do not change along the rostral-caudal axis. The primary goal of a spinal cord scaffold or conduit is to encourage axon growth in the rostral-caudal direction to restore connectivity across the site of injury, since axon tracts are primarily aligned in this direction [23], [32], [103]. Therefore, the axons infiltrating the scaffold are not growing along a rigidity gradient, but like axon tracts in native tissue, they are growing perpendicular to a disparity in matrix stiffness. Consequently, the mechanisms underlying increased axon infiltration in heterogeneous scaffolds compared to homogenous controls are likely different than those identified in previous durotaxis studies, including specific cell-matrix interactions [184], [185] and small GTPase-mediated actomyosin contractility [186]–[188]. Future studies are therefore required to understand the molecular mechanisms responsible for the increased axon growth into the heterogeneous scaffolds.

The modification to digital light processing described here enables 3D-printing of complex topologies within mechanically heterogeneous hydrogels. DLP is a powerful tool for recreating complex tissue architectures in hydrogels, though previously the method has been limited to printing scaffolds exhibiting homogenous mechanics. However, other existing 3D-printing approaches are capable of printing interfacial and heterogeneous structures. For example, extrusion-based methods have been used to create heterogeneous aortic valve scaffolds [189]. But these methods are not applicable to softer, cell-permeable hydrogels, which are more appropriate for printing scaffolds with mechanics that match

soft tissue like the spinal cord. And although 3D-printed scaffolds with elastic moduli greater than 200 kPa have been implanted within the spinal cord and demonstrated axon infiltration [23], DLP can recreate native tissue topology while also incorporating cell-based therapies by creating cell-permeable scaffolds with elastic moduli less than 10 kPa. Therefore, advancing DLP technology to print hydrogels with spatially varying mechanics provides a pathway to create scaffolds that better mimic the anisotropy of a variety of native tissues, and specifically to harness durotaxis by fabricating hydrogels that control cell growth and migration.

As advances in 3D-printing technology are made to mimic native tissue, one limitation to fabricating scaffolds that recreate the in vivo microenvironment is our understanding of complex tissue mechanics. Tissue mechanical properties are a function of multiple length scales, creating heterogeneity that is difficult to characterize and then implement in 3D-printed constructs. In this specific aim, a variety of mechanical testing, including rheology and atomic force microscopy, characterize spinal cord tissue ex vivo. These studies indicate that the macroscale mechanical properties of the spinal cord change as a function of level. Although previous work has shown that the mechanics of the cord are different based on the type of sectioning (e.g. coronal, sagittal, or transverse) [130], these results are the first to find differences in mechanical properties along the cord. Combining macroscale with microscale mechanical testing indicated that although the bulk mechanics differ along the cord, the mechanics of white matter and gray matter remain constant and gray matter is stiffer than white matter. Therefore, the differences in rheological properties arise from differences in the percentage of gray matter in the coronal section and not intrinsic disparity between levels. These findings justify the DLP-based

approach to fabricate scaffolds that recreate a stiffer inner region to mimic the difference in gray-white matter mechanics. However, one aspect of the spinal cord tissue mechanics that the scaffolds do not mimic is viscoelasticity: the GelMA scaffolds are primarily elastic even though tensiometry indicated that gray matter exhibited higher stress relaxation. Therefore, there is a need for photoinks with tunable viscoelasticity, especially for tissues like the spinal cord that exhibit these properties.

Nonetheless, the DLP approach described here has the flexibility to incorporate existing neurotrophic therapies. As mentioned, in contrast to other 3D-printing approaches, the GelMA scaffolds printed for these studies are compatible with cell seeding. There are currently ongoing clinical trials evaluating the efficacy of intrathecal injection of mesenchymal stem cells (MSC) in spinal cord injury patients [59], with evidence that MSCs release neurotrophic factors to stimulate axon growth and connectivity. Therefore, future studies will interrogate the benefit of incorporating MSCs into the heterogeneous scaffolds following implantation at the site of injury. In contrast to intrathecal injection, this approach can augment the residence time for MSCs at the site of injury and determine whether longer retention is beneficial. Moreover, the composition of the scaffold is also tunable. Although GelMA is used here, the DLP approach is compatible with other photoinks. Therefore, printing heterogeneous mechanics in degradable [190] or electrically conductive[105] photoinks provides a new means to combine different aspects of regenerative approaches in a multifunctional scaffold that mimics the mechanical anisotropy of native tissue.

5.5. Conclusion, Impact, and Outlook

While bioengineered scaffolds have been extensively studied, the techniques and results described in this dissertation yield numerous biological insights that can inform therapeutic strategies for spinal cord injury repair. The primary findings of the specific aims are as follows:

1. Self-assembled peptide hydrogels support neuronal regeneration, and vascularization of these scaffolds augments axon infiltration and attenuates inflammation and astrogliosis.
2. Injectable, magnetically-responsive peptide hydrogels provide rostral-caudal guidance cues, and the incorporation of mesenchymal stem cells increases axon regrowth through BDNF secretion.
3. 3D-printed scaffolds with heterogenous mechanical properties that mimic the gray and white matter promote regeneration of axons in a transection spinal cord injury model.

The results from these experiments demonstrate the potential translational benefit of bioengineering scaffolds to repair spinal cord injury. Fabricating injectable hydrogels with rostral-caudal alignment and 3D-printing scaffolds with mechanical anisotropy both promote axon regrowth. Moreover, the transplantation of cell-seeded scaffolds exhibits primary and secondary benefits in promoting axon infiltration and attenuating inflammation in both injectable and solid scaffolds. These two modalities of bioengineered scaffolds provide physical guidance cues to control host axon infiltration along the rostral-caudal direction, which is the native orientation of the spinal cord. Overall, the novel

techniques developed in this dissertation create the foundation for new regenerative strategies to repair the damaged spinal cord.

Although the work advances the field of tissue engineering and regenerative medicine, there are still several caveats that must be addressed in future studies:

1. The magnetic particles can become oxidized and cytotoxic to the cells within the matrix. Future experiments will be needed to interrogate biocompatible coatings of particles that do not affect any magnetic or rheological properties.
2. Since 3D-printed scaffolds with mechanical heterogeneity have shown to improve axon infiltration, future approaches will needed to incorporate cells within these constructs.
3. Since gelatin-methacrylate (GelMA) is derived from a bovine source, there is a need for biomaterial innovations to create photocrosslinkable scaffolds with synthesized peptides. Additionally, GelMA is predominantly linearly elastic, but our results show that spinal cord tissue is viscoelastic. Future experiments will be needed to tune the viscoelasticity of 3D-printed scaffolds to fully mimic the mechanical properties of native tissue.
4. The 3D-printing techniques described in this dissertation indicate axon infiltration, but likely not enough to result in functional improvements following injury. Future experiments will need to investigate the ability to incorporate additional strategies such as conductive polymers to improve the efficacy of transplanted scaffolds.

While the current work demonstrates that magnetic fields facilitate rostral-caudal alignment, future experiments will need to interrogate the long-term effects of embedding

magnetic particles in RADA-16I. One aspect of improving magnetically-responsive biomaterials is to functionalize magnetic particles with a protective polymer to optimize cell viability. Previous studies have demonstrated the ability to coat the particles with either silica or polystyrene without diminishing the rheological effects to maintain the cell viability within the fabricated scaffolds [191], [192]. These studies would facilitate long-term spinal cord studies for behavioral analysis. Despite the lack of behavioral analysis presented in this dissertation, future experiments can be designed to perform the Louisville Swim Scale (LSS) as a novel assessment of hindlimb function for rats that undergo contusion spinal cord injuries [193].

The benefits of incorporating both vascular and mesenchymal stem cells in our scaffolds suggest that cells should also be incorporated in the 3D-printed constructs with mechanical heterogeneity. The ability to harvest and generate custom constructs using a patient's own cells can prevent a host inflammatory response during transplantation. Future clinical work can isolate mesenchymal stem cells directly from patients to incorporate with our magnetically-aligned injectable or 3D-printed platforms for cell-scaffold-based therapies to repair the spinal cord. Moreover, future techniques can explore the fabrication of functional scaffolds by 3D-printing blood-brain barrier vasculature to provide the required nutrients for sustained axon proliferation. The results from the first specific aim demonstrate the primary and secondary benefits of transplanting microvessels, but vascularizing 3D-printed scaffolds on a capillary scale has yet to be achieved due to limitations in the printability of the device. As the field of 3D-printing advances, refinement of printing resolution can be used to generate microvasculature in the scaffolds.

While the approach described in this dissertation often relies on gelatin-methacrylate (GelMA), synthesizing new peptide-based bioinks for 3D-printed constructs would eliminate the need for bovine-sourced gelatin. Novel chemistries that provide more flexibility in hydrogel mechanical properties and allow for tuning of cell-matrix interactions can potentially improve the regenerative capability of 3D-printed scaffolds. Another caveat to GelMA bioinks is that they are linearly elastic, whereas the mechanical testing data showed that the spinal cord tissue is viscoelastic. Future studies can incorporate gellan gum, a polysaccharide able to tune the loss angle of the hydrogel without significantly changing the storage modulus. Future studies can determine whether mimicking the viscoelastic properties of native tissue can increase axon infiltration into the scaffold.

While we have developed a novel technique to 3D-print mechanical heterogeneity within the constructs, there are ongoing efforts to develop functional bioinks that can provide an electrically conductive microenvironment. Conductive polymers have been traditionally used in a wide variety of tissue engineering applications (bone, cardiac, nerve and muscle) [105]. In terms of spinal cord injury, previous studies have demonstrated that transplantation of microfibers with electrically active polymers (PEDOT:PSS) augments blood vessel formation and axonal regeneration while reducing astrogliosis. Combining conductive bioinks with the ability to fabricate heterogeneous mechanical properties scaffolds holds great promise for a multifunctional scaffold to repair the damaged spinal cord.

References

[1] J. W. McDonald and C. Sadowsky, "Spinal-cord injury," *Lancet*, vol. 359, no. 9304, pp. 417–425, 2002, doi: 10.1016/S0140-6736(02)07603-1.

[2] S. Thuret, L. D. F. Moon, and F. H. Gage, "Therapeutic interventions after spinal cord injury," *Nature Reviews Neuroscience*, vol. 7, no. 8, pp. 628–643, 2006, doi: 10.1038/nrn1955.

[3] T. K. McIntosh, M. Juhler, and T. Wieloch, "Novel pharmacologic strategies in the treatment of experimental traumatic brain injury: 1998," *Journal of Neurotrauma*, vol. 15, no. 10, pp. 731–769, 1998, doi: 10.1089/neu.1998.15.731.

[4] C. H. Tator and I. Koyanagi, "Vascular mechanisms in the pathophysiology of human spinal cord injury," *Journal of Neurosurgery*, vol. 86, no. 3, pp. 483–492, 1997, doi: 10.3171/jns.1997.86.3.0483.

[5] N. B. Jain *et al.*, "Traumatic spinal cord injury in the United States, 1993-2012," *JAMA - Journal of the American Medical Association*, vol. 313, no. 22, pp. 2236–2243, 2015, doi: 10.1001/jama.2015.6250.

[6] J. E. Lasfargues, D. Custis, F. Morrone, J. Carswell, and T. Nguyen, "A model for estimating spinal cord injury prevalence in the United States," *Paraplegia*, vol. 33, no. 2, pp. 62–68, 1995, doi: 10.1038/sc.1995.16.

[7] B. B. Lee, R. A. Cripps, M. Fitzharris, and P. C. Wing, "The global map for traumatic spinal cord injury epidemiology: Update 2011, global incidence rate," *Spinal Cord*, vol. 52, no. 2, pp. 110–116, 2014, doi: 10.1038/sc.2012.158.

[8] M. Wyndaele and J. J. Wyndaele, "Incidence, prevalence and epidemiology of spinal cord injury: What learns a worldwide literature survey?," *Spinal Cord*, vol. 44, no. 9, pp. 523–529, 2006, doi: 10.1038/sj.sc.3101893.

[9] L. H. S. Sekhon and M. G. Fehlings, "Epidemiology, demographics, and pathophysiology of acute spinal cord injury," *Spine (Phila Pa 1976)*, vol. 26, no. 24 SUPPL., 2001, doi: 10.1097/00007632-200112151-00002.

[10] G. Yiu and Z. He, "Glial inhibition of CNS axon regeneration," *Nature Reviews Neuroscience*, vol. 7, no. 8, pp. 617–627, 2006, doi: 10.1038/nrn1956.

[11] S. Karimi-Abdolrezaee and R. Billakanti, "Reactive astrogliosis after spinal cord injury-beneficial and detrimental effects," *Molecular Neurobiology*, vol. 46, no. 2, pp. 251–264, 2012, doi: 10.1007/s12035-012-8287-4.

[12] K. B. Casper and K. D. McCarthy, “GFAP-positive progenitor cells produce neurons and oligodendrocytes throughout the CNS,” *Molecular and Cellular Neuroscience*, vol. 31, no. 4, pp. 676–684, 2006, doi: 10.1016/j.mcn.2005.12.006.

[13] M. Karsy and G. Hawryluk, “Modern Medical Management of Spinal Cord Injury,” *Current Neurology and Neuroscience Reports*, vol. 19, no. 9, 2019, doi: 10.1007/s11910-019-0984-1.

[14] Q. Huang *et al.*, “Spinal Cord Stimulation for Pain Treatment After Spinal Cord Injury,” *Neuroscience Bulletin*, vol. 35, no. 3, pp. 527–539, 2019, doi: 10.1007/s12264-018-0320-9.

[15] K. Venkatesh, S. K. Ghosh, M. Mullick, G. Manivasagam, and D. Sen, “Spinal cord injury: pathophysiology, treatment strategies, associated challenges, and future implications,” *Cell and Tissue Research*, vol. 377, no. 2, pp. 125–151, 2019, doi: 10.1007/s00441-019-03039-1.

[16] E. Moeendarbary *et al.*, “The soft mechanical signature of glial scars in the central nervous system,” *Nature Communications*, vol. 8, pp. 1–11, 2017, doi: 10.1038/ncomms14787.

[17] M. Antman-Passig and O. Shefi, “Remote Magnetic Orientation of 3D Collagen Hydrogels for Directed Neuronal Regeneration,” *Nano Letters*, vol. 16, no. 4, pp. 2567–2573, 2016, doi: 10.1021/acs.nanolett.6b00131.

[18] C. D. L. Johnson *et al.*, “Injectable, Magnetically Orienting Electrospun Fiber Conduits for Neuron Guidance,” *ACS Applied Materials and Interfaces*, vol. 11, no. 1, pp. 356–372, 2019, doi: 10.1021/acsami.8b18344.

[19] A. Omidinia-Anarkoli, S. Boesveld, U. Tuvshindorj, J. C. Rose, T. Haraszti, and L. de Laporte, “An Injectable Hybrid Hydrogel with Oriented Short Fibers Induces Unidirectional Growth of Functional Nerve Cells,” *Small*, vol. 13, no. 36, pp. 1–8, 2017, doi: 10.1002/smll.201702207.

[20] J. C. Rose, M. Cámara-Torres, K. Rahimi, J. Köhler, M. Möller, and L. de Laporte, “Nerve Cells Decide to Orient inside an Injectable Hydrogel with Minimal Structural Guidance,” *Nano Letters*, vol. 17, no. 6, pp. 3782–3791, 2017, doi: 10.1021/acs.nanolett.7b01123.

[21] O. Kriha *et al.*, “Connection of hippocampal neurons by magnetically controlled movement of short electrospun polymer fibers - A route to magnetic micromanipulators,” *Advanced Materials*, vol. 19, no. 18, pp. 2483–2485, 2007, doi: 10.1002/adma.200601937.

[22] K. M. Pawelec, J. Hix, E. M. Shapiro, and J. Sakamoto, “The mechanics of scaling-up multichannel scaffold technology for clinical nerve repair,” *Journal of the Mechanical Behavior of Biomedical Materials*, vol. 91, pp. 247–254, Mar. 2019, doi: 10.1016/j.jmbbm.2018.12.016.

[23] J. Koffler *et al.*, “Biomimetic 3D-printed scaffolds for spinal cord injury repair,” *Nature Medicine*, 2019, doi: 10.1038/s41591-018-0296-z.

[24] B. Grigoryan *et al.*, “Multivascular networks and functional intravascular topologies within biocompatible hydrogels,” *Science (1979)*, vol. 364, no. 6439, pp. 458–464, 2019, doi: 10.1126/science.aav9750.

[25] Y. Zhao *et al.*, “Clinical Study of NeuroRegen Scaffold Combined with Human Mesenchymal Stem Cells for the Repair of Chronic Complete Spinal Cord Injury,” *Cell Transplantation*, vol. 26, no. 5, pp. 891–900, 2017, doi: 10.3727/096368917x695038.

[26] A. E. Haggerty, “Biomaterials for spinal cord repair,” vol. 29, no. 4, pp. 445–459, 2013, doi: 10.1007/s12264-013-1362-7.

[27] M. Tsintou, K. Dalamagkas, and A. M. Seifalian, “Advances in regenerative therapies for spinal cord injury: A biomaterials approach,” *Neural Regeneration Research*, vol. 10, no. 5, pp. 726–742, 2015, doi: 10.4103/1673-5374.156966.

[28] Q. Han *et al.*, “The promotion of neural regeneration in an extreme rat spinal cord injury model using a collagen scaffold containing a collagen binding neuroprotective protein and an EGFR neutralizing antibody,” *Biomaterials*, vol. 31, no. 35, pp. 9212–9220, 2010, doi: 10.1016/j.biomaterials.2010.08.040.

[29] L. Riemann *et al.*, “Transplantation of neural precursor cells attenuates chronic immune environment in cervical spinal cord injury,” *Frontiers in Neurology*, vol. 9, no. JUN, pp. 1–12, 2018, doi: 10.3389/fneur.2018.00428.

[30] B. Shrestha, K. Coykendall, Y. Li, A. Moon, P. Priyadarshani, and L. Yao, “Repair of injured spinal cord using biomaterial scaffolds and stem cells,” *Stem Cell Research and Therapy*, vol. 5, no. 4, pp. 1–11, 2014, doi: 10.1186/scrt480.

[31] A. C. Lepore, A. Bakshi, S. A. Swanger, M. S. Rao, and I. Fischer, “Neural precursor cells can be delivered into the injured cervical spinal cord by intrathecal injection at the lumbar cord,” *Brain Research*, vol. 1045, no. 1–2, pp. 206–216, 2005, doi: 10.1016/j.brainres.2005.03.050.

[32] P. P. Partyka *et al.*, “Harnessing neurovascular interaction to guide axon growth,” *Scientific Reports*, vol. 9, no. 1, pp. 1–10, 2019, doi: 10.1038/s41598-019-38558-y.

[33] H. Chen *et al.*, “Effect of hypoxia-inducible factor-1/vascular endothelial growth factor signaling pathway on spinal cord injury in rats,” *Experimental and Therapeutic Medicine*, vol. 13, no. 3, pp. 861–866, 2017, doi: 10.3892/etm.2017.4049.

[34] A. Zimna and M. Kurpisz, “Hypoxia-Inducible Factor-1 in Physiological and Pathophysiological Angiogenesis: Applications and Therapies,” *BioMed Research International*, vol. 2015, pp. 1–13, 2015, doi: 10.1155/2015/549412.

[35] D. Basagiannis *et al.*, “VEGF induces signalling and angiogenesis by directing VEGFR2 internalisation via macropinocytosis.,” *Journal of Cell Science*, p. jcs.188219, 2016, doi: 10.1242/jcs.188219.

[36] C. Dray, G. Rougon, and F. Debarbieux, “Quantitative analysis by in vivo imaging of the dynamics of vascular and axonal networks in injured mouse spinal cord,” *Proceedings of the National Academy of Sciences*, vol. 106, no. 23, pp. 9459–9464, 2009, doi: 10.1073/pnas.0900222106.

[37] J. Guo *et al.*, “Reknitting the injured spinal cord by self-assembling peptide nanofiber scaffold,” *Nanomedicine: Nanotechnology, Biology, and Medicine*, vol. 3, no. 4, pp. 311–321, 2007, doi: 10.1016/j.nano.2007.09.003.

[38] J. Guo *et al.*, “Self-assembling peptide nanofiber scaffold promotes the reconstruction of acutely injured brain,” *Nanomedicine: Nanotechnology, Biology, and Medicine*, vol. 5, no. 3, pp. 345–351, 2009, doi: 10.1016/j.nano.2008.12.001.

[39] Y.-X. Liang *et al.*, “Nano neuro knitting: Peptide nanofiber scaffold for brain repair and axon regeneration with functional return of vision,” *Proceedings of the National Academy of Sciences*, vol. 103, no. 13, pp. 5054–5059, 2006, doi: 10.1073/pnas.0600559103.

[40] M. E. Davis *et al.*, “Local myocardial insulin-like growth factor 1 (IGF-1) delivery with biotinylated peptide nanofibers improves cell therapy for myocardial infarction,” vol. 1, no. 19, pp. 19–24, 2006.

[41] T. C. Holmes, S. de Lacalle, X. Su, G. Liu, A. Rich, and S. Zhang, “Extensive neurite outgrowth and active synapse formation on self-assembling peptide scaffolds,” 2000.

[42] T. C. Holmes, “Novel peptide-based biomaterial scaffolds for tissue engineering,” *Trends in Biotechnology*, vol. 20, no. 1, pp. 16–21, 2002, doi: 10.1016/S0167-7799(01)01840-6.

[43] S. Zhang, F. Gelain, and X. Zhao, “Designer self-assembling peptide nanofiber scaffolds for 3D tissue cell cultures,” *Seminars in Cancer Biology*, vol. 15, no. 5 SPEC. ISS., pp. 413–420, 2005, doi: 10.1016/j.semcancer.2005.05.007.

[44] S. Zhang, “Fabrication of novel biomaterials through molecular self-assembly,” no. March, pp. 1171–1178, 2017, doi: 10.1038/nbt874.

[45] E. G. Bahima, “Osteogenic Differentiation of Mouse Embryonic Stem Cells,” no. September, 2006, doi: 10.1089/ten.2006.12.2215.

[46] L. Y. Sang, Y. Liang, and Y. Li, “A self-assembling nanomaterial reduces acute brain injury and enhances functional recovery in a rat model of intracerebral hemorrhage,” *Nanomedicine: Nanotechnology, Biology, and Medicine*, vol. 11, no. 3, pp. 611–620, 2015, doi: 10.1016/j.nano.2014.05.012.

[47] A. L. Sieminski, A. S. Was, G. Kim, H. Gong, and R. D. Kamm, “The Stiffness of Three-dimensional Ionic Self-assembling Peptide Gels Affects the Extent of Capillary-like Network Formation,” pp. 73–83, 2007, doi: 10.1007/s12013-007-0046-1.

[48] C. M. Dumont *et al.*, “Aligned hydrogel tubes guide regeneration following spinal cord injury,” *Acta Biomaterialia*, vol. 86, pp. 312–322, 2019, doi: 10.1016/j.actbio.2018.12.052.

[49] C. D. L. Johnson *et al.*, “Injectable, Magnetically Orienting Electrospun Fiber Conduits for Neuron Guidance,” *ACS Applied Materials & Interfaces*, vol. 11, no. 1, pp. 356–372, Jan. 2019, doi: 10.1021/acsami.8b18344.

[50] W. Zhu, F. Masood, J. O’Brien, and L. G. Zhang, “Highly aligned nanocomposite scaffolds by electrospinning and electrospraying for neural tissue regeneration,” *Nanomedicine: Nanotechnology, Biology and Medicine*, vol. 11, no. 3, pp. 693–704, Apr. 2015, doi: 10.1016/j.nano.2014.12.001.

[51] K. Pawar *et al.*, “Biomaterial bridges enable regeneration and re-entry of corticospinal tract axons into the caudal spinal cord after SCI: Association with recovery of forelimb function,” *Biomaterials*, vol. 65, no. 2015, pp. 1–12, 2015, doi: 10.1016/j.biomaterials.2015.05.032.

[52] S. Stokols and M. H. Tuszynski, “Freeze-dried agarose scaffolds with uniaxial channels stimulate and guide linear axonal growth following spinal cord injury,” *Biomaterials*, vol. 27, no. 3, pp. 443–451, 2006, doi: 10.1016/j.biomaterials.2005.06.039.

[53] S. Stokols and M. H. Tuszynski, “The fabrication and characterization of linearly oriented nerve guidance scaffolds for spinal cord injury,” *Biomaterials*, vol. 25, no. 27, pp. 5839–5846, 2004, doi: 10.1016/j.biomaterials.2004.01.041.

[54] J. Koffler *et al.*, “Biomimetic 3D-printed scaffolds for spinal cord injury repair,” *Nature Medicine*, vol. 25, no. 2, pp. 263–269, 2019, doi: 10.1038/s41591-018-0296-z.

[55] Z. Cao *et al.*, “Directional axonal regrowth induced by an aligned fibrin nanofiber hydrogel contributes to improved motor function recovery in canine L2 spinal cord injury,” *Journal of Materials Science: Materials in Medicine*, vol. 31, no. 5, 2020, doi: 10.1007/s10856-020-06375-9.

[56] E. Schnell *et al.*, “Guidance of glial cell migration and axonal growth on electrospun nanofibers of poly-ε-caprolactone and a collagen/poly-ε-caprolactone blend,” *Biomaterials*, vol. 28, no. 19, pp. 3012–3025, 2007, doi: 10.1016/j.biomaterials.2007.03.009.

[57] S. Zhang *et al.*, “Creating polymer hydrogel microfibres with internal alignment via electrical and mechanical stretching,” *Biomaterials*, vol. 35, no. 10, pp. 3243–3251, 2014, doi: 10.1016/j.biomaterials.2013.12.081.

[58] S. B. Riemenschneider *et al.*, “Inosculation and perfusion of pre-vascularized tissue patches containing aligned human microvessels after myocardial infarction,” *Biomaterials*, vol. 97, pp. 51–61, 2016, doi: 10.1016/j.biomaterials.2016.04.031.

[59] M. Bydon *et al.*, “CELLTOP Clinical Trial: First Report From a Phase 1 Trial of Autologous Adipose Tissue–Derived Mesenchymal Stem Cells in the Treatment of Paralysis Due to Traumatic Spinal Cord Injury,” *Mayo Clinic Proceedings*, vol. 95, no. 2, pp. 406–414, 2020, doi: 10.1016/j.mayocp.2019.10.008.

[60] K. A. Tran, P. P. Partyka, Y. Jin, J. Bouyer, I. Fischer, and P. A. Galie, “Vascularization of self-assembled peptide scaffolds for spinal cord injury repair,” *Acta Biomaterialia*, vol. 104, pp. 76–84, 2020, doi: 10.1016/j.actbio.2019.12.033.

[61] Y. C. Chen *et al.*, “Functional human vascular network generated in photocrosslinkable gelatin methacrylate hydrogels,” *Advanced Functional Materials*, vol. 22, no. 10, pp. 2027–2039, 2012, doi: 10.1002/adfm.201101662.

[62] M. Nakata, K. Nagasaka, M. Shimoda, I. Takashima, and S. Yamamoto, “Focal brain lesions induced with ultraviolet irradiation,” *Scientific Reports*, vol. 8, no. 1, pp. 1–11, 2018, doi: 10.1038/s41598-018-26117-w.

[63] J. Fu *et al.*, “Mechanical regulation of cell function with geometrically modulated elastomeric substrates,” *Nature Methods*, vol. 7, no. 9, pp. 733–736, 2010, doi: 10.1038/nmeth.1487.

[64] B. M. Baker and C. S. Chen, “Deconstructing the third dimension-how 3D culture microenvironments alter cellular cues,” *Journal of Cell Science*, vol. 125, no. 13, pp. 3015–3024, 2012, doi: 10.1242/jcs.079509.

[65] J. H. Wen *et al.*, “Interplay of matrix stiffness and protein tethering in stem cell differentiation,” *Nature Materials*, vol. 13, no. 10, pp. 979–987, 2014, doi: 10.1038/nmat4051.

[66] S. Dupont *et al.*, “Role of YAP/TAZ in mechanotransduction,” *Nature*, vol. 474, no. 7350, pp. 179–184, 2011, doi: 10.1038/nature10137.

[67] R. McBeath, D. M. Pirone, C. M. Nelson, K. Bhadriraju, and C. S. Chen, “Cell shape, cytoskeletal tension, and RhoA regulate stem cell lineage commitment,” *Developmental Cell*, vol. 6, no. 4, pp. 483–495, 2004, doi: 10.1016/S1534-5807(04)00075-9.

[68] H. Hong and J. P. Stegemann, “2D and 3D collagen and fibrin biopolymers promote specific ECM and integrin gene expression by vascular smooth muscle cells,” *Journal of Biomaterials Science, Polymer Edition*, vol. 19, no. 10, pp. 1279–1293, 2008, doi: 10.1163/156856208786052380.

[69] J. P. Stegemann and R. M. Nerem, “Altered response of vascular smooth muscle cells to exogenous biochemical stimulation in two- and three-dimensional culture,” *Experimental Cell Research*, vol. 283, no. 2, pp. 146–155, 2003, doi: 10.1016/S0014-4827(02)00041-1.

[70] S. Nam, J. Lee, D. G. Brownfield, and O. Chaudhuri, “Viscoplasticity Enables Mechanical Remodeling of Matrix by Cells,” *Biophysical Journal*, vol. 111, no. 10, pp. 2296–2308, 2016, doi: 10.1016/j.bpj.2016.10.002.

[71] O. Chaudhuri, “Viscoelastic hydrogels for 3D cell culture,” *Biomaterials Science*, vol. 5, no. 8, pp. 1480–1490, 2017, doi: 10.1039/c7bm00261k.

[72] O. Chaudhuri *et al.*, “Substrate stress relaxation regulates cell spreading,” *Nature Communications*, vol. 6, pp. 1–7, 2015, doi: 10.1038/ncomms7365.

[73] R. K. Das, V. Gocheva, R. Hammink, O. F. Zouani, and A. E. Rowan, “Stress-stiffening-mediated stem-cell commitment switch in soft responsive hydrogels,” *Nature Materials*, vol. 15, no. 3, pp. 318–325, 2016, doi: 10.1038/nmat4483.

[74] S. Khetan, M. Guvendiren, W. R. Legant, D. M. Cohen, C. S. Chen, and J. A. Burdick, "Degradation-mediated cellular traction directs stem cell fate in covalently crosslinked three-dimensional hydrogels," *Nature Materials*, vol. 12, no. 5, pp. 458–465, 2013, doi: 10.1038/nmat3586.

[75] R. S. Stowers, S. C. Allen, L. J. Suggs, and K. S. Anseth, "Dynamic phototuning of 3D hydrogel stiffness," *Proc Natl Acad Sci U S A*, vol. 112, no. 7, pp. 1953–1958, 2015, doi: 10.1073/pnas.1421897112.

[76] A. M. Rosales, S. L. Vega, F. W. DelRio, J. A. Burdick, and K. S. Anseth, "Hydrogels with Reversible Mechanics to Probe Dynamic Cell Microenvironments," *Angewandte Chemie - International Edition*, vol. 56, no. 40, pp. 12132–12136, 2017, doi: 10.1002/anie.201705684.

[77] C. Yang, M. W. Tibbitt, L. Basta, and K. S. Anseth, "Mechanical memory and dosing influence stem cell fate," *Nature Materials*, vol. 13, no. 6, pp. 645–652, 2014, doi: 10.1038/nmat3889.

[78] A. A. Abdeen, J. Lee, N. A. Bharadwaj, R. H. Ewoldt, and K. A. Kilian, "Temporal Modulation of Stem Cell Activity Using Magnetoactive Hydrogels," *Advanced Healthcare Materials*, vol. 5, no. 19, pp. 2536–2544, 2016, doi: 10.1002/adhm.201600349.

[79] T. Mitsumata, A. Honda, H. Kanazawa, and M. Kawai, "Magnetically tunable elasticity for magnetic hydrogels consisting of carrageenan and carbonyl iron particles," *Journal of Physical Chemistry B*, vol. 116, no. 40, pp. 12341–12348, 2012, doi: 10.1021/jp3049372.

[80] A. B. Bonhome-Espinosa *et al.*, "Effect of particle concentration on the microstructural and macromechanical properties of biocompatible magnetic hydrogels," *Soft Matter*, vol. 13, no. 16, pp. 2928–2941, 2017, doi: 10.1039/c7sm00388a.

[81] E. G. Popa, V. E. Santo, M. T. Rodrigues, and M. E. Gomes, "Magnetically-responsive hydrogels for modulation of chondrogenic commitment of human adipose-derived stem cells," *Polymers (Basel)*, vol. 8, no. 2, 2016, doi: 10.3390/polym8020028.

[82] J. H. Lee, W. J. Han, H. S. Jang, and H. J. Choi, "Highly Tough, Biocompatible, and Magneto-Responsive Fe3O4/Laponite/PDMAAm Nanocomposite Hydrogels," *Scientific Reports*, vol. 9, no. 1, pp. 1–13, 2019, doi: 10.1038/s41598-019-51555-5.

[83] M. Iwashita, N. Kataoka, K. Toida, and Y. Kosodo, “Systematic profiling of spatiotemporal tissue and cellular stiffness in the developing brain,” *Development*, vol. 141, no. 19, pp. 3793–3798, Oct. 2014, doi: 10.1242/dev.109637.

[84] B. S. Elkin, E. U. Azeloglu, K. D. Costa, and B. Morrison III, “Mechanical Heterogeneity of the Rat Hippocampus Measured by Atomic Force Microscope Indentation,” *Journal of Neurotrauma*, vol. 24, no. 5, pp. 812–822, May 2007, doi: 10.1089/neu.2006.0169.

[85] A. F. Christ *et al.*, “Mechanical difference between white and gray matter in the rat cerebellum measured by scanning force microscopy,” *Journal of Biomechanics*, vol. 43, no. 15, pp. 2986–2992, Nov. 2010, doi: 10.1016/j.jbiomech.2010.07.002.

[86] S. Chatelin, A. Constantinesco, and R. Willinger, “Fifty years of brain tissue mechanical testing: From in vitro to in vivo investigations,” *Biorheology*, vol. 47, no. 5–6, pp. 255–276, 2010, doi: 10.3233/BIR-2010-0576.

[87] S. Cheng, E. C. Clarke, and L. E. Bilston, “Rheological properties of the tissues of the central nervous system: A review,” *Medical Engineering & Physics*, vol. 30, no. 10, pp. 1318–1337, Dec. 2008, doi: 10.1016/j.medengphy.2008.06.003.

[88] A. di Ieva *et al.*, “Magnetic resonance elastography: a general overview of its current and future applications in brain imaging,” *Neurosurgical Review*, vol. 33, no. 2, pp. 137–145, Apr. 2010, doi: 10.1007/s10143-010-0249-6.

[89] Y. K. Mariappan, K. J. Glaser, and R. L. Ehman, “Magnetic resonance elastography: A review,” *Clinical Anatomy*, vol. 23, no. 5, pp. 497–511, Jun. 2010, doi: 10.1002/ca.21006.

[90] K. Ichihara, T. Taguchi, Y. Shimada, I. Sakuramoto, S. Kawano, and S. Kawai, “Gray Matter of the Bovine Cervical Spinal Cord is Mechanically More Rigid and Fragile than the White Matter,” *Journal of Neurotrauma*, vol. 18, no. 3, pp. 361–367, Mar. 2001, doi: 10.1089/08977150151071053.

[91] T.-K. Hung, G.-L. Chang, J.-L. Chang, and M. S. Albin, “Stress-strain relationship and neurological sequelae of uniaxial elongation of the spinal cord of cats,” *Surgical Neurology*, vol. 15, no. 6, pp. 471–476, Jun. 1981, doi: 10.1016/S0090-3019(81)80043-2.

[92] L. E. Bilston and L. E. Thibault, “The mechanical properties of the human cervical spinal cordIn Vitro,” *Annals of Biomedical Engineering*, vol. 24, no. S1, pp. 67–74, Sep. 1995, doi: 10.1007/BF02770996.

[93] P. S. Donoghue *et al.*, “The Development of a ε-Polycaprolactone Scaffold for Central Nervous System Repair,” *Tissue Engineering Part A*, vol. 19, no. 3–4, pp. 497–507, Feb. 2013, doi: 10.1089/ten.tea.2012.0382.

[94] D. Shahriari, J. Y. Koffler, M. H. Tuszynski, W. M. Campana, and J. S. Sakamoto, “Hierarchically Ordered Porous and High-Volume Polycaprolactone Microchannel Scaffolds Enhanced Axon Growth in Transected Spinal Cords,” *Tissue Engineering Part A*, vol. 23, no. 9–10, pp. 415–425, May 2017, doi: 10.1089/ten.tea.2016.0378.

[95] S. Zhang *et al.*, “Polycaprolactone/polysialic acid hybrid, multifunctional nanofiber scaffolds for treatment of spinal cord injury,” *Acta Biomaterialia*, vol. 77, pp. 15–27, Sep. 2018, doi: 10.1016/j.actbio.2018.06.038.

[96] X. Zhou *et al.*, “Polycaprolactone electrospun fiber scaffold loaded with iPSCs-NSCs and ASCs as a novel tissue engineering scaffold for the treatment of spinal cord injury,” *International Journal of Nanomedicine*, vol. Volume 13, pp. 6265–6277, Oct. 2018, doi: 10.2147/IJN.S175914.

[97] X. Zhang *et al.*, “A Perspective: Electrospun Fibers for Repairing Spinal Cord Injury,” *Chemical Research in Chinese Universities*, vol. 37, no. 3, pp. 404–410, Jun. 2021, doi: 10.1007/s40242-021-1162-y.

[98] K. Xi *et al.*, “Microenvironment-responsive immunoregulatory electrospun fibers for promoting nerve function recovery,” *Nature Communications*, vol. 11, no. 1, p. 4504, Dec. 2020, doi: 10.1038/s41467-020-18265-3.

[99] N. J. Schaub, C. D. Johnson, B. Cooper, and R. J. Gilbert, “Electrospun Fibers for Spinal Cord Injury Research and Regeneration,” *Journal of Neurotrauma*, vol. 33, no. 15, pp. 1405–1415, Aug. 2016, doi: 10.1089/neu.2015.4165.

[100] Z. Yu *et al.*, “Application of fibrin-based hydrogels for nerve protection and regeneration after spinal cord injury,” *Journal of Biological Engineering*, vol. 14, no. 1, p. 22, Dec. 2020, doi: 10.1186/s13036-020-00244-3.

[101] Z. Zhang *et al.*, “Effect of hierarchically aligned fibrin hydrogel in regeneration of spinal cord injury demonstrated by tractography: A pilot study,” *Scientific Reports*, vol. 7, no. 1, p. 40017, Feb. 2017, doi: 10.1038/srep40017.

[102] T. Sudhadevi, H. S. Vijayakumar, E. v Hariharan, S. Sandhyamani, and L. K. Krishnan, “Optimizing fibrin hydrogel toward effective neural progenitor cell delivery in spinal cord injury,” *Biomedical Materials*, vol. 17, no. 1, p. 014102, Jan. 2022, doi: 10.1088/1748-605X/ac3680.

[103] K. A. Tran *et al.*, “Magnetic alignment of injectable hydrogel scaffolds for spinal cord injury repair,” *Biomaterials Science*, 2022, doi: 10.1039/d1bm01590g.

[104] T. Nakahashi *et al.*, “Vascular endothelial cells synthesize and secrete brain-derived neurotrophic factor,” *FEBS Letters*, vol. 470, no. 2, pp. 113–117, 2000, doi: 10.1016/S0014-5793(00)01302-8.

[105] E. A. Kiyotake *et al.*, “Conductive and injectable hyaluronic acid/gelatin/gold nanorod hydrogels for enhanced surgical translation and bioprinting,” *Journal of Biomedical Materials Research Part A*, vol. 110, no. 2, pp. 365–382, Feb. 2022, doi: 10.1002/jbm.a.37294.

[106] D. Shahriari *et al.*, “Peripheral nerve growth within a hydrogel microchannel scaffold supported by a kink-resistant conduit,” *Journal of Biomedical Materials Research Part A*, vol. 105, no. 12, pp. 3392–3399, Dec. 2017, doi: 10.1002/jbm.a.36186.

[107] K. M. Pawelec, J. Koffler, D. Shahriari, A. Galvan, M. H. Tuszynski, and J. Sakamoto, “Microstructure and *in vivo* characterization of multi-channel nerve guidance scaffolds,” *Biomedical Materials*, vol. 13, no. 4, p. 044104, Apr. 2018, doi: 10.1088/1748-605X/aaad85.

[108] M. Costantini *et al.*, “Engineering Muscle Networks in 3D Gelatin Methacryloyl Hydrogels: Influence of Mechanical Stiffness and Geometrical Confinement,” *Frontiers in Bioengineering and Biotechnology*, vol. 5, Apr. 2017, doi: 10.3389/fbioe.2017.00022.

[109] J. Lewandowska-Łańcucka, K. Mystek, A. Mignon, S. van Vlierberghe, A. Łatkiewicz, and M. Nowakowska, “Alginate- and gelatin-based bioactive photocross-linkable hybrid materials for bone tissue engineering,” *Carbohydrate Polymers*, vol. 157, pp. 1714–1722, Feb. 2017, doi: 10.1016/j.carbpol.2016.11.051.

[110] M. T. Poldervaart *et al.*, “3D bioprinting of methacrylated hyaluronic acid (MeHA) hydrogel with intrinsic osteogenicity,” *PLOS ONE*, vol. 12, no. 6, p. e0177628, Jun. 2017, doi: 10.1371/journal.pone.0177628.

[111] Q. Feng *et al.*, “Mechanically resilient, injectable, and bioadhesive supramolecular gelatin hydrogels crosslinked by weak host-guest interactions assist cell infiltration and in situ tissue regeneration,” *Biomaterials*, vol. 101, pp. 217–228, Sep. 2016, doi: 10.1016/j.biomaterials.2016.05.043.

[112] X. Li *et al.*, “3D Culture of Chondrocytes in Gelatin Hydrogels with Different Stiffness,” *Polymers (Basel)*, vol. 8, no. 8, p. 269, Jul. 2016, doi: 10.3390/polym8080269.

[113] C. Chung, M. Beecham, R. L. Mauck, and J. A. Burdick, “The influence of degradation characteristics of hyaluronic acid hydrogels on in vitro neocartilage formation by mesenchymal stem cells,” *Biomaterials*, vol. 30, no. 26, pp. 4287–4296, Sep. 2009, doi: 10.1016/j.biomaterials.2009.04.040.

[114] I. E. Erickson, A. H. Huang, C. Chung, R. T. Li, J. A. Burdick, and R. L. Mauck, “Differential Maturation and Structure–Function Relationships in Mesenchymal Stem Cell- and Chondrocyte-Seeded Hydrogels,” *Tissue Engineering Part A*, vol. 15, no. 5, pp. 1041–1052, May 2009, doi: 10.1089/ten.tea.2008.0099.

[115] S. J. Bryant and K. S. Anseth, “The effects of scaffold thickness on tissue engineered cartilage in photocrosslinked poly(ethylene oxide) hydrogels,” *Biomaterials*, vol. 22, no. 6, pp. 619–626, Mar. 2001, doi: 10.1016/S0142-9612(00)00225-8.

[116] H. Li, A. M. Koenig, P. Sloan, and N. D. Leipzig, “In vivo assessment of guided neural stem cell differentiation in growth factor immobilized chitosan-based hydrogel scaffolds,” *Biomaterials*, vol. 35, no. 33, pp. 9049–9057, Nov. 2014, doi: 10.1016/j.biomaterials.2014.07.038.

[117] N. D. Leipzig, R. G. Wylie, H. Kim, and M. S. Shoichet, “Differentiation of neural stem cells in three-dimensional growth factor-immobilized chitosan hydrogel scaffolds,” *Biomaterials*, vol. 32, no. 1, pp. 57–64, Jan. 2011, doi: 10.1016/j.biomaterials.2010.09.031.

[118] I. S. Kinstlinger and J. S. Miller, “3D-printed fluidic networks as vasculature for engineered tissue,” *Lab on a Chip*, vol. 16, no. 11, pp. 2025–2043, 2016, doi: 10.1039/C6LC00193A.

[119] S. R. Gorodkin, R. O. James, and W. I. Kordonski, “Magnetic properties of carbonyl iron particles in magnetorheological fluids,” *Journal of Physics: Conference Series*, vol. 149, p. 012051, Feb. 2009, doi: 10.1088/1742-6596/149/1/012051.

[120] D. P. Ankeny, D. M. McTigue, and L. B. Jakeman, “Bone marrow transplants provide tissue protection and directional guidance for axons after contusive spinal cord injury in rats,” *Experimental Neurology*, vol. 190, no. 1, pp. 17–31, 2004, doi: 10.1016/j.expneurol.2004.05.045.

[121] C. P. Hofstetter *et al.*, “Marrow stromal cells form guiding strands in the injured spinal cord and promote recovery,” *Proceedings of the National Academy of Sciences*, vol. 99, no. 4, pp. 2199–2204, 2002, doi: 10.1073/pnas.042678299.

[122] C. C. Medalha, Y. Jin, T. Yamagami, C. Haas, and I. Fischer, “Transplanting neural progenitors into a complete transection model of spinal cord injury,” *Journal of Neuroscience Research*, vol. 92, no. 5, pp. 607–618, 2014, doi: 10.1002/jnr.23340.

[123] E. K. F. Yim, R. M. Reano, S. W. Pang, A. F. Yee, C. S. Chen, and K. W. Leong, "Nanopattern-induced changes in morphology and motility of smooth muscle cells," *Biomaterials*, vol. 26, no. 26, pp. 5405–5413, 2005, doi: 10.1016/j.biomaterials.2005.01.058.

[124] P. P. Partyka *et al.*, "Mechanical stress regulates transport in a compliant 3D model of the blood-brain barrier," *Biomaterials*, vol. 115, pp. 30–39, 2017, doi: 10.1016/j.biomaterials.2016.11.012.

[125] H. C. Bowers, M. L. Fiori, J. B. Khadela, P. A. Janmey, and P. A. Galie, "Cell-matrix tension contributes to hypoxia in astrocyte-seeded viscoelastic hydrogels composed of collagen and hyaluronan," *Experimental Cell Research*, vol. 376, no. 1, pp. 49–57, 2019, doi: 10.1016/j.yexcr.2019.01.012.

[126] A. L. Placone, P. M. McGuiggan, D. E. Bergles, H. Guerrero-Cazares, A. Quiñones-Hinojosa, and P. C. Searson, "Human astrocytes develop physiological morphology and remain quiescent in a novel 3D matrix," *Biomaterials*, vol. 42, pp. 134–143, 2015, doi: 10.1016/j.biomaterials.2014.11.046.

[127] P. A. Galie, D.-H. T. Nguyen, C. K. Choi, D. M. Cohen, P. A. Janmey, and C. S. Chen, "Fluid shear stress threshold regulates angiogenic sprouting," *Proceedings of the National Academy of Sciences*, vol. 111, no. 22, pp. 7968–7973, 2014, doi: 10.1073/pnas.1310842111.

[128] N. Bouhrira, B. J. Deore, D. W. Sazer, Z. Chiaradia, J. S. Miller, and P. A. Galie, "Disturbed flow disrupts the blood-brain barrier in a 3D bifurcation model," *Biofabrication*, vol. 12, no. 2, 2020, doi: 10.1088/1758-5090/ab5898.

[129] S. R. Caliari, S. L. Vega, M. Kwon, E. M. Soulas, and J. A. Burdick, "Dimensionality and spreading influence MSC YAP/TAZ signaling in hydrogel environments," *Biomaterials*, vol. 103, pp. 314–323, 2016, doi: 10.1016/j.biomaterials.2016.06.061.

[130] D. E. Koser, E. Moeendarbary, J. Hanne, S. Kuerten, and K. Franze, "CNS Cell Distribution and Axon Orientation Determine Local Spinal Cord Mechanical Properties," *Biophysical Journal*, vol. 108, no. 9, pp. 2137–2147, May 2015, doi: 10.1016/j.bpj.2015.03.039.

[131] P. Mitra and R. M. Brownstone, "An in vitro spinal cord slice preparation for recording from lumbar motoneurons of the adult mouse," *Journal of Neurophysiology*, vol. 107, no. 2, pp. 728–741, Jan. 2012, doi: 10.1152/jn.00558.2011.

[132] M. GRIFFIN, R. CASADIO, and C. M. BERGAMINI, “Transglutaminases: Nature’s biological glues,” *Biochemical Journal*, vol. 368, no. 2, pp. 377–396, Dec. 2002, doi: 10.1042/bj20021234.

[133] V. van Duinen, D. Zhu, C. Ramakers, A. J. van Zonneveld, P. Vulto, and T. Hankemeier, “Perfused 3D angiogenic sprouting in a high-throughput in vitro platform,” *Angiogenesis*, vol. 22, no. 1, pp. 157–165, 2019, doi: 10.1007/s10456-018-9647-0.

[134] F. Lauwers, F. Cassot, V. Lauwers-Cances, P. Puwanarajah, and H. Duvernoy, “Morphometry of the human cerebral cortex microcirculation: General characteristics and space-related profiles,” *Neuroimage*, vol. 39, no. 3, pp. 936–948, 2008, doi: 10.1016/j.neuroimage.2007.09.024.

[135] W. Meier-Ruge, O. Hunziker, U. Schulz, H. J. Tobler, and A. Schweizer, “Stereological changes in the capillary network and nerve cells of the aging human brain,” *Mechanisms of Ageing and Development*, vol. 14, no. 1–2, pp. 233–243, 1980, doi: 10.1016/0047-6374(80)90123-2.

[136] Y. Cao *et al.*, “Three-dimensional imaging of microvasculature in the rat spinal cord following injury,” *Scientific Reports*, vol. 5, pp. 1–11, 2015, doi: 10.1038/srep12643.

[137] Y. Jin *et al.*, “Transplantation of human glial restricted progenitors and derived astrocytes into a contusion model of spinal cord injury,” *Journal of Neurotrauma*, vol. 28, no. 4, pp. 579–594, 2011, doi: 10.1089/neu.2010.1626.

[138] Y. Jin, J. S. Shumsky, and I. Fischer, “Axonal regeneration of different tracts following transplants of human glial restricted progenitors into the injured spinal cord in rats,” *Brain Research*, vol. 1686, pp. 101–112, 2018, doi: 10.1016/j.brainres.2018.01.030.

[139] Y. il Cho, J. S. Choi, S. Y. Jeong, and H. S. Yoo, “Nerve growth factor (NGF)-conjugated electrospun nanostructures with topographical cues for neuronal differentiation of mesenchymal stem cells,” *Acta Biomaterialia*, vol. 6, no. 12, pp. 4725–4733, 2010, doi: 10.1016/j.actbio.2010.06.019.

[140] X. Q. Li, V. M. K. Verge, J. M. Johnston, and D. W. Zochodne, “CGRP peptide and regenerating sensory axons,” *Journal of Neuropathology and Experimental Neurology*, vol. 63, no. 10, pp. 1092–1103, 2004, doi: 10.1093/jnen/63.10.1092.

[141] M. Ghosh and D. D. Pearse, “The role of the serotonergic system in locomotor recovery after spinal cord injury,” *Frontiers in Neural Circuits*, vol. 8, no. FEB, pp. 1–14, 2015, doi: 10.3389/fncir.2014.00151.

[142] R. Curtis, D. Green, R. M. Lindsay, and G. P. Wilkin, “Up-regulation of GAP-43 and growth of axons in rat spinal cord after compression injury,” *Journal of Neurocytology*, vol. 22, no. 1, pp. 51–64, 1993, doi: 10.1007/BF01183975.

[143] T. Shiga, A. Okada, and T. Kurauchi, “Magnetroviscoelastic behavior of composite gels,” *Journal of Applied Polymer Science*, vol. 58, no. 4, pp. 787–792, 1995, doi: 10.1002/app.1995.070580411.

[144] G. L. and T. L. Yangguang Xu, “Magneto-Sensitive Smart Materials and Magnetorheological Mechanism,” *IntechOpen,*, doi: DOI: http://dx.doi.org/10.5772/intechopen.84742.

[145] L. D. Landau, L. P. Pitaevskii, and E. M. Lifshitz, *Electrodynamics of Continuous Media*, vol. 29, no. 9. 1984. doi: 10.1119/1.1937882.

[146] Y. M. Shkel and D. J. Klingenberg, “Electrostriction of polarizable materials: Comparison of models with experimental data,” *Journal of Applied Physics*, vol. 83, no. 12, pp. 7834–7843, 1998, doi: 10.1063/1.367958.

[147] A. Basu, Q. Wen, X. Mao, T. C. Lubensky, P. A. Janmey, and A. G. Yodh, “Nonaffine displacements in flexible polymer networks,” *Macromolecules*, vol. 44, no. 6, pp. 1671–1679, 2011, doi: 10.1021/ma1026803.

[148] Q. Wen, A. Basu, J. P. Winer, A. Yodh, and P. A. Janmey, “Local and global deformations in a strain-stiffening fibrin gel,” *New Journal of Physics*, vol. 9, 2007, doi: 10.1088/1367-2630/9/11/428.

[149] A. Shkumatov *et al.*, “Matrix stiffness-modulated proliferation and secretory function of the airway smooth muscle cells,” *American Journal of Physiology - Lung Cellular and Molecular Physiology*, vol. 308, no. 11, pp. L1125–L1135, 2015, doi: 10.1152/ajplung.00154.2014.

[150] M. Wang *et al.*, “Regulating Mechanotransduction in Three Dimensions using Sub-Cellular Scale, Crosslinkable Fibers of Controlled Diameter, Stiffness, and Alignment,” *Advanced Functional Materials*, vol. 29, no. 18, pp. 1–11, 2019, doi: 10.1002/adfm.201808967.

[151] C. Godbout *et al.*, “The Mechanical Environment Modulates Intracellular Calcium Oscillation Activities of Myofibroblasts,” *PLoS ONE*, vol. 8, no. 5, 2013, doi: 10.1371/journal.pone.0064560.

[152] O. Chaudhuri *et al.*, “Hydrogels with tunable stress relaxation regulate stem cell fate and activity,” *Nature Materials*, vol. 15, no. 3, pp. 326–334, 2016, doi: 10.1038/nmat4489.

[153] L. Bian, C. Hou, E. Tous, R. Rai, R. L. Mauck, and J. A. Burdick, “The influence of hyaluronic acid hydrogel crosslinking density and macromolecular diffusivity on human MSC chondrogenesis and hypertrophy,” *Biomaterials*, vol. 34, no. 2, pp. 413–421, 2013, doi: 10.1016/j.biomaterials.2012.09.052.

[154] O. Chaudhuri *et al.*, “Hydrogels with tunable stress relaxation regulate stem cell fate and activity,” *Nature Materials*, vol. 15, no. 3, pp. 326–334, 2016, doi: 10.1038/nmat4489.

[155] K. Pogoda *et al.*, “Compression stiffening of brain and its effect on mechanosensing by glioma cells,” *New Journal of Physics*, vol. 16, no. 7, p. 075002, Jul. 2014, doi: 10.1088/1367-2630/16/7/075002.

[156] M. Perepelyuk *et al.*, “Normal and Fibrotic Rat Livers Demonstrate Shear Strain Softening and Compression Stiffening: A Model for Soft Tissue Mechanics,” *PLOS ONE*, vol. 11, no. 1, p. e0146588, Jan. 2016, doi: 10.1371/journal.pone.0146588.

[157] C. Puckert, E. Tomaskovic-Crook, S. Gambhir, G. G. Wallace, J. M. Crook, and M. J. Higgins, “Electro-mechano responsive properties of gelatin methacrylate (GelMA) hydrogel on conducting polymer electrodes quantified using atomic force microscopy,” *Soft Matter*, vol. 13, no. 27, pp. 4761–4772, 2017, doi: 10.1039/C7SM00335H.

[158] F. Moradi *et al.*, “BD PuraMatrix peptide hydrogel as a culture system for human fetal Schwann cells in spinal cord regeneration,” *Journal of Neuroscience Research*, vol. 90, no. 12, pp. 2335–2348, 2012, doi: 10.1002/jnr.23120.

[159] T. E. Park *et al.*, “Hypoxia-enhanced Blood-Brain Barrier Chip recapitulates human barrier function and shuttling of drugs and antibodies,” *Nature Communications*, vol. 10, no. 1, pp. 1–12, 2019, doi: 10.1038/s41467-019-10588-0.

[160] E. K. Hollmann, A. K. Bailey, A. v. Potharazu, M. D. Neely, A. B. Bowman, and E. S. Lippmann, “Accelerated differentiation of human induced pluripotent stem cells to blood-brain barrier endothelial cells,” *Fluids and Barriers of the CNS*, vol. 14, no. 1, pp. 1–13, 2017, doi: 10.1186/s12987-017-0059-0.

[161] E. J. Bradbury and L. M. Carter, “Manipulating the glial scar: Chondroitinase ABC as a therapy for spinal cord injury,” *Brain Research Bulletin*, vol. 84, no. 4–5, pp. 306–316, 2011, doi: 10.1016/j.brainresbull.2010.06.015.

[162] C. Fan *et al.*, “A modified collagen scaffold facilitates endogenous neurogenesis for acute spinal cord injury repair,” *Acta Biomaterialia*, vol. 51, pp. 304–316, 2017, doi: 10.1016/j.actbio.2017.01.009.

[163] X. Li *et al.*, “Cetuximab modified collagen scaffold directs neurogenesis of injury-activated endogenous neural stem cells for acute spinal cord injury repair,” *Biomaterials*, vol. 137, pp. 73–86, 2017, doi: 10.1016/j.biomaterials.2017.05.027.

[164] W. Liu *et al.*, “A functional scaffold to promote the migration and neuronal differentiation of neural stem/progenitor cells for spinal cord injury repair,” *Biomaterials*, vol. 243, no. February, p. 119941, 2020, doi: 10.1016/j.biomaterials.2020.119941.

[165] E. M. Fleischmann, “The measurement and penetration of ultraviolet radiation into tropical marine water,” *Limnology and Oceanography*, vol. 34, no. 8, pp. 1623–1629, 1989, doi: 10.4319/lo.1989.34.8.1623.

[166] M. Yasui and K. Ikuta, “Modeling and measurement of curing properties of photocurable polymer containing magnetic particles and microcapsules,” *Microsystems and Nanoengineering*, vol. 3, 2017, doi: 10.1038/micronano.2017.35.

[167] J. Ikeda, D. Takahashi, M. Watanabe, M. Kawai, and T. Mitsumata, “Particle size in secondary particle and magnetic response for carrageenan magnetic hydrogels,” *Gels*, vol. 5, no. 3, pp. 1–9, 2019, doi: 10.3390/gels5030039.

[168] C. Gila-Vilchez, J. D. G. Duran, F. Gonzalez-Caballero, A. Zubarev, and M. T. Lopez-Lopez, “Magnetorheology of alginate ferrogels,” *Smart Materials and Structures*, vol. 28, no. 3, 2019, doi: 10.1088/1361-665X/aafeac.

[169] W. H. Binder and R. Sachsenhofer, “‘Click’ chemistry in polymer and materials science,” *Macromolecular Rapid Communications*, vol. 28, no. 1, pp. 15–54, 2007, doi: 10.1002/marc.200600625.

[170] C. E. Hoyle and C. N. Bowman, “Thiol-ene click chemistry,” *Angewandte Chemie - International Edition*, vol. 49, no. 9, pp. 1540–1573, 2010, doi: 10.1002/anie.200903924.

[171] E. M. Shapiro, K. Sharer, S. Skrtic, and A. P. Koretsky, “In vivo detection of single cells by MRI,” *Magnetic Resonance in Medicine*, vol. 55, no. 2, pp. 242–249, 2006, doi: 10.1002/mrm.20718.

[172] C. Suezawa *et al.*, “Time-dependent changes in plasma osteopontin levels in patients with anterior-wall acute myocardial infarction after successful reperfusion: Correlation with left-ventricular volume and function,” *Journal of Laboratory and Clinical Medicine*, vol. 145, no. 1, pp. 33–40, 2005, doi: 10.1016/j.lab.2004.08.007.

[173] J. M. Pilewski, L. Liu, A. C. Henry, A. v. Knauer, and C. A. Feghali-Bostwick, “Insulin-like growth factor binding proteins 3 and 5 are overexpressed in idiopathic

pulmonary fibrosis and contribute to extracellular matrix deposition," *American Journal of Pathology*, vol. 166, no. 2, pp. 399–407, 2005, doi: 10.1016/S0002-9440(10)62263-8.

[174] P. A. Galie, N. Khalid, K. E. Carnahan, M. v. Westfall, and J. P. Stegemann, "Substrate stiffness affects sarcomere and costamere structure and electrophysiological function of isolated adult cardiomyocytes," *Cardiovascular Pathology*, vol. 22, no. 3, pp. 219–227, 2013, doi: 10.1016/j.carpath.2012.10.003.

[175] P. G. Genever, W. J. Cunliffe, and E. J. Wood, "Influence of the extracellular matrix on fibroblast responsiveness to phenytoin using in vitro wound healing models," *British Journal of Dermatology*, vol. 133, no. 2, pp. 231–235, 1995, doi: 10.1111/j.1365-2133.1995.tb02620.x.

[176] L. E. Tracy, R. A. Minasian, and E. J. Caterson, "Extracellular Matrix and Dermal Fibroblast Function in the Healing Wound," *Advances in Wound Care*, vol. 5, no. 3, pp. 119–136, 2016, doi: 10.1089/wound.2014.0561.

[177] P. A. Netti, L. T. Baxter, Y. Boucher, R. K. Jain, and R. Skalak, "Time-dependent Behavior of Interstitial Fluid Pressure in Solid Tumors: Implications for Drug Delivery," *Cancer Research*, vol. 55, no. 22, pp. 5451–5458, 1995.

[178] F. Yuan, Y. Chen, M. Dellian, N. Safabakhsh, N. Ferrara, and R. K. Jain, "Time-dependent vascular regression and permeability changes in established human tumor xenografts induced by an anti-vascular endothelial growth factor/vascular permeability factor antibody," *Proc Natl Acad Sci U S A*, vol. 93, no. 25, pp. 14765–14770, 1996, doi: 10.1073/pnas.93.25.14765.

[179] M. Ponticos and B. D. Smith, "Extracellular matrix synthesis in vascular disease: Hypertension, and atherosclerosis," *Journal of Biomedical Research*, vol. 28, no. 1, pp. 25–39, 2014, doi: 10.7555/JBR.27.20130064.

[180] F. G. Spinale, M. L. Coker, C. v. Thomas, J. D. Walker, R. Mukherjee, and L. Hebbar, "Time-dependent changes in matrix metalloproteinase activity and expression during the progression of congestive heart failure: Relation to ventricular and myocyte function," *Circulation Research*, vol. 82, no. 4, pp. 482–495, 1998, doi: 10.1161/01.RES.82.4.482.

[181] A. Shellard and R. Mayor, "Collective durotaxis along a self-generated stiffness gradient in vivo," *Nature*, vol. 600, no. 7890, pp. 690–694, Dec. 2021, doi: 10.1038/s41586-021-04210-x.

[182] I. Pi-Jaumà, R. Alert, and J. Casademunt, “Collective durotaxis of cohesive cell clusters on a stiffness gradient,” *The European Physical Journal E*, vol. 45, no. 1, p. 7, Jan. 2022, doi: 10.1140/epje/s10189-021-00150-6.

[183] C. F. Guimarães, L. Gasperini, A. P. Marques, and R. L. Reis, “The stiffness of living tissues and its implications for tissue engineering,” *Nature Reviews Materials*, vol. 5, no. 5, pp. 351–370, May 2020, doi: 10.1038/s41578-019-0169-1.

[184] C. D. Hartman, B. C. Isenberg, S. G. Chua, and J. Y. Wong, “Vascular smooth muscle cell durotaxis depends on extracellular matrix composition,” *Proceedings of the National Academy of Sciences*, vol. 113, no. 40, pp. 11190–11195, Oct. 2016, doi: 10.1073/pnas.1611324113.

[185] J. A. Espina, C. L. Marchant, and E. H. Barriga, “Durotaxis: the mechanical control of directed cell migration,” *The FEBS Journal*, vol. 289, no. 10, pp. 2736–2754, May 2022, doi: 10.1111/febs.15862.

[186] B. J. DeOre, P. P. Partyka, F. Fan, and P. A. Galie, “CD44 mediates shear stress mechanotransduction in an in vitro blood-brain barrier model through small GTPases RhoA and Rac1,” *The FASEB Journal*, vol. 36, no. 5, May 2022, doi: 10.1096/fj.202100822RR.

[187] B. J. DeOre *et al.*, “Microindentation of Fluid-Filled Cellular Domes Reveals the Contribution of RhoA-ROCK Signaling to Multicellular Mechanics,” *Small*, vol. 18, no. 21, p. 2200883, May 2022, doi: 10.1002/smll.202200883.

[188] B. J. DeOre, K. A. Tran, A. M. Andrews, S. H. Ramirez, and P. A. Galie, “SARS-CoV-2 Spike Protein Disrupts Blood–Brain Barrier Integrity via RhoA Activation,” *Journal of Neuroimmune Pharmacology*, vol. 16, no. 4, pp. 722–728, Dec. 2021, doi: 10.1007/s11481-021-10029-0.

[189] L. A. Hockaday *et al.*, “Rapid 3D printing of anatomically accurate and mechanically heterogeneous aortic valve hydrogel scaffolds,” *Biofabrication*, vol. 4, no. 3, p. 035005, Sep. 2012, doi: 10.1088/1758-5082/4/3/035005.

[190] A. Thomas *et al.*, “Vascular bioprinting with enzymatically degradable bioinks via multi-material projection-based stereolithography,” *Acta Biomaterialia*, vol. 117, pp. 121–132, Nov. 2020, doi: 10.1016/j.actbio.2020.09.033.

[191] J. de Vicente, M. T. López-López, F. González-Caballero, and J. D. G. Durán, “Rheological study of the stabilization of magnetizable colloidal suspensions by addition of silica nanoparticles,” *Journal of Rheology*, vol. 47, no. 5, pp. 1093–1109, Sep. 2003, doi: 10.1122/1.1595094.

[192] N. H. Hai, N. H. Luong, N. Chau, and N. Q. Tai, “Preparation of magnetic nanoparticles embedded in polystyrene microspheres,” *Journal of Physics: Conference Series*, vol. 187, p. 012009, Sep. 2009, doi: 10.1088/1742-6596/187/1/012009.

[193] R. R. Smith *et al.*, “The Louisville Swim Scale: A Novel Assessment of Hindlimb Function following Spinal Cord Injury in Adult Rats,” *Journal of Neurotrauma*, vol. 23, no. 11, pp. 1654–1670, Nov. 2006, doi: 10.1089/neu.2006.23.1654.

[194] C. Rink and S. Khanna, “Significance of brain tissue oxygenation and the arachidonic acid cascade in stroke,” *Antioxidants and Redox Signaling*, vol. 14, no. 10, pp. 1889–1903, 2011, doi: 10.1089/ars.2010.3474.

[195] M. E. Watts, R. Pocock, and C. Claudianos, “Brain energy and oxygen metabolism: Emerging role in normal function and disease,” *Frontiers in Molecular Neuroscience*, vol. 11, 2018, doi: 10.3389/fnmol.2018.00216.

[196] S. Caja and J. A. Enríquez, “Mitochondria in endothelial cells: Sensors and integrators of environmental cues,” *Redox Biology*, vol. 12, pp. 821–827, 2017, doi: 10.1016/j.redox.2017.04.021.

[197] B. Yetkin-Arik *et al.*, “The role of glycolysis and mitochondrial respiration in the formation and functioning of endothelial tip cells during angiogenesis,” *Scientific Reports*, vol. 9, no. 1, 2019, doi: 10.1038/s41598-019-48676-2.

[198] S. K. Halder and R. Milner, “Mild hypoxia triggers transient blood–brain barrier disruption: a fundamental protective role for microglia,” *Acta Neuropathologica Communications*, vol. 8, no. 1, 2020, doi: 10.1186/s40478-020-01051-z.

[199] M. M. Hickey and M. C. Simon, “Regulation of Angiogenesis by Hypoxia and Hypoxia-Inducible Factors,” *Current Topics in Developmental Biology*, vol. 76, pp. 217–257, 2006, doi: 10.1016/S0070-2153(06)76007-0.

[200] A. Doddaballapur *et al.*, “Laminar shear stress inhibits endothelial cell metabolism via KLF2-mediated repression of PFKFB3,” *Arteriosclerosis, Thrombosis, and Vascular Biology*, vol. 35, no. 1, pp. 137–145, 2015, doi: 10.1161/ATVBAHA.114.304277.

[201] G. Niu and X. Chen, “Vascular Endothelial Growth Factor as an Anti-Angiogenic Target for Cancer Therapy,” *Current Drug Targets*, vol. 11, no. 8, pp. 1000–1017, 2010, doi: 10.2174/138945010791591395.

[202] P. M. Clifford *et al.*, “Aβ peptides can enter the brain through a defective blood-brain barrier and bind selectively to neurons,” *Brain Research*, vol. 1142, no. 1, pp. 223–236, 2007, doi: 10.1016/j.brainres.2007.01.070.

[203] R. A. Umans *et al.*, “CNS angiogenesis and barriergenesis occur simultaneously,” *Developmental Biology*, vol. 425, no. 2, pp. 101–108, 2017, doi: 10.1016/j.ydbio.2017.03.017.

[204] D. H. T. Nguyen *et al.*, “Biomimetic model to reconstitute angiogenic sprouting morphogenesis in vitro,” *Proc Natl Acad Sci U S A*, vol. 110, no. 17, pp. 6712–6717, 2013, doi: 10.1073/pnas.1221526110.

[205] D. H. T. Nguyen, L. Gao, A. Wong, and C. S. Chen, “Cdc42 regulates branching in angiogenic sprouting in vitro,” *Microcirculation*, vol. 24, no. 5, 2017, doi: 10.1111/micc.12372.

[206] S. Kim, M. Chung, J. Ahn, S. Lee, and N. L. Jeon, “Interstitial flow regulates the angiogenic response and phenotype of endothelial cells in a 3D culture model,” *Lab on a Chip*, vol. 16, no. 21, pp. 4189–4199, 2016, doi: 10.1039/c6lc00910g.

[207] J. W. Song, J. Daubriac, J. M. Tse, D. Bazou, and L. L. Munn, “RhoA mediates flow-induced endothelial sprouting in a 3-D tissue analogue of angiogenesis,” *Lab on a Chip*, vol. 12, no. 23, pp. 5000–5006, 2012, doi: 10.1039/c2lc40389g.

[208] M. A. Winkelman, D. Y. Kim, S. Kakarla, A. Grath, N. Silvia, and G. Dai, “Interstitial flow enhances the formation, connectivity, and function of 3D brain microvascular networks generated within a microfluidic device,” *Lab on a Chip*, vol. 22, no. 1, pp. 170–192, 2022, doi: 10.1039/d1lc00605c.

[209] W. J. Polacheck, M. L. Kutys, J. B. Tefft, and C. S. Chen, “Microfabricated blood vessels for modeling the vascular transport barrier,” *Nature Protocols*, vol. 14, no. 5, pp. 1425–1454, 2019, doi: 10.1038/s41596-019-0144-8.

[210] G. Lee *et al.*, “Multilayer microfluidic platform for the study of luminal, transmural, and interstitial flow,” *Biofabrication*, vol. 14, no. 2, p. 025007, 2022, doi: 10.1088/1758-5090/ac48e5.

[211] W. Y. Wang *et al.*, “Direct comparison of angiogenesis in natural and synthetic biomaterials reveals that matrix porosity regulates endothelial cell invasion speed and sprout diameter,” *Acta Biomaterialia*, vol. 135, pp. 260–273, 2021, doi: 10.1016/j.actbio.2021.08.038.

[212] W. Y. Wang, E. H. Jarman, D. Lin, and B. M. Baker, “Dynamic Endothelial Stalk Cell–Matrix Interactions Regulate Angiogenic Sprout Diameter,” *Frontiers in Bioengineering and Biotechnology*, vol. 9, 2021, doi: 10.3389/fbioe.2021.620128.

[213] P. A. Williams, R. S. Stilhano, V. P. To, L. Tran, K. Wong, and E. A. Silva, “Hypoxia augments outgrowth endothelial cell (OEC) sprouting and directed migration in response to sphingosine-1-phosphate (S1P),” *PLoS ONE*, vol. 10, no. 4, 2015, doi: 10.1371/journal.pone.0123437.

[214] G. Vilanova, M. Burés, I. Colominas, and H. Gomez, “Computational modelling suggests complex interactions between interstitial flow and tumour angiogenesis,” *Journal of the Royal Society Interface*, vol. 15, no. 146, 2018, doi: 10.1098/rsif.2018.0415.

[215] J. P. Alberding and T. W. Secomb, “Simulation of angiogenesis in three dimensions: Application to cerebral cortex,” *PLoS Computational Biology*, vol. 17, no. 6, 2021, doi: 10.1371/journal.pcbi.1009164.

[216] D. A. Hormuth *et al.*, “Biologically-based mathematical modeling of tumor vasculature and angiogenesis via time-resolved imaging data,” *Cancers (Basel)*, vol. 13, no. 12, 2021, doi: 10.3390/cancers13123008.

[217] M. Azimzadeh, P. Khashayar, M. Amereh, N. Tasnim, M. Hoorfar, and M. Akbari, “Microfluidic-Based Oxygen (O2) Sensors for On-Chip Monitoring of Cell, Tissue and Organ Metabolism,” *Biosensors (Basel)*, vol. 12, no. 1, p. 6, 2021, doi: 10.3390/bios12010006.

[218] C. McDonald, L. Drewes, and Z. Blankenheim, “Brain Endothelial Cell Bioenergetics via Extracellular Flux Analysis,” *The FASEB Journal*, vol. 33, no. S1, 2019, doi: 10.1096/fasebj.2019.33.1_supplement.708.1.

[219] M. H. Sheikh *et al.*, “Immuno-metabolic impact of the multiple sclerosis patients’ sera on endothelial cells of the blood-brain barrier,” *Journal of Neuroinflammation*, vol. 17, no. 1, 2020, doi: 10.1186/s12974-020-01810-8.

[220] S. L. Rellick, H. Hu, J. W. Simpkins, and X. Ren, “Evaluation of bioenergetic function in cerebral vascular endothelial cells,” *Journal of Visualized Experiments*, vol. 2016, no. 117, 2016, doi: 10.3791/54847.

[221] P. A. Galie, F. J. Byfield, C. S. Chen, J. Y. Kresh, and P. A. Janmey, “Mechanically stimulated contraction of engineered cardiac constructs using a microcantilever,” *IEEE Transactions on Biomedical Engineering*, vol. 62, no. 2, pp. 438–442, 2015, doi: 10.1109/TBME.2014.2357778.

[222] B. B. Weksler, “Blood-brain barrier-specific properties of a human adult brain endothelial cell line,” *The FASEB Journal*, vol. 26, pp. 1–26, 2005, doi: 10.1096/fj.04-3458fje.

[223] R. H. ADAMSON, J. F. LENZ, and F. E. CURRY, “Quantitative Laser Scanning Confocal Microscopy on Single Capillaries: Permeability Measurement,” *Microcirculation*, vol. 1, no. 4, pp. 251–265, 1994, doi: 10.3109/10739689409146752.

[224] U. Cheema, Z. Rong, O. Kirresh, A. J. MacRobert, P. Vadgama, and R. A. Brown, “Oxygen diffusion through collagen scaffolds at defined densities: implications for cell survival in tissue models,” *Journal of Tissue Engineering and Regenerative Medicine*, vol. 6, no. 1, pp. 77–84, Jan. 2012, doi: 10.1002/term.402.

[225] N. D. Bade, R. D. Kamien, R. K. Assoian, and K. J. Stebe, “Curvature and Rho activation differentially control the alignment of cells and stress fibers,” *Science Advances*, vol. 3, no. 9, 2017, doi: 10.1126/sciadv.1700150.

[226] P. A. Galie, M. W. Russell, M. V. Westfall, and J. P. Stegemann, “Interstitial fluid flow and cyclic strain differentially regulate cardiac fibroblast activation via AT1R and TGF-β1,” *Experimental Cell Research*, vol. 318, no. 1, pp. 75–84, Jan. 2012, doi: 10.1016/j.yexcr.2011.10.008.

[227] B. J. Moeller, Y. Cao, Z. Vujaskovic, C. Y. Li, Z. A. Haroon, and M. W. Dewhirst, “The relationship between hypoxia and angiogenesis,” *Seminars in Radiation Oncology*, vol. 14, no. 3, pp. 215–221, 2004, doi: 10.1016/j.semradonc.2004.04.005.

[228] A. J. Moss, “Intramyocardial oxygen tension,” *Cardiovascular Research*, vol. 2, no. 3, pp. 314–318, 1968, doi: 10.1093/cvr/2.3.314.

[229] L. B. Padnick, R. A. Linsenmeier, and T. K. Goldstick, “Oxygenation of the cat primary visual cortex,” *Journal of Applied Physiology*, vol. 86, no. 5, pp. 1490–1496, 1999, doi: 10.1152/jappl.1999.86.5.1490.

Appendix

Oxygen Gradients Dictate Angiogenesis But Not Barriergenesis in a 3D Brain Microvascular Model

Abstract

A variety of biophysical properties are known to regulate angiogenic sprouting, and *in vitro* systems can parse the individual effects of these factors in a controlled setting. Here, a three-dimensional brain microvascular model interrogates how variables including extracellular matrix composition, fluid shear stress, and radius of curvature affect angiogenic sprouting of cerebral endothelial cells. Tracking endothelial migration over several days reveals that application of fluid shear stress and enlarged vessel radius of curvature both attenuate sprouting. Computational modeling informed by oxygen consumption assays suggests that sprouting correlates to reduced oxygen concentration: both fluid shear stress and vessel geometry alter the local oxygen levels dictated by both ambient conditions and cellular respiration. Moreover, increasing cell density and consequently lowering the local oxygen levels yields significantly more sprouting. Further analysis reveals that the magnitude of oxygen concentration is not as important as its spatial concentration gradient: decreasing ambient oxygen concentration causes significantly less sprouting than applying an external oxygen gradient to the vessels. In contrast, barriergenesis is dictated by shear stress independent of local oxygen concentrations, suggesting that different mechanisms mediate angiogenesis and barrier formation and that angiogenic sprouting can occur without compromising the barrier. Overall, these results improve our understanding of how specific biophysical variables regulate the function and

activation of cerebral vasculature, and identify spatial oxygen gradients as the driving factor of angiogenesis in the brain.

Introduction

The brain is a highly metabolically active organ that accounts for 20% of the body's total oxygen consumption despite only accounting for approximately 2% of total body weight [194]. It has a heterogeneous topography of local metabolic requirements dictated by neuronal density and activity [195], and precise regulation of blood flow to supply oxygen and nutrients is vital for proper functioning of brain tissue. While most endothelial cell subtypes in other parts of the body rely heavily on glycolysis for energy production [196], cerebral endothelial cells, which form tight junctions that give rise to the blood-brain barrier, contain a greater concentration of mitochondria that produce energy via oxidative phosphorylation [197]. This difference suggests that cerebral endothelial cells may be more sensitive to changes in local oxygen concentrations than in other tissues. Recent studies have shown that even mild levels of hypoxia can lead to blood-brain barrier disruption and subsequent angiogenesis in mice [198], but the relationship between oxygen tension and cerebral endothelial function has yet to be directly interrogated in a controlled, *in vitro* environment.

Hypoxia occurs in physiological processes including development as well as a broad range of pathologies that encompasses cancer and stroke [199]. Hypoxia is generally associated with an increase in angiogenesis through activation of hypoxia inducible factors, which in turn regulate the transcription of pro-angiogenic factors [200]. In systemic vasculature, and specifically during processes related to cancer, angiogenesis is generally associated with increased vascular permeability due to the effects of proteins like vascular endothelial growth factor (VEGF) [201]. However, increased permeability in the brain has

severe consequences: blood-brain barrier disruption leads to inflammation and subsequent damage to the surrounding parenchyma [202]. Previous studies have shown that angiogenesis and barriergenesis can occur simultaneously in the developing brain so that new blood vessels can sprout from existing vasculature without allowing transport of blood components into the extracellular matrix of the central nervous system [203]. However, the factors that mediate angiogenesis and barriergenesis in cerebral vasculature during both development and disease remain mostly unclear.

In recent years, *in vitro* models of vasculature have provided tremendous insight into angiogenesis and the formation of neovasculature in controlled, three-dimensional environments. In contrast to tubulogenesis assays on two-dimensional substrates, 3D systems can capture the cell-matrix interactions that mediate sprouting and neovessel formation. The effects of both biochemical factors [133], [204], [205] and mechanical stimuli [127], [206]–[212] on angiogenesis have been extensively investigated in these systems. The primary advantage of 3D models, despite not fully recapitulating the *in vivo* microenvironment, is their ability to precisely control environmental factors to provide a mechanistic understanding of pro-angiogenic processes. These systems have also been used to assess the angiogenic response to hypoxia [213], demonstrating that hypoxia influences the effects of other factors that stimulate neovessel formation. The recent development of 3D models of the blood-brain barrier provides a means to interrogate the effect of hypoxia and other factors on both angiogenesis and barriergenesis in a controlled environment.

Another advantage of 3D *in vitro* models is their compatibility with computational modeling to predict spatial and temporal distributions of angiogenic factors exposed to

endothelialized vessels. Complex computational models have been developed to predict the angiogenic response to interstitial fluid flow by coupling convective and diffusive transport with constitutive equations predicting cell division and migration [209], [214]–[216]. Coupling finite element simulations of oxygen transport with experimental data has previously been used to predict cell viability within *in vitro* systems [125]. An important component of oxygen tension models is the prediction of cellular oxygen consumption, which serves as a major sink in the diffusive constitutive equation. There has been substantial innovation in systems to directly measure cellular oxygen consumption including microfluidic-based approaches [217]. Accurate measurements of oxygen consumption are vital to informing computational models of oxygen diffusion within *in vitro* systems, and previous studies have provided measurements of oxygen consumption by cerebral endothelial cells in culture [218]–[220]. Overall, combining *in vitro* platforms with computational models informed by cellular oxygen consumption rates can provide new insight into processes affecting angiogenesis and barriergenesis in cerebral vasculature.

Materials and Methods

Microfabricated devices and hydrogel preparation

Polydimethylsiloxane (PDMS) microfluidic devices were fabricated using soft lithography [124], [186]. Briefly, positive features were used to cast negative features and a layer of PDMS was used to enclose the devices. The hydrogel reservoir was filled with 5 M sulfuric acid for 90 minutes, washed thoroughly with deionized water, and coated with 20 µg/mL collagen for 60 minutes. All microfluidic devices were sterilized using shortwave length ultraviolet light prior to use. Collagen hydrogels were formed within reservoirs in the device by mixing solubilized collagen in 0.02 N acetic acid with 10X PBS,

0.1 M NaOH, 1 mg/mL of Matrigel and deionized water to yield a final concentration of 2 mg/mL [125], [221]. For gels containing hyaluronan (HA), the deionized water was replaced with 2-2.4 MDa HA to create a final mixture of 1 mg/mL HA, 1 mg/mL Matrigel and 2 mg/mL collagen [126], [186].

Cell culture

P22-23 human cerebral microvascular endothelial cells (HCMEC/d3) were cultured in gelatin-coated culture plates prior to use in experiments. Modified endothelial growth medium (EGM-2) was prepared using a previous protocol [222]. The final concentrations of EGM-2 yielded the following: 5 µg/mL ascorbic acid (Sigma), 1 ng/mL bFGF (Peprotech), 1% chemically defined lipid concentration (Thermo Fisher) 5% fetal bovine serum (FBS) (VWR), 10 mM HEPES buffer (VWR), 1.4 µM of hydrocortisone (VWR), and 1% penicillin-streptomycin (VWR). HCMEC/d3 were thawed 5 days prior to seeding and medium was changed every other day.

3D angiogenic model

Three-dimensional blood vessels were fabricated using a previously described protocol [124], [186]. Briefly, 60 µL of collagen gel was injected into the hydrogel reservoir of the device and either 180-µm or 300-µm diameter acupuncture needles coated with 0.1 % BSA were inserted prior to polymerization. The needles were removed after the hydrogel polymerized to create 2 parallel cylindrical channels in which HCMEC/d3 cells were injected into one channel at a density of 5×10^6 cells/mL. For high-density 300-µm blood vessels, cells were seeded at a density of 20×10^6 cells/mL. The endothelialized channels were incubated for 10 minutes on each side to ensure cell attachment. Following

cell seeding, these channels were either exposed to static conditions or perfused with culture medium using a linear syringe pump (Kent Scientific) for 4 days.

Hypoxia experiments

Blood vessels fabricated in 300-µm channels were cultured with EGM-2 in static conditions in a 1% O_2 hypoxic chamber by purging with nitrogen for 4 days while maintaining 37°C and 5% CO_2. To create an oxygen gradient in a hypoxic incubator, a syringe pump containing EGM-2 was placed outside the incubator and injected the medium into the adjacent channel at a fixed rate of 2.4 µL/min for 4 days.

Immunocytochemistry

Microfluidic devices were fixed with 4% paraformaldehyde (Alfa Aesar) for 20 minutes and permeabilized with 0.2% Triton X-100 (Sigma) for 20 min at room temperature. For ZO-1 labeling, hydrogels were removed from the devices and blocked by 3% bovine serum albumin (BSA) for 30 min at room temperature. These gels were incubated with 1:250 anti-ZO-1 (Cell Signaling) for 48 hours at 4°C. These gels were washed thoroughly with PBS and all secondary antibodies were used at 1:500 dilution. Cell nuclei were identified with DAPI (1:500) and F-actin was stained using Alexa Fluor 488-conjugated phalloidin at 37°C for 60 minutes.

Sprout quantification

Images of the vessel walls were converted to 8-bit image files, rotated, and cropped to a height of 999.81 units so that the sprouts emanated from the right side of the image. A custom MATLAB program converted the image to a binary matrix with a gradient mask. Based on the final binary mask image, a new matrix was generated. The sprout frequency for each vessel wall was determined by calculating the percentage of the vessel border

exceeding a threshold distance of 40 microns from the parent microvessel to include only mature sprouts. The algorithm was also utilized to evaluate the normalized average sprout length, standard deviation, root mean square, and maximum length of the sprouting in each vessel wall.

Glucose Measurements

To measure the glucose concentrations within each vessel condition, 15-µL of media was removed from 300-µm diameter vessels (both low and high density) after 4 days of incubation. Test strips compatible with a OneTouch glucometer were used to determine the amounts of glucose in the media and measurements were performed in triplicates for each condition.

Permeability testing

Blood vessels exposed to experimental conditions were transferred to a stage of an inverted epifluorescent microscope enclosed by an environmental chamber. Using a syringe pump, 4-kDa FITC dextran was perfused into the channels at a flow rate of 5 µL/min for 10 minutes while submerged in culture medium to maintain cell viability. Images were taken at 30-s intervals, and the permeability coefficients were calculated using the following equation [60], [223]: $P = \frac{dI}{dt}\frac{r}{2I_o}$ where dI/dt is the change in intensity over time, r is radius of the blood vessel and I_o is the maximum intensity.

Oxygen consumption assay (OCR)

Oxygen consumption rate assay kits (Cayman Chemicals) were used to measure the relative amounts of oxygen consumed within each vessel condition. Due to the nature of the small cylindrical channels, we could not control the exact number of cells seeded within the channel for a given cell density injected into the device. Thus, in order to determine the

number of cells lining the channel walls, DAPI images were obtained and cell nuclei were counted within each vessel condition. The cell densities for the OCR assays were then chosen to replicate these measurements: 10,000 cells/well as a reference, 129,408 cells/well (180-µm), 112,704 cells/well (300-µm, low density) and 175,296 cells/well (300-µm, high cell density). HCMEC/D3s were plated in a 96-well plate for 2 hours to form a 2D monolayer, since the assay was not compatible with the 3D model. Once the monolayer was formed, culture medium supplemented with 10-µL of phosphorescent oxygen probe was added and oxygen consumption was measured over a time span of 30 minutes. These relative rates were then compared to previously published values to provide absolute quantities [218], [219].

Computational modeling

In order to predict oxygen distributions within the hydrogel containing the 3D brain microvascular model, a finite element model was constructed using commercially available software (COMSOL). A schematic of the microfluidic device and the location of the collagen gel within the device is shown in Supplemental Figure A1A. The geometry of the collagen gel was imported into the finite element software and boundary conditions were applied. The cellular channel was modeled as a 5-µm-thick annulus as shown in Supplemental Figure A1B; the diameter of the acellular and cellular channels was set to either 180 or 300 µm depending on the experiment. A constitutive equation for Fick's second law was solved over the discretized geometry (triangular mesh elements):

$$\nabla \cdot \mathbf{J} = R$$

where **J** is the flux vector and R is the reaction rate.

Boundaries in direct contact with culture medium were set as fixed concentration to 21% oxygen (9.4 mol/m^3). The cellular annulus was set as a 0th-order volume reaction term with consumption rates obtained from the OCR for different cell seeding densities. The remaining boundaries were considered no flux (Supplemental Figure A1C). The oxygen diffusion coefficient was set at 4.5 x 10-10 m^2/s within the collagen gel, using a value obtained from a previous study [224].

In the hypoxic gradient experiments, when medium is perfused through the acellular channel, the boundary in the acellular channel is fixed at 9.4 mol/m^3. The Peclet number of the flow in the hypoxic gradient (300 µm diameter vessel and 5 µL/min flow rate) was approximately 8000, indicating convection dominates diffusion and the use of a constant concentration boundary condition.

Statistics

Two-way ANOVA and post-hoc Tukey's HSD tests were performed to calculate statistical differences unless otherwise specified. For the hypoxic experiments, a Welch Two Sample t-test, assuming normal distributions with unequal variances between groups was used to calculate significant differences. P-value less than 0.05 indicated significant differences. Measurements from each condition were averaged from n = 3 or greater.

Results

I. The effect of ECM composition and fluid flow on angiogenic sprouting

A primary advantage of the three-dimensional brain microvascular model is its ability to control specific biophysical variables in order to probe their effect on angiogenic sprouting. These studies interrogated the effects of both HA concentration in the collagen hydrogel and the application of fluid shear stress to the endothelial cells. Previous studies have shown that the addition of hyaluronan slows down the rate of polymerization of

collagen hydrogels without affecting their equilibrium storage moduli, thus these experiments did not evaluate the effect of matrix mechanical properties on sprouting [125]. In order to quantify angiogenesis, a MATLAB code was written to measure the percentage of the vessel experiencing angiogenic sprouting for four days following cell seeding. Although maximum sprout length was initially calculated, sprouting frequency provided a more representative estimation of angiogenic activity along the length of the vessel in the bulk of the hydrogel. Figures A1A and A1B show the entire 3D brain microvascular blood vessels exposed to static and flow conditions. Figures A1C and A1D focus on the edge of phalloidin-stained vessels in collagen-only hydrogels after four days in two orthogonal planes. A shear stress of 0.7 dyn/cm^2 was chosen based on previous studies demonstrating this magnitude causes barriergenesis [124] and is lower than the threshold that induces angiogenesis in HUVEC-lined channels [127]. Shear stress substantially reduced sprouting from the vessel, though there were regions of the vessel exhibiting endothelial migration into the surrounding matrix (Figure A1D,ii). Figure A1C,ii (white arrow) shows the presence of small lumens in the sprouting structures in the static condition, indicative of early neovessel formation that is not observed in the flow condition (Figure A1B,ii). The addition of hyaluronan into the matrix did not affect sprouting in both static and flow conditions (Figures A1E,A1F). Again, only the static vessels featured lumens in the sprouting structures. Two-factor ANOVA analysis confirmed that the addition of flow but not hyaluronan significantly affected sprouting from the endothelial vessels (Figure A1G).

II. Evaluating the effect of biophysical factors on oxygen concentration

In addition to exerting shear stress to the endothelial cells lining the vessel, the application of fluid flow also alters local oxygen tension by constantly replenishing the

oxygen concentration within the cell-seeded channel. In static conditions, cellular oxygen consumption reduces the local oxygen concentrations. In order to determine whether the primary anti-angiogenic effect of fluid flow is either by application of shear stress or by altering oxygen tension, endothelial cells were seeded within a larger diameter (300 µm) vessel. Increasing the diameter of the vessel reduces the volumetric density of the cells and mitigates local reduction in oxygen concentration. Therefore, an additional control was created by seeding these larger vessels with a higher concentration of cells, since recent studies have shown that altering radius of curvature can also dictate cell response [225]. The cell number per unit area was quantified in the following six conditions: (i) 180-µm static, collagen-only, low seeding density, (ii) 180-µm flow, collagen-only, low seeding density, (iii) 180-µm static, collagen-HA, low seeding density, (iv) 180-µm flow, collagen-HA, low seeding density, (v) 300-µm static, collagen-only, low seeding density, and (vi) 300-µm static, collagen-only, high seeding density. Figures A2A-B show DAPI stains of the walls of each of these vessels. One-way ANOVA and post-hoc Tukey comparisons indicated that the 300-µm high density condition had a significantly higher density than the 300-µm low density condition (Fig. A2C). Images and quantification of DAPI within collagen/HA hydrogels reveal no significant difference between flow and static conditions (Supplemental Figure A2). In order to determine whether the difference in cell density also affected glucose levels, medium removed from the vessels was measured with a glucose sensor and indicated there was no significant differences between high and low cell density conditions (Supplemental Figure A3A). An oxygen consumption assay was then conducted on the cell density representing low density (112,704 cells/well) and high density (175,296 cells/well) as well as a density used in a previous study of HCMEC/D3 oxygen

consumption that served as a reference value [218], [219]. The consumption rates were measured to be 6.4×10^{-11} mol/min and 9.6×10^{-11} mol/min for the low and high densities respectively (Supplemental Figure A3B,C).

The consumption rates were then incorporated into a finite element model as a reaction term in the diffusion constitutive equation for different cell densities. Figure A2D shows contour maps of oxygen tension for 180-µm vessels in static and flow conditions and 300-µm vessels with low and high seeding densities. Supplemental Figure A4 demonstrates that the oxygen gradient is mostly constant along the length of the channel in the bulk of the hydrogel where measurements were taken. The HA-containing vessels weren't modeled since the presence of HA did not significantly affect cell density. The predicted oxygen tensions surrounding the vessels indicated substantial differences based on vessel radius and the application of shear stress. As expected, applying flow maintains the oxygen levels at ambient levels, and the larger diameter vessel mitigates the oxygen reduction for a given cell density. Figure A2E shows that the high cell density increases the oxygen deficit in the 300-µm vessel, but not to the level of the 180-µm vessel exposed to static conditions. Given the large difference in oxygen concentration between the 300-µm high density and low density vessels, sprouting density was evaluated in these two conditions. Figure A2F shows there is substantially more sprouting in the high density vessel, and one-factor ANOVA reveals that the cell density significantly affects sprouting percentage (Fig. A2G). Moreover, the 180-µm static vessel, which the finite element model predicted to have the lowest local oxygen concentrations, had significantly greater sprouting than both the high and low cell density 300-µm vessels (Supplemental Figure

A5). Combined with the results presented in Figure A1, these results suggest a direct correlation between reduced oxygen levels and increased angiogenic response.

III. Differentiating between the effects of oxygen concentration and oxygen gradient

In order to determine whether hypoxia is the driving factor for angiogenesis in the 3D brain microvascular model, 300-µm vessels with low cell seeding density were incubated in a hypoxic chamber for four days prior to measuring angiogenic sprouting. As shown in Figure A2F, not only is the oxygen concentration reduced in the conditions exhibiting increased sprouting, but the oxygen gradient is also increased. Therefore, a second condition was tested by imposing an external oxygen gradient to the vessel: oxygenated medium was perfused through the channel adjacent to the endothelialized channel while the device was in the hypoxic chamber. In order to verify that application of flow through the acellular channel did not cause interstitial pressure gradients across the cell-seeded channel, the fluid dynamics were assessed by modeling the collagen gel as a porous medium [226]. Supplemental Figure A6 indicates that there is a negligible interstitial pressure gradient caused by perfusion through the acellular channel. Schematics in Figures A3A,i and A3A,ii display the differences between the hypoxic and oxygen gradient conditions. Figure A3B shows that minimal sprouting was observed in blood vessels exposed to a constant 1% O_2 environment after 4 days. In contrast, the channels with the external oxygen gradient exhibited substantial sprouting along the length of the vessel (Fig. A3C,ii). Quantification revealed that blood vessels in the constant hypoxic environment exhibited significantly lower sprout percentages compared to the O_2 gradient condition (Fig. A3D). The finite element model provided a means to estimate the difference in oxygen gradients between conditions. Figure A3E shows contour plots between the

hypoxic and gradient conditions, and Figure A3F provides quantification of the spatial oxygen gradient for these two conditions as well as the 300-µm low density vessels in normoxic conditions. The plot shows that despite the large difference in absolute oxygen concentrations, there is a negligible difference in the oxygen gradient between normoxic and hypoxic conditions (~200 mol/m^3/m) compared to the imposed gradient, which is approximately an order of magnitude greater. Overall, these results demonstrate that the oxygen gradient is the main driving factor for angiogenesis and that the biophysical factors that affected sprouting, flow and radius of curvature, did so primarily through their effects on the oxygen gradient experienced by cells lining the vessel.

IV. Evaluating the influence of oxygen gradients on barriergenesis

The importance of oxygen gradient on barrier formation was also evaluated in the 3D brain microvascular model. Previous studies have found that fluid flow is required for barrier formation, with the assumption that the shear stress exerted by the fluid flow was the primary factor for barriergenesis. Given the result that fluid flow also altered the oxygen gradient, the barrier integrity of several conditions with varying angiogenic responses (180-µm static with and without HA, 180-µm flow with and without HA, and 300- µm low density) were evaluated to interrogate any potential correlation between oxygen levels and tight junction formation. The vessels exposed to static conditions exhibited no significant difference in either ZO-1 localization to the cell-cell junctions (Figs. A4A-C) or in the permeability of 4-kDa FITC dextran (Fig. A4D), despite large differences in sprouting caused by the difference in vessel diameter. Moreover, the 180-µm vessels exposed to flow exhibited substantially lower vessel permeabilities. There was increased ZO-1 localization to cell-cell junctions (Figs. A4E-F) and the permeability was significantly lower than the

static values (Fig. A4G). In contrast to the static conditions, there was a significant difference between the flow conditions with and without HA: incorporation of HA significantly reduced the permeability, despite not having any effect on oxygen gradient and angiogenic sprouting. The ZO-1 images and permeability assays are consistent with previous results showing that CD44 mediates shear stress mechanotransduction through small GTPases such as RhoA and Rac1 to induce barriergenesis in cerebral vasculature [186]. Moreover, ZO-1 was present in the sprouts from both static and flow conditions, but it was not localized to the cell-cell junctions in either condition (Supplemental Figure A7). This result is consistent with the permeability measurements, since parent vessels did not exhibit barrier function in the static condition and there were no lumens observed in the sprouts from parent vessels exposed to flow. Overall, these results demonstrate no correlation between oxygen gradient and barrier integrity and supports the hypothesis that the mechanical stress exerted by fluid flow is the primary factor driving barrier formation in the 3D brain microvascular model. Taken together with the data presented in Figure A1 that vessels exposed to flow exhibit a non-zero level of angiogenic sprouting, these results suggest that the mechanisms dictating angiogenesis and barriergenesis are independent from one another and sprouting does not compromise the barrier.

Discussion

The combination of experimental and computational results presented here identify the spatial oxygen gradient as the primary instigating factor for angiogenic sprouting in cerebral vasculature among the biophysical parameters evaluated here: matrix composition, fluid shear stress, and vessel diameter. The relationship between oxygen concentration and angiogenesis has been cited frequently, especially in the context of tumor formation where hypoxia and formation of neovessels are spatially correlated. However,

there is ample evidence that the connection between oxygen concentration and angiogenesis may be more complex than a direct causal link: previous studies have shown that hypoxia does not always correlate to the growth of new blood vessels from existing vasculature [227]. Several tissues including the myocardium [228] and visual cortex [229] have baseline, physiologic hypoxia that do not induce angiogenesis. Moreover, there are processes like wound healing where hypoxia is a byproduct of angiogenesis, not a driving factor [227]. The *in vitro* 3D brain microvascular model presents a means to directly evaluate the effect of hypoxia in cerebral vasculature, and it demonstrated no significant difference in sprouting between normoxic conditions and an environment with 1% oxygen. In contrast, imposing an external oxygen gradient by perfusing oxygenated medium through an adjacent channel in low oxygen ambient conditions significantly increased angiogenic sprouting. Taken together, these results show that simply decreasing the oxygen levels does not lead to activation of endothelial cells, but rather the presence of a gradient may lead to angiogenesis.

Further studies are required to clarify whether the effect of oxygen gradient on angiogenesis is unique to the central nervous system. Endothelial cells in the brain have unique properties, including the formation of tight junctions that give rise to the blood-brain barrier. Their metabolic activities also differ from other regions of the body, and therefore these cells may respond to oxygen levels differently from their counterparts in other organs. There are several pathologies where large oxygen gradients are present within the central nervous system, and these scenarios are characterized by rapid angiogenesis. For example, the formation of glioblastoma (GBM) creates large spatial gradients of oxygen between the tumor and surrounding parenchyma, and GBM exhibits substantial

growth of new vessels from the existing vasculature [36–37]. Moreover, following spinal cord injury there is a strong and temporary angiogenic response that precedes the formation of a glial scar [36], and the site of injury is characterized by hypoxia due to disruption of the blood supply. The result that oxygen gradient is the primary driving factor for angiogenesis in the central nervous system is consistent with these pathologies. There are several examples of pathologies outside the central nervous system, including tumor formation and wound healing, that suggest the effect of oxygen gradient is universal. *In vitro* vascular models provide a means to evaluate the relationship between spatial differences in oxygen levels and angiogenesis in other organ systems.

The effect of oxygen gradients on barrier formation was also evaluated, given the ability of cerebral endothelial cells to form tight junctions. In contrast to angiogenesis, there did not appear to be a correlation between oxygen gradient and the barrier integrity of the 3D vessels. Both the low density, 300-µm diameter vessel cultured in static conditions and the 180-µm diameter vessel perfused with 0.7 dyn/cm^2 of shear stress exhibited the two lowest oxygen gradients of the conditions tested, and these conditions had significantly different permeabilities and localization of ZO-1 to cell-cell junctions. As shown in a previous version of this 3D blood-brain barrier model [124], the main driving factor for barrier formation is the shear stress exerted on the endothelium by fluid flow, and these results are consistent with that finding. These studies indicate that different stimuli and likely different signaling pathways mediate barrier formation and angiogenic sprouting. Given that the vessels exposed to flow exhibited some level of sprouting, though significantly less than other conditions, the two processes of barrier formation and angiogenesis may occur simultaneously. In fact, a recent study using transgenic zebrafish

with promoters for barrier development demonstrated that angiogenesis and barriergenesis occur at the same time within the central nervous system [203]. Additional studies are required to understand the interdependence, or lack thereof, of signaling pathways mediating these two processes.

The results of the study do not preclude the importance of other pro-angiogenic factors unrelated to the spatial oxygen gradient. Although non-cerebral endothelial cells were used, previous *in vitro* models have identified the growth factors most likely to stimulate sprouting from an endothelialized vessel [204]. Small GTPases like cdc42 that contribute to sprouting are activated by specific agonists and not differences in oxygen concentration [205]. Furthermore, previous studies have shown that fluid shear stress, if applied with a sufficiently high magnitude, can induce sprouting from HUVEC-lined channels with diameters of 400-μm [127]. Augmenting shear stress by increasing flow rate does not exacerbate the oxygen gradient experienced by the cells within the vessel, suggesting that the mechanical stimulus is responsible for instigating angiogenesis. Overall, there are likely several biophysical and biochemical factors that cause sprouting independent of local oxygen levels. Nonetheless, the studies presented here reveal that oxygen gradient is more important than overall oxygen concentration for driving angiogenesis.

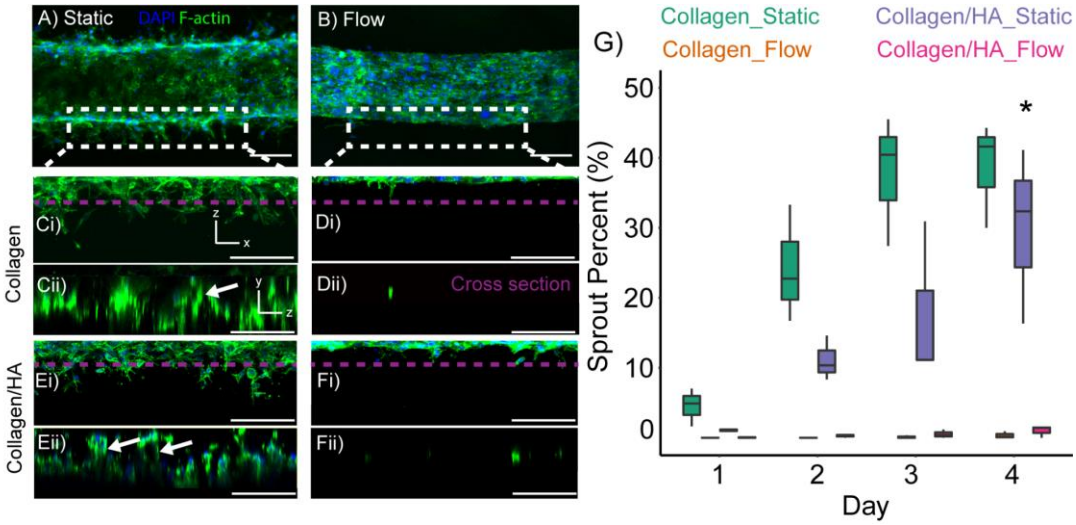

Figure A1. 180-µm blood vessels exposed to (A) static and (B) flow conditions after 4 days in culture. Angiogenic sprouts from 180-µm parent blood vessels fabricated in (C,D) collagen and (E,F) collagen/HA hydrogels on day 4. (Ci,Ei) Blood vessels incubated in static conditions and (Di,Fi) vessels exposed to fluid flow. (ii) Confocal microscopy stacks of the YZ plane showing the presence of sprout lumens (white arrows). Purple dotted lines in C-F indicate the region of cross-section used for orthogonal views to identify the presence of luminal space within the angiogenic sprouts. E) Sprouting percentage of the 4 conditions. DAPI = blue and F-actin = green. Scale = 100 µm. The box plots depict the median, 25 and 75 percentiles, and the whiskers represent 1.5x the interquartile range. *$p < 0.05$ ($n = 3$).

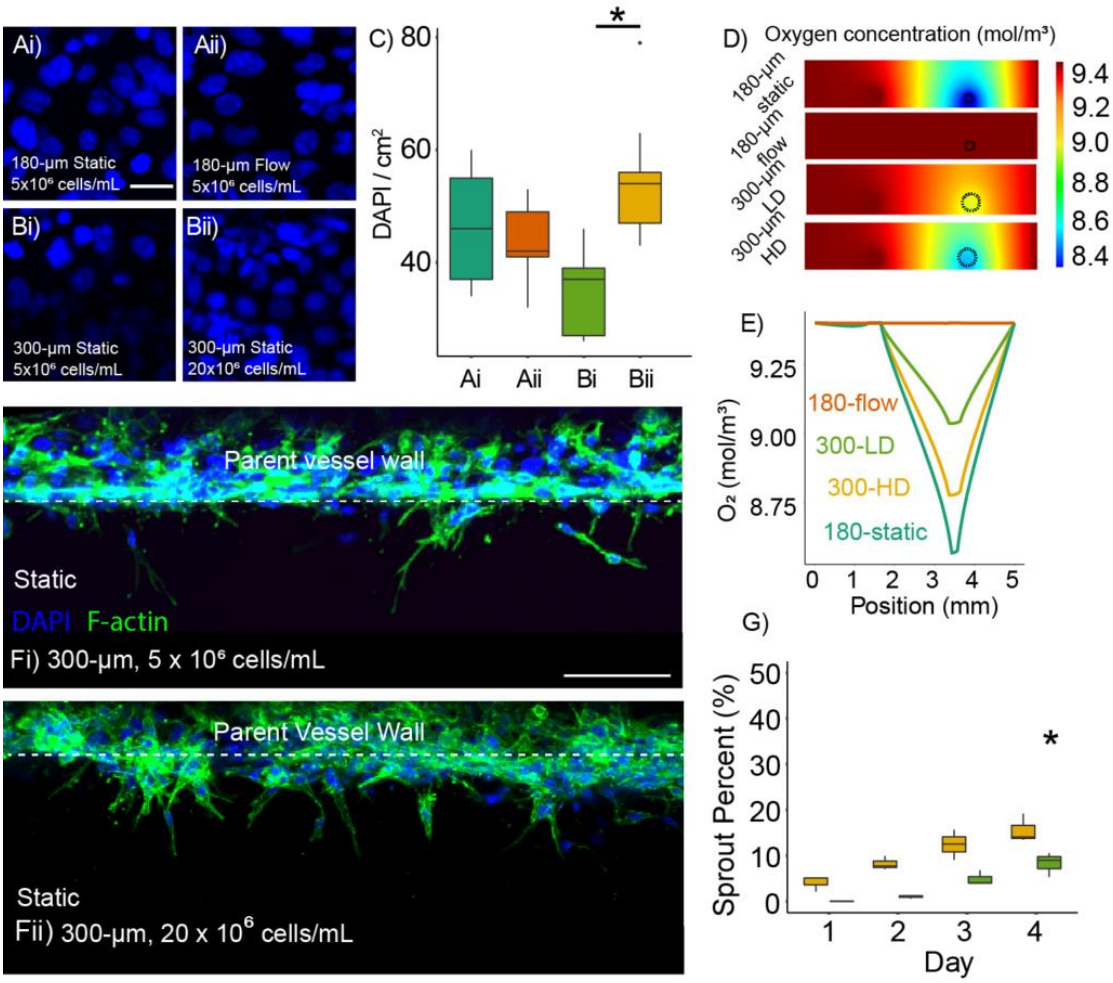

Figure A2. Confocal images of DAPI stains verifying cells per area in (A) 180-µm seeded with 5×10^6 cells/mL in collagen-only hydrogels exposed to (i) static and (ii) flow conditions and (B) 300-µm collagen-only hydrogels seeded with (i) 5×10^6 cells/mL and (ii) 20×10^6 cells/mL. (C) Quantification of nuclei per cm^2. (D) Computational models of oxygen consumption in each vessel conditions. Scale = 100 µm. (E) Oxygen levels dependent on distance from vessels, y-axis range is 8.5-9.5 mol/m^3. (F) Immunofluorescence images of angiogenic sprouts in 300-µm seeded with (i) 5×10^6 cells/mL and (ii) 20×10^6 cells/mL. (G) Sprouting percentage of these conditions. DAPI = blue and F-actin = green. Scale = 50 µm. The box plots depict the median, 25 and 75 percentiles, and the whiskers represent 1.5x the interquartile range. *$p < 0.05$ ($n = 3$).

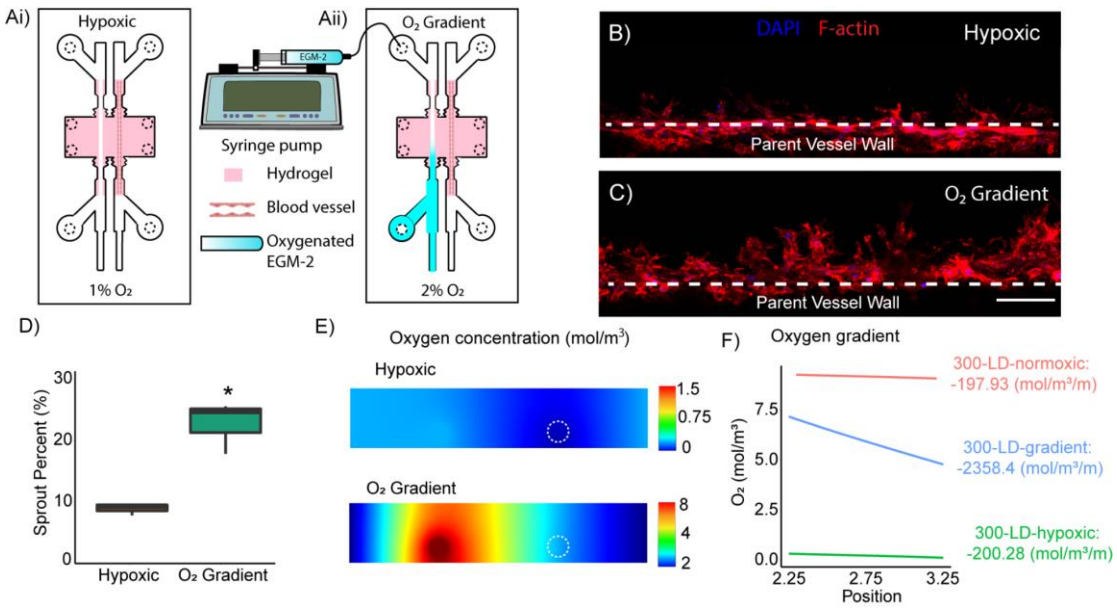

Figure A3. Schematic of blood vessels in static conditions incubated in a hypoxic and oxygen gradient environment. Confocal images of angiogenic sprouts in 300-µm vessels seeded with 5×10^6 cells/mL exposed to (B) hypoxia and (C) O_2 gradient. (D) Quantification of sprout percentage. (E) Computational models of oxygen concentration in each vessel conditions. (F) Oxygen levels dependent on distance from vessels. DAPI = blue and F-actin = red. Scale = 100 µm. The box plots depict the median, 25 and 75 percentiles, and the whiskers represent 1.5x the interquartile range. *$p < 0.05$ ($n = 3$).

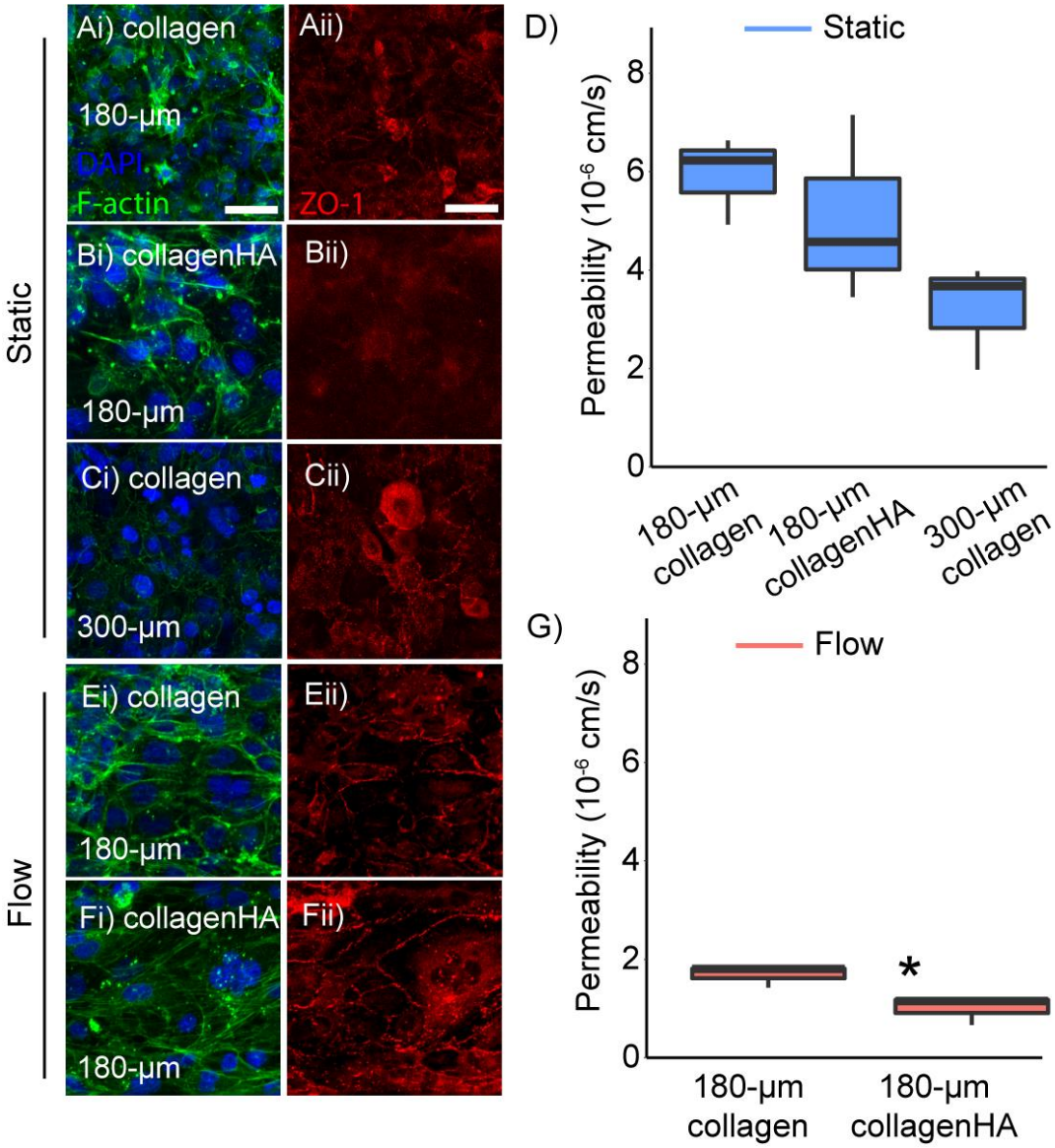

Figure A4. (A-C) Confocal stacks of blood vessels cultured in static conditions and (E-F) flow conditions labeled with (i) DAPI (blue), FITC-phalloidin (green), and (ii) ZO-1 (red). Permeability quantification of vessels exposed to (D) static and (G) luminal shear stress for 4 days measured with 4kDa dextran. Scale = 50 µm. The box plots depict the median, 25 and 75 percentiles, and the whiskers represent 1.5x the interquartile range. *$p < 0.05$ ($n = 3$).

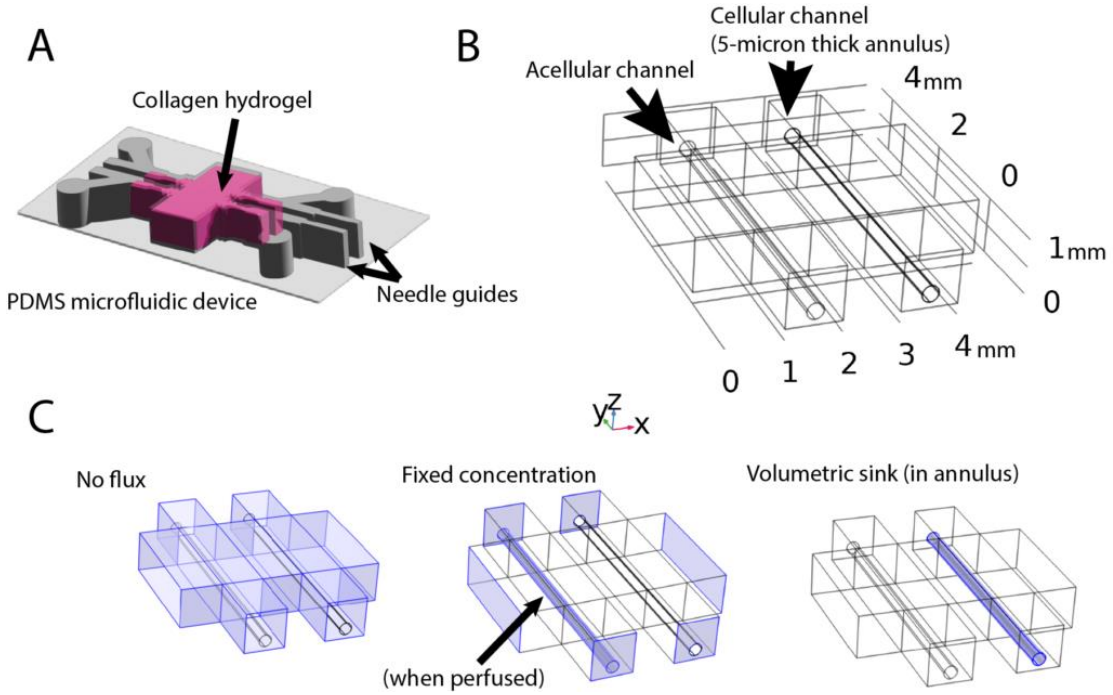

Supplemental Figure A1. Computational model methods. (A) Schematic of microfluidic device showing the location of the hydrogel for the computational model. (B) A mesh showing cell-seeded and acellular channels. (C) Parameters for the COMSOL models.

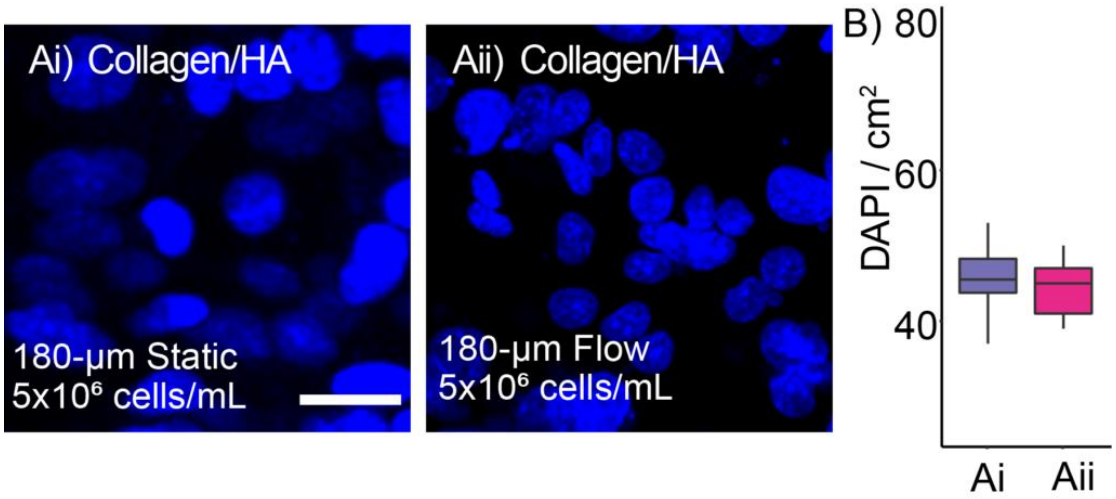

Supplemental Figure A2. DAPI stains verifying cells per area in collagen/HA hydrogels exposed to (Ai) static and (Aii) flow conditions. (B) Quantification of DAPI per cm^2. DAPI = blue. Scale = 100 µm. *$p < 0.05$ ($n = 3$).

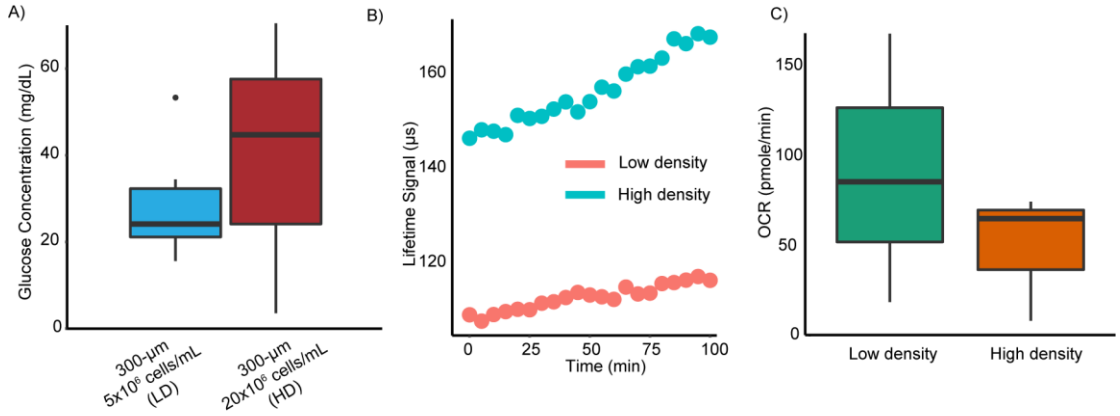

Supplemental Figure A3. (A) Glucose concentrations within the 300 µm low cell and high cell density vessels. (B) Representative lifetime signal from oxygen phosphorescent probe from each condition. (C) Oxygen consumption rates for low cell and high cell density conditions.

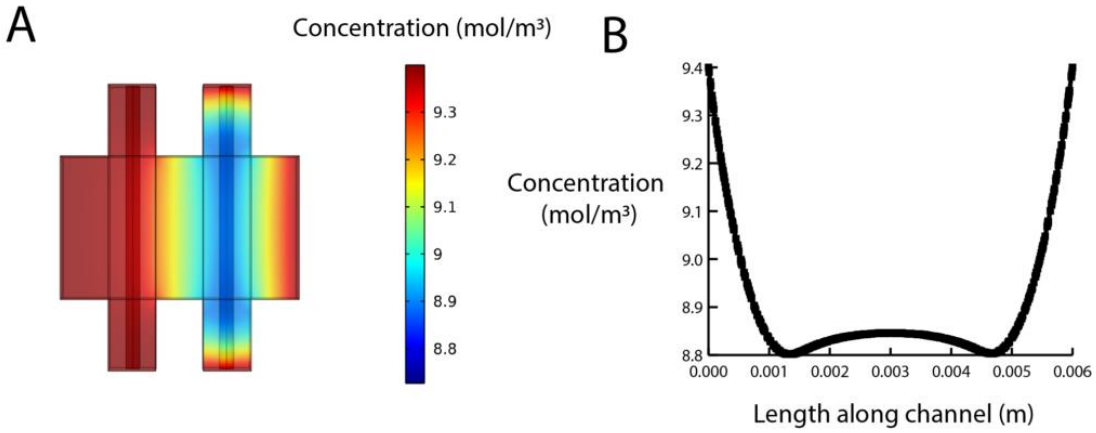

Supplemental Figure A4. (A) Oxygen concentration along the length of 3D brain microvascular model. (B) Concentration profile along the channel.

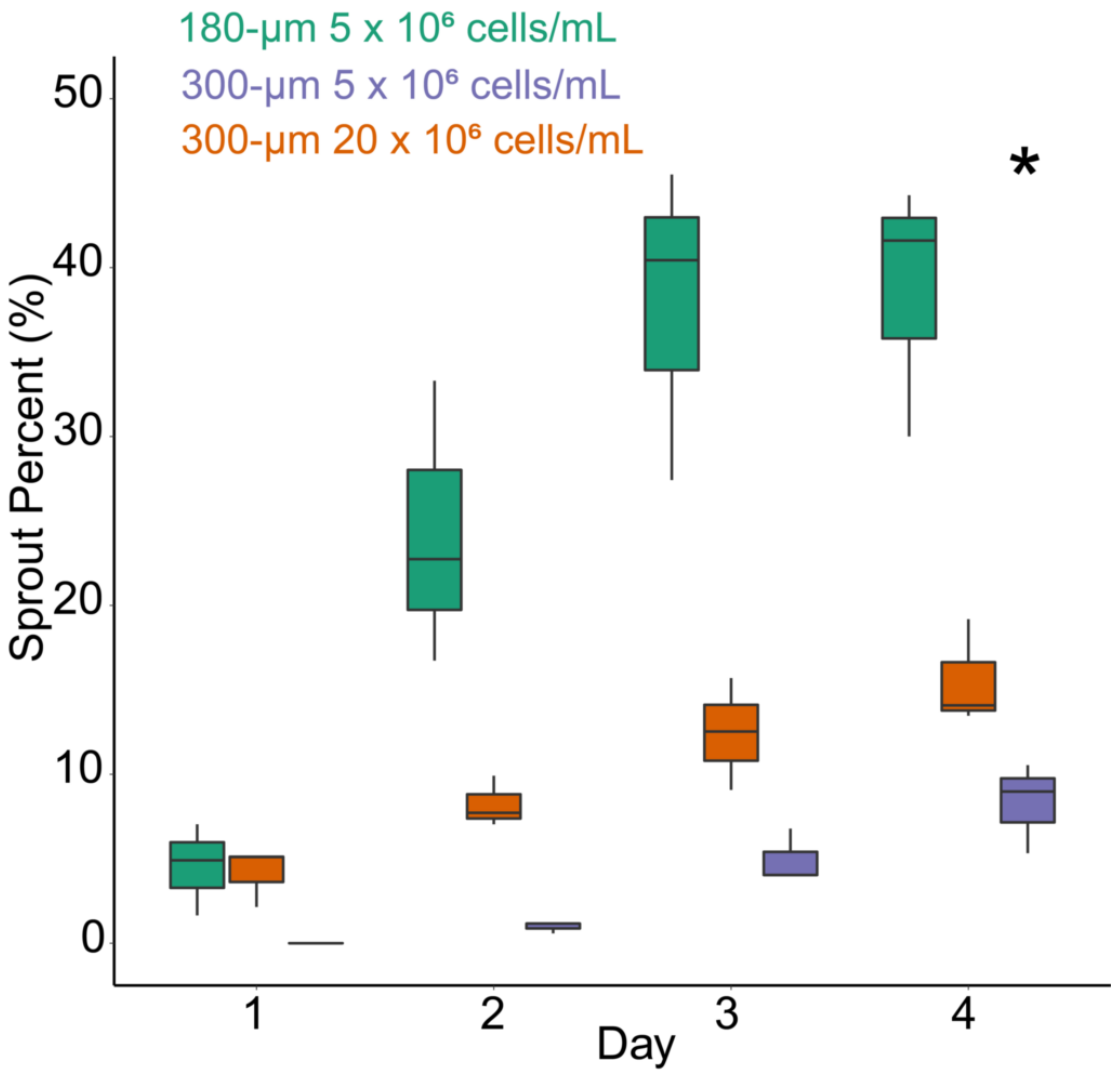

Supplemental Figure A5. Box plot comparing sprout percentage between 180 µm and 300 µm blood vessels in collagen hydrogels. *$p < 0.05$ ($n = 3$).

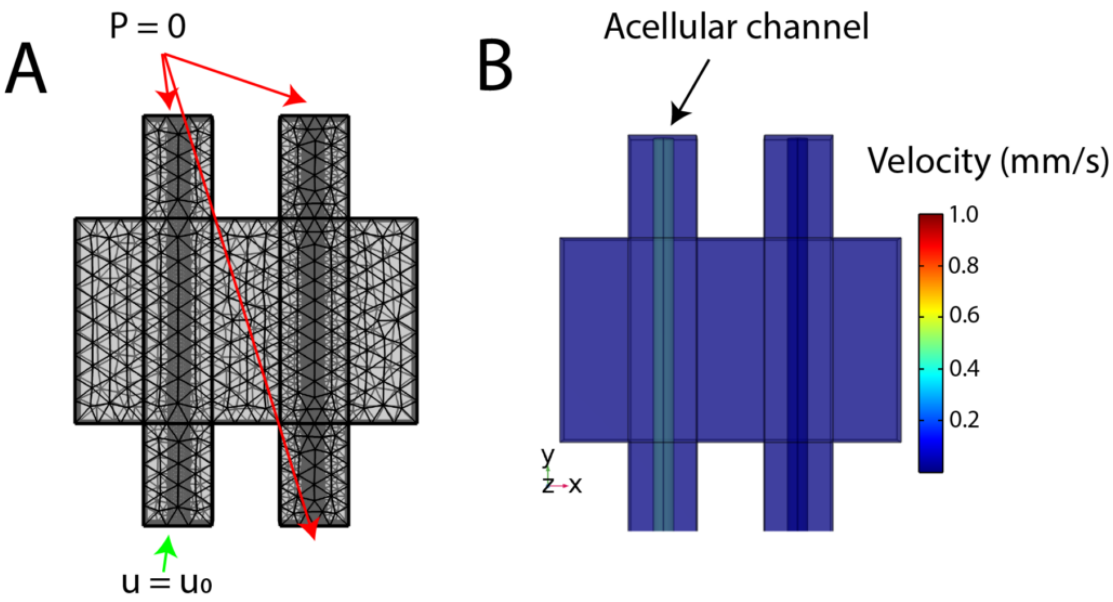

Supplemental Figure A6. Computational model of interstitial pressure gradients in collagen hydrogels showing (A) pressure in a porous medium and (B) velocity from the adjacent acellular channel.

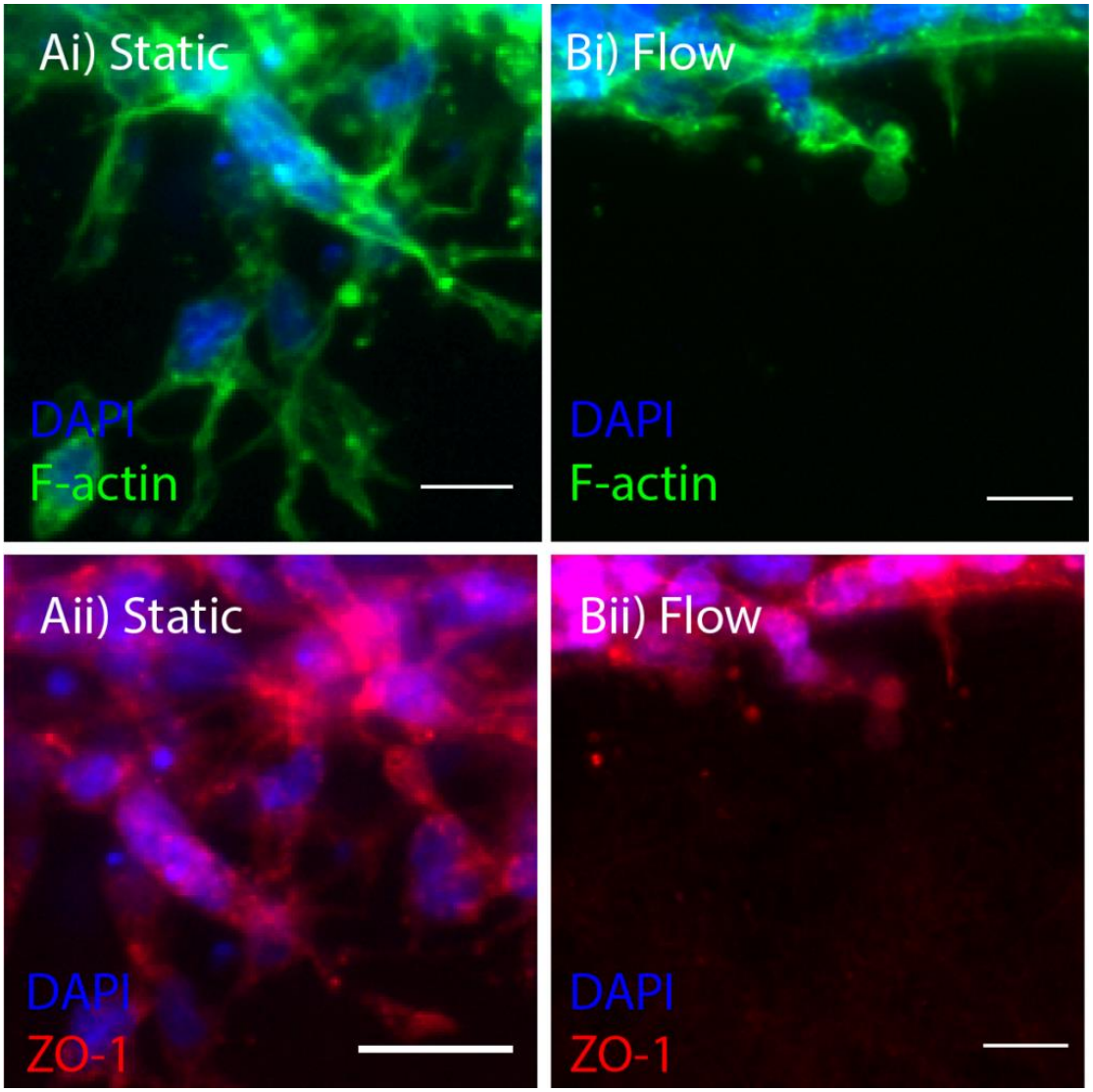

Supplemental Figure A7. ZO-1 in angiogenic sprouts in (A) static and (B) flow conditions. DAPI = blue, F-actin = green, ZO-1 = red. Scale = 15 μm.